EVALUATION AND SCREENING OF ADSORBENTS FOR THE SEPARATION OF CARBON DIOXIDE FROM NATURAL GAS

Lefu Tao

ORCID: 0000-0002-8300-7886

Submitted in total fulfilment of the requirements of the degree of Doctor of Philosophy

June 2020

Department of Chemical Engineering

The University of Melbourne

Abstract

Replacing coal with natural gas is one of the feasible approaches to mitigate CO_2 emission at present. To satisfy the increasing global demand for natural gas, more research and development efforts are being put in converting the highly sour natural gas into applicable energy sources. Adsorption processes offer a promising method to remove the bulk sour component, CO_2, from high pressure sour natural gas.

Adsorptive properties of six zeolites and one silica gel (CBV-760, CBV-780, HSZ-320HOA, HSZ-350HUA, HSZ-385HUA, HSZ-390HUA, and Sorbead® WS) were characterised by various methods. Their adsorption isotherms of CO_2 and CH_4 in the low-pressure regime (0 – 10 bar) were used to determine the isosteric heat of adsorption, while the high-pressure adsorption isotherms (0 – 50 bar for CO_2 and 0 – 100 bar for CH_4) were fitted to the Toth and the Langmuir adsorption isotherm models. The model fitting parameters were further used in a rigorous simulation model to evaluate the performance of the selected adsorbents in separating a gaseous mixture with 30% CO_2 and 70% CH_4. The simulated CH_4 recovery were used as a major adsorbent performance metric. Besides, another traditional adsorbent performance indicator, IAST (Ideal Adsorbed Solution Theory) selectivity, was employed for the screening of the adsorbents. Both evaluation metrics gave different results about the performance ranking for the same CO_2/CH_4 separation application. Although HSZ-320HOA was suggested to be the best adsorbent among selected materials by the IAST selectivity, the process simulation preferred Sorbead® WS which achieved the highest CH_4 recovery (71%) among selected adsorbents.

To push the limitations of the traditional adsorbent performance indicators, a new indicator was proposed. The new indicator, adiabatic column working selectivity, contained all features that other indicators have, and also involved a new factor, the components remaining in the void gas phase. The adsorbent evaluation results of the adiabatic column working selectivity were compared with the results of other indicators and the rigorous simulation model. It was found that only the new indicator could match the results of simulations well, while other indicators

deviated more or less from the simulation results.

The new indicator was proved effective for screening the adsorbents for the application of CO_2 removal from natural gas, but to apply this indicator, two process variables, the temperature and bed composition at the end of the desorption step must be determined beforehand. To overcome this difficulty, two simplified simulation models were developed to facilitate the calculation of all critical process variables. The newly developed simplified models could determine the comparable desorption conditions as well as the rigorous simulations, but within much less computation time.

A pressure swing adsorption (PSA) plant was operated in the CO2CRC Otway CO_2 Capture Research Facility applying Sorbead® WS as the adsorbent to separate CO_2 from gas mixtures with various compositions (28 mol% to 78 mol% CO_2 balanced with CH_4) under different conditions from May 2017 to May 2019. Using the recorded process conditions, the process performance predicted by the simplified models could agree well with the actual process performances. This outcome verified the validation of the simplified models.

Overall, we found a novel adsorbent performance indicator, adiabatic column working selectivity to evaluate the performance of adsorbents for the application of CO_2 removal from natural gas at high-pressure. At the same time, with the help of a newly developed simplified verified by a real PSA plant, the calculation results of the adiabatic column working selectivity can more precisely predict and screen adsorbents for the targeted application.

Declaration

This is to certify that:

1) the thesis comprises only my original work towards the PhD,
2) due acknowledgement has been made in the text to all other material used,
3) the thesis is fewer than 100,000 words in length, exclusive of tables, maps, bibliographies and appendices.

_____

Lefu Tao

June, 2020

Publications

Journal Published:

L. Tao, P. Xiao, A. Qader, P.A. Webley, CO2 capture from high concentration CO2 natural gas by pressure swing adsorption at the CO2CRC Otway site, Australia, Int. J. Greenh. Gas Control. 83 (2019) 1–10.

Conference abstracts:

L. Tao, P. Xiao, A. Qader, P.A. Webley, Simulation Modelling of the Otway CO2/CH4 Adsorption Separation Process and Optimization, in: 14th Greenh. Gas Control Technol. Conf. Melb., 2018: pp. 21–26.

Acknowledgment

Firstly, I would like to express my appreciation to my primary supervisor, Professor Paul A. Webley, for giving me countless advice, continuous supports, and numerous discussions. Thank you for always praising me for various exotic ideas and allowing me to explore this interesting research topic at my own pace. Thank you for providing me opportunities and financial supports to attend a lot of academic activities, like the Chemeca 2018 conference in New Zealand, the 13th International Conference on Fundamentals of Adsorption in Australia, and 1st International Gas Adsorption Summer School in Greece. And what is more important, thank you for letting me work within your research group.

Then to my additional supervisor, Dr. Penny Xiao, thank you for the everyday discussion and valuable guidance throughout my three and half years' Ph.D. life. I would also like to thank Dr. Ranjeet Singh, the lab manager, for teaching me experimental techniques and knowledge of material science.

Thank you to the Australian Centre for LNG Futures for providing the funding for this research and the opportunity to attend the internal conferences in Western Australian to meet and connect people with diverse research backgrounds.

Thank you to the CO2CRC Ltd. for allowing me to participate in the CO_2 capture work in their research facility and attend many symposiums and activities that facilitated the connection with other CO2CRC researchers and members. I would also like to acknowledge the CO2CRC Ltd. for providing financial assistance to attend the 14th International Conference on Greenhouse Gas Control Technologies in Australia.

Thank you to the Department of Chemical Engineering for allowing me to tutor and teach at various subjects. Specially thank you to Professor Greg Qiao for continuously offering me the tutor position for 4 years in the subject of Reactor Engineering.

Thank you to A. Professor Kathryn Mumford for all valuable advices provided in every Ph.D. progress review meeting as my committee chair. Also, thank you to Kathryn for denoting me as the student representative of the Peter Cook Centre.

Thank you to Dr. David Danaci, Dr. Fan Wu, Dr. Yue Wu, Dr. Xin Fang, Dr. Guoping Hu, and Mr. Yongqiang Wang for the help you give me in all collaborated research work we did together.

Thank you to my friends, Fan Wu, Yue Wu, Guoping Hu, Zhe Lv, Huinan Si, Yue Sun, Changqing Zhang, Cola (the Cat) Zhang, Ge Ye, Duolong Ma, and Zihui Qiu for providing me pleasurable experiences during my Ph.D. period.

Gratefully thank you to my parents for the firm and persistent supports as my back. Your patience and love for me will never be forgotten.

In closing, I want to express my deepest appreciation to my respected wife, Mandy. The love, encouragement, company, and spiritual supports from you, as well as discussions between us in the academic area, help me overcome the difficulties and pressures in my study. This thesis would not have been possible without you.

Table of Contents

List of Figures

Chapter 2

Chapter 3

Chapter 4

Chapter 5

Chapter 6

List of Tables

Chapter 1

Chapter 2

Chapter 3

Chapter 4

Chapter 5

Chapter 6

Appendix A

Appendix B

CHAPTER 1

INTRODUCTION

1.1 Global warming and fossil fuel transitions

The issue of global warming attracted continuous attention and discussions worldwide in the last three decades. The Intergovernmental Panel on Climate Change (IPCC) founded in 1988 has published five assessment reports regarding the remedial efforts for global warming, and their latest report clearly stated that it is anthropogenic activities that have caused approximately 1.0 ^{o}C of global warming above pre-industrial levels [1]. According to the report specific to the issue of CO_2 emission from consumption of fossil fuel published by International Energy Agency (IEA), the anthropogenic carbon emission owing to fulfilling the global energy demand is the absolute key contributor of the global warming, which accounted for 74% of the total global emissions in 2015 [2]. In the meantime, the energy demand will rise by an average rate of 1.3% each year to 2040 based on the prediction of IPCC. If the world continues along the current international energy and environmental policies without any additional changes, it will inevitably further concentrate the energy-related greenhouse gas in the atmosphere [3]. To meet the essential target of Paris Climate Agreement, restricting the global temperature rise to "well below 2 ℃, … and pursuing efforts to limit it to 1.5 ^{o}C" over pre-industrial levels within the 21st century [4], multiple renewable and low-carbon fuels and technologies providing efficient and cost-effective energy are required to achieve significant emission cuts.

One of the feasible approaches to mitigate CO_2 emission is by replacing coal with natural gas, or called coal-to-gas switching. Natural gas is relatively cleaner than other fossil fuels. Theoretically, harvesting energy by burning natural gas emits around 20% fewer CO_2 than burning oil and 40% fewer than coal combustion for each unit of energy output [3]. Statistics show that nearly 10 gigatons (Gt) of CO_2 emissions were solely attributed to the coal-fired electricity generation, which accounted for around 30% global emissions in 2018. Coal-to-gas switching in the power sector could lead to an immediate emission saving of around 1.2 Gt CO_2 without major infrastructure alternations, and potential further saving if lower gas prices are accessible. Of course, it is only a short-term

remedy for the global climate change, and the emission reduction effects will fade away when a more decarbonised energy system is favoured in the future. However, coal-to-gas switching is still a valuable approach among a portfolio of options to reduce emissions, providing plenty of flexibility to the global power systems to gradually transit from high-carbon fossil fuel. Besides, while renewables are regarded as a solid solution for the global warming, the essential fuel-fired power generations as the baseload sources undertaking coal-to-gas switching can also benefit the overall emissions reductions. In the Sustainable Development Scenario that IPCC proposed to meet the Paris Climate Agreement in full, the coal-to-gas switching contributes around 8% of the overall emission reduction in the 2018 to 2040 period [3].

As the prevalence of coal-to-gas switching increases and the indigenous growth continues before the renewable replacement, the demand for natural gas of any forms (pipeline and liquified natural gas) will increase accordingly. The IPCC calculates that the global gas demand will increase by 19.9 % until 2030 and 37.3% until 2040 if following the current policies, as listed in Table 1.1. To fulfill the increment of the future demand, unconventional sources of gas are given high expectations comparing to the conventional gases. Here, unconventional gas is referred to the natural gas when it cannot be extracted from the Earth either through naturally occurring pressure, or pumping mechanisms. Sour natural gas, shale gas, tight gas, coal bed methane, and biogas all belong to unconventional gas.

Table 1.1 Global gas demand prediction under the stated policies, in billion cubic meters (bcm) [3].

Year	*2000*	*2018*	*2030*	*2040*
Conventional gas	2,318	3,004	3,293	3,694
Unconventional gas	189	933	1,426	1,711
World total gas	2,507	3,937	4,719	5,405
Change	63.7%	100%	119.9%	137.3%

1.2 Acid gas removal from natural gas

One of the major issues regarding the exploitation of natural gas resources is the

presence of associated impurities which must be separated before the transport and application of the gas. Some of the conventional gas sources and most of the unconventional gas sources could contain higher amounts of impurities. For many years, the exceeding amount of impurities have prevented those resources to be exploited due to the high cost incurred for the necessary downstream separation processes, when lower-cost conventional natural gas was available. As the global gas demand soars, as well as the number of the potential high-quality gas resources is going to decline, the previous non-attractive gas resources turn out to be more appealing to the energy industry, and consequently, more research and development efforts are being put in tackling the issues of separating impurities from natural gas.

Table 1.2 Natural gas composition in volumetric percentage (vol%) of selected gas reservoirs [5,6]

	Gorningen (Netherlands)	*Kapumi (New Zealand)*	*Uch (Pakistan)*	*Uthmaniyah (Saudi Arabia)*	*Northern Carnarvon Basin (Australia)*
CH_4	81.3	45.6	27.3	55.5	83.4
C_2H_6	2.9	5.8	0.7	18	4.4
C_3H_8	0.4	2.9	0.3	9.8	1.4
C_4H_{10}	0.1	1.1	0.3	4.5	0.5
C_{5+}	0.1	0.8	-	1.6	0.2
N_2	14.3	-	25.2	0.2	1.7
H_2S	-	-	-	1.5	-
CO_2	**0.9**	**43.8**	**46.2**	**8.9**	**8.2**

The presence of CO_2 in these sources of gas is one of the major impurities. High-quality conventional gas contains around 0 to 3% of CO_2, while the sub-quality gas reservoirs could have very high CO_2 containment up to from 30% to 80%. According to a statistic conducted by ExxonMobil, roughly half of the global proven and probable natural hydrocarbon gas reservoirs have a CO_2 content greater than 2%, and most of them are in the range 15% to 80% [7]. The compositions of some natural gas reservoirs are listed in Table 1.2. Some of the

large deposits of gas with high CO_2 contents are located in Southeast Asia, North America, and north-western Australia [7,8]. To meet the quality specifications for pipeline natural gas in different countries, the level of CO_2 has to be proceeded to less than 1 to 3 vol%, while to satisfy the specification for further liquified natural gas (LNG) processing, the CO_2 should be less than 50 ppmv (parts per million volume) [9].

Removing CO_2 from raw natural gas is a crucial step in natural gas processing. It is carried out in the acid gas removal units which separates contaminates in the dry gas such as CO_2 and H_2S. This process can also be called as the gas sweetening process. Current gas sweetening technologies that are widely used include solvent-based absorption process, solid-based adsorption processes, cryogenic condensation and membranes [10]. Each of the technologies has its advantages and shortages relative to the others.

1.3 Purpose of this work and the outline

The present study will focus on the topic regarding separating CO_2 from high-pressure natural gas by adsorption technology. The aim is to characterize novel adsorbents to have good selectivity of CO_2 over CH_4 at the operating pressure of gas sweetening process, and what's more important, to find a general and cheap way to effectively evaluate the adsorbents' process performance to help the adsorbents screening and selection.

Following key points have been covered to accomplish the objectives of the present study:

1. To characterize six zeolites and one silica gel adsorbents for CH_4/CO_2 separation;
2. To evaluate adsorbent performances through PSA process simulations;
3. To develop a new process performance indicator for adsorbent evaluations;
4. To compare adsorbent performances from existing indicators and process simulations with the new indicator;
5. To develop and validate a simplified PSA simulation model;

6. To demonstrate the performance of an actual PSA plant for CH_4/CO_2 separation.

The work in this thesis is presented as follows; chapter 2 presents an extensive literature review revolving around the application of separating CO_2/CH_4 via PSA process at high pressure. Chapter 3 characterizes the structure and adsorption properties of seven novel adsorbents, and evaluate the performance of these adsorbents using existing performance indicators and a rigorous PSA simulation. In chapter 4, a new adsorbent performance evaluation indicator is proposed. Then in chapter 5, two simplified PSA simulation models are developed to facilitate the use of the new performance indicator. The new models are then validated in chapter 7 by the experiments carried in an actual PSA plant. The final chapter presents the overall conclusions and recommendations for future work.

CHAPTER 2

LITERATURE REVIEW

This chapter is to review the existing literature over a range of topics regarding CO_2 removal from natural gas by adsorption technology. Firstly, the fundamental theories of adsorption processes are covered, including the concept of adsorption, adsorbents, and the separation mechanisms. Secondly, topics specific to the application of adsorption in natural gas processing and sweetening are discussed. This section outlines the adsorbents highlighted by their potentials of CO_2 capture from natural gas, and the reported pressure swing adsorption processes for high-pressure CO_2/CH_4 separation. Thereafter, we emphasize a particular topic, the adsorbent performance indicators which are used to evaluate and screen adsorbents for a given adsorption process.

2.1 Adsorption

2.1.1 Adsorption theory

A general definition of adsorption is the phenomenon that the molecules of fluids adhere to the surface of a solid material [11]. It should be clearly distinguished from the concept of absorption, where molecules of fluids dissolve into another fluid or solid phase.

Adsorption is a surface phenomenon that is driven by the unsaturated force acting at the solid surface due to the discontinuity of the structure [12]. So, in principle gas molecules under any pressures and temperatures can interact with the solid surface via different types of bonding. The diversity of the interaction is because both solid surface and gas molecules can vary considerably in terms of various properties. Gas molecules with different sizes, structures, or electronic properties would show different affinities to the solid surface. Also, the variation of the solid surface would also provide different types of adsorption sites.

Depending on the nature of interactions between the gas molecules and the solid surface, the adsorptive separation can be classified primarily into two types: physical adsorption and chemisorption.

In chemisorption, the adsorptive site on the solid is capable to connect the

adsorbate with covalent bonds. Such connections are strong and greatly enhance the adsorption capacity of the component with specific chemical characteristics, while in the meantime other components that are not targeted are reduced on their competitiveness for the adsorptive site. For example, the amine-modified zeolites show incredible CO_2 capacity which could be used in the applications of post-combustion capture [13–15]. However, the shortcoming is that the chemical connections require more effort to reverse, hence higher energy consumption. This drawback limits the scope of chemisorption in most process applications. It could be employed to removing critical but trace contaminants in the gas mixture, such as hydrogen sulphide [16].

Physical adsorption is more commonly applied in most of the adsorption separations. The interaction between adsorbates and adsorbent surface is governed primarily by van der Waals forces and/or coulombic forces. When the solid surface is mostly covered by nonpolar sites, the adsorbate-adsorbent interaction will be caused by the dispersion repulsion forces, the major contribution of van der Waals forces. When the solid surface is polar, and the adsorbates are of different electrostatic characteristics, such as dipole moment, quadrupolar moment, their interaction can be enhanced by the electrostatic forces. Therefore, selectivity of polar species, such as water and CO_2, over nonpolar species, like CH_4, will be shifted to the polar side.

2.1.2 Adsorbents

Since the solid surface is the place where the adsorption occurs, any solid material theoretically can act as an adsorbent. However, a solid material is normally exploited to be a practical adsorbent when it presents a huge surface area within a relatively small space. This is usually achieved when the solid material contains a complex internal structure and porosity. The porous structures inside the solid can be classified into three categories according to the dimensional size of the pore, d, via the recommendation by IUPAC: (1) micropores when d is smaller than 2 nm, (2) mesopores when d is between 2 and 50 nm, and (3) macropores when d is larger than 50 nm [17]. This classification is arbitrary under the S.I. unit scheme and was developed on the basis of adsorption of nitrogen on a wide range of material [18].

Apparently, according to geometric principles, when the pore volume is a constant, the smaller size the pore is, the larger surface area the solid will have because of the porous structure. This statement suggests that a solid material with large microporous volume is the ideal adsorbent with adequate adsorptive capacity. However, with only micropores, the mass transfer of the gas molecules from bulk gas to the solid surface would suffer from steric restriction, so that it takes too long for the adsorbate to reach the adsorptive sites. This eventually requires a longer and larger adsorption column, and consequently leads to low productivity. Of course, some adsorption applications manage to exploit the different kinetic resistances between competitive adsorbates with different physical properties to achieve a kinetic separation. This separation mechanism will be introduced in a later section. In general, a qualified adsorbent is required to provide good adsorptive capacity and kinetics simultaneously. Therefore, a solid material with a combination of pores of a range of size is suggested for practical separation processes [18,19]. The micropores in the porous solid can provide sufficient surface area and micropore volume to assure adsorption capacity, while the meso and macro-porous network offer the “high-way” for gas molecules to transfer from the exterior to the interior structure.

2.1.2.1 Activated carbon

Activated carbon is the most exploited adsorbent because of its extremely high surface area and micropore volume. Their interior structures are highly affected by the starting materials before “activated” and the activating process.

The starting materials can be coal, coconut shell, biomass, polymers and any other materials with high carbon content. Then, carbonaceous raw materials are carbonised at various high temperatures in an inert atmosphere to eventually be converted into activated carbon. In this process, all non-carbon elements within the raw materials, such as hydrogen, nitrogen and oxygen, react to produce volatile compounds and leave the system. The subsequent residual elementary carbon assembles into a network of flat carbon sheets in a random arrangement. This skeleton of carbon provides a broad spectrum of pore size, which acts as the structural foundation of activated carbon being adsorbents.

The pore size distribution in activated carbon can be manipulated by changing

different starting materials, as well as altering the heating and cooling procedures of the activation. For example, a special type of activated carbon, carbon molecular sieve with narrow pore size distribution is produced by pyrolyzing a hard coal under carefully regulated conditions [20]. Recent approaches of fine-tuning the pore size distribution of activated carbon are carried out by fixing carbon on a highly ordered template material, and then eliminating the template and maintaining the carbon skeleton as the ordered structure [21,22]. More details regarding activated carbon could be obtained from the literature [23].

2.1.2.2 Silica-gel

Silica-gel is one of the silicic adsorbents, traditionally produced by dehydrating the polymeric colloidal silica acid. The chemical composition of silica gel is as simple as $SiO_2 \cdot nH_2O$, where the water molecules present in the structure are mainly in the form of hydroxyl groups connecting SiO_2.

Similar to the activation process as activated carbon, the drying process for the silica-gel greatly alters the interior network structures. The preparation process is demonstrated in a simple sketch in Figure 2.1. Before dehydration, the chains and nets of linked tetrahedra [SIO_4] are relatively dispersed in the solution. As the water content decreases, the linked structures aggregate to form spherical particles. With further dehydration, the particles agglomerate to form a porous structure as the basic structure for an adsorbent. The bond formed within the particles by eliminating a water molecule between two hydroxyl groups makes the porous structure physically robust. The pore size distribution is greatly affected by the solution conditions, like cations present and pH, and the dehydration procedure [24].

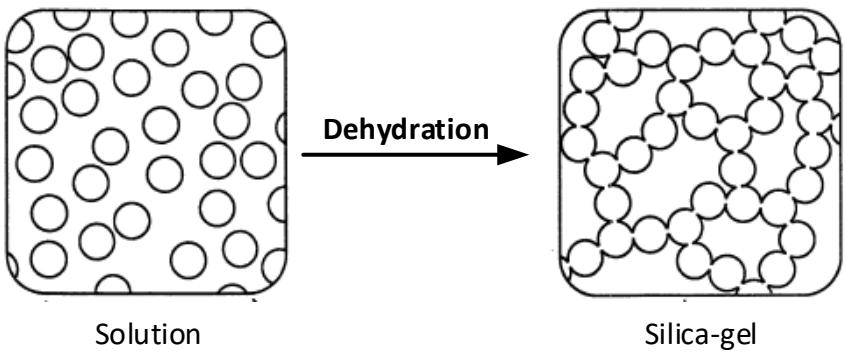

Figure 2.1. Scheme of silica-gel preparations. Recreated according to the figure from

reference [24]**.**

2.1.2.3 Zeolites

Zeolites are an important class of adsorbents. In contrast with the amorphous topology of activated carbon and silica gel, zeolites are crystalline materials.

The primary building units of zeolites are normally composed of an assemblage of [SiO_4] and [AlO_4] tetrahedra connected with shared oxygen atoms. The primary building units then construct the secondary polyhedral building units to form final three-dimensional crystalline frameworks.

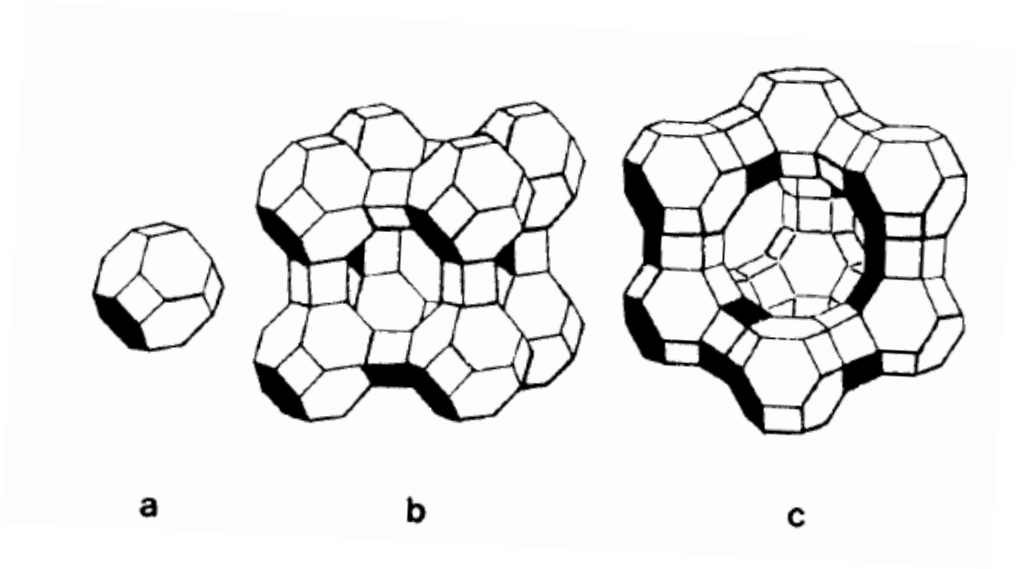

Figure 2.2. Line representations of zeolite structure from (a) primary building units to secondary polyhedral building units (b) type A zeolite and (c) type X and type Y zeolite [12]

Figure 2.2 clearly illustrates the structure of two common types of synthetic zeolites, type A and type X and Y zeolites. Each vertex of the structure is either a silicon or aluminium atom, and the lines between vertices represent the bond of shared oxygen. The primary building structure of both types are identical, which is the truncated octahedra as shown in Figure 2.2(a). The difference is that within type A zeolite the primary building units are linked via the four-member ring, while within type X and Y they are connected by the six-member ring, demonstrated in Figure 2.2(b) and Figure 2.2(c) respectively.

Because of this fundamental divergence, they have different porous configurations within their structures. The central cavity surrounded by the primary building units in type A zeolite has a free diameter of 11.4 Å, which is

accessible via the eight-member ring with a minimum diameter of 4.4 Å, while the aperture of the twelve-member ring in type Y zeolite has a diameter of approximately 7.4 Å [12]. These data of type A zeolites are only valid when the ratio between the silica and alumina tetrahedra is 1:1, as the dimensional size of the cavity would change when the composition of the zeolite skeleton varies.

Besides, due to the difference of silicon and aluminium in the valence, the [AlO_4] tetrahedra is negatively charged and requires a cation to maintain the charge neutrality. The number of cations on a secondary building unit can be changed by tuning the ratio of silica and alumina, while the type of cations can also be changed by ion exchange. This can influence the electrostatic characteristics and the porous property of the zeolites, and consequently the selectivity of the adsorbent.

2.1.2.4 Metal-organic frameworks

The final group of adsorbents, MOFs, are discovered in the last few decades. As the name indicates, the general structure of MOF is comprised of metal-centre units connected by organic linkers forming a crystalline framework. Because both the metal-containing units and the organic linkers can be functionalized or varied, the inner structure of the framework is tuneable accordingly. With specific combinations of metal-centre units and organic linkers, some MOF materials can present inherent and permanent porosity, which show great potentials of being excellent adsorbents.

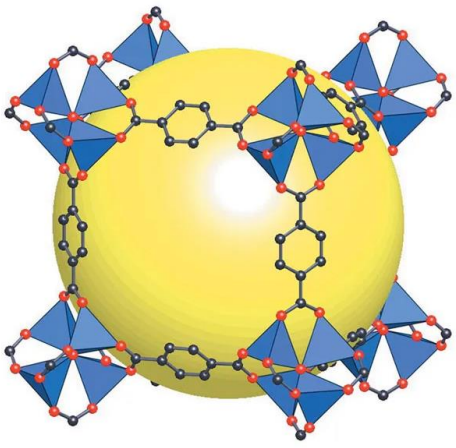

Figure 2.3. The basic structure of MOF-5 retrieved from reference [25]. **The metal-centre units [ZnO_4] is shown as the blue tetrahedra. The organic linker, benzene dicarboxylate, is illustrated as black (carbon atoms) and red (oxygen atoms) spheres. The yellow sphere**

is the resulting cavity by the MOF-5 structure, with the centre diameter of 12 Å and the aperture width of 8 Å.

Figure 2.3 demonstrates the structure of one of the earliest reported metal-organic framework materials, MOF-5 [25]. The figure shows the possibility of tuning the pore structure by varying the metal-centre units and the organic linkers. Theoretically, there are innumerable combinations of the metal-centre units and organic linkers, thus MOFs can potentially be used to satisfy any demands on the pore sizes and internal structures for a given separation application. Extensive literature can be referred to for further information regarding the application of MOFs in the adsorption process [26–28].

2.1.3 Separation mechanisms of adsorption

Gas separation by adsorption is achieved by exploiting the difference of interactions of the competitive adsorbates (or co-adsorbates) with the surface of the solid adsorbent. In the adsorption process, one component can be selectively concentrated on the solid phase while the other components are enriched in the gas phase. This selective adsorption and separation are based on three different mechanisms: equilibrium separations, kinetic separations, and molecular sieving.

2.1.3.1 Equilibrium separations

In section 2.1.1, we have presented the basic concept of how the solid adsorbents selectively concentrate one adsorbate more than the other one by chemical bonding or difference of the physical interactions. These separations are based upon the equilibrium mechanism. That is, the separation is determined by the adsorption equilibrium capacity difference among co-adsorbates on the adsorbent.

Equilibrium separation is valid when the size of the adsorbate molecule is much smaller compared to the dimensional size of the porous structure of the adsorbent, thus the adsorbates can reach the adsorptive sites without suffering significant diffusional resistances. Since the equilibrium adsorption capacity of the adsorbent is easy to determine by experimental methods and the equilibrium separation mechanism is straightforward, equilibrium separations are widely employed in industrial applications, such as hydrogen purification in steam-methane reforming (SMR) [29].

The possible drawback of the equilibrium separation is that all co-adsorbates are more or less adsorbed on the solid. Hence, when the adsorbents are regenerating to produce the extract stream, the purity will be compromised, and consequently impair the recovery of the raffinate product. This is the major technical concern of applying adsorption to the CO_2 removal from natural gas [30].

2.1.3.2 Kinetic separations

Kinetic separations, on the contrary, utilize the difference of the diffusivities instead of equilibrium adsorption loadings among co-adsorbates, such that when one adsorbate has arrived at the adsorptive sites, the other competitive one is still hindered in the network of porous channels. Therefore, the exposure time of the adsorbate mixture to the adsorbent can be adjusted to a designated value so that only the component with larger diffusivity can adsorb.

Adsorbates begin to face significant diffusional resistances when the dimensional size of the porous structures of the adsorbent is close to the kinetic diameter of the gas molecule. The kinetic diameters are related to the thermodynamic property of the gas molecule and can be calculated as Equation 2.1, where d is the kinetic diameter, l is the mean free path length of the molecule and n is number of molecules per unit volume [31]. The kinetic diameters of some common gas molecules are listed in Table 2.1.

$$d^2 = \frac{1}{l \cdot \pi \cdot n} \qquad \textbf{Equation 2.1}$$

Table 2.1. Kinetic diameters of common gas molecules[31]

Molecule	*Kinetic diameter (Å)*
H_2O	2.65
H_2	2.89
CO_2	3.3
O_2	3.46
N_2	3.64
CH_4	3.8

Kinetic separations are widely used in air fractionation to produce nitrogen from air with carbon molecular sieve as the adsorbents [32].

2.1.3.3 Molecular sieving

Molecular sieving can be regarded as an extreme case of kinetic separations. When the dimensional size of the primary pore is small enough to exclude the gas molecules with larger kinetic diameters but admit those molecules with smaller kinetic diameters, then this gas mixture can be separated by molecular sieving mechanism on that specific adsorbent. For example, Zeolite 3A has a characterized pore size of 3 Å, which is between the kinetic diameter of CH_4 (3.8 Å) and H_2O (2.64 Å), thus it is commonly employed in the natural gas processing industry to dehydrate natural gas before further treatment [33].

2.1.4 Equilibrium adsorption isotherms

The equilibrium adsorption isotherms of the adsorbates on a given solid adsorbent is a critical property indicating the equilibrium adsorption capacities. For equilibrium separation, it is the only major contributor to the selectivity of the co-adsorbates, and thus the ultimate separation results; for kinetic separation, the equilibrium adsorption capacity is required as well along with the kinetic diffusion properties to find the actual selectivity.

2.1.4.1 Pure component adsorption isotherms

The equilibrium adsorption amount, n, of a particular gas-solid pair is determined by two system variables, the temperature, T, and the pressure, P. It can be described using the following equation:

$$n = f(T, P) \qquad \textbf{Equation 2.2}$$

The adsorption amount could be expressed in a unit of $[mol/kg]$, which indicates the mole of gas adsorbed on the unit mass of adsorbent. When the temperature is constant, the equilibrium adsorption amount is only a function of pressure and the resulting $n\ vs.\ P$ curve is named as the equilibrium adsorption isotherm at a given temperature. With changing temperature, several adsorption isotherms at different thermal environments can be obtained.

The adsorption isotherms could be in six types of shapes which are classified by IUPAC as shown in Figure 2.4. The characteristics of the adsorption isotherms are related to the interior structure of the adsorbents, and the adsorbate-adsorbent interaction as well as adsorbate-adsorbate interaction. For example, the hysteresis loops in type IV(a) and type V isotherms are referred to the phenomenon of mesopore filling. The step increase in type VI could be due to the adsorbate-adsorbate interaction [17].

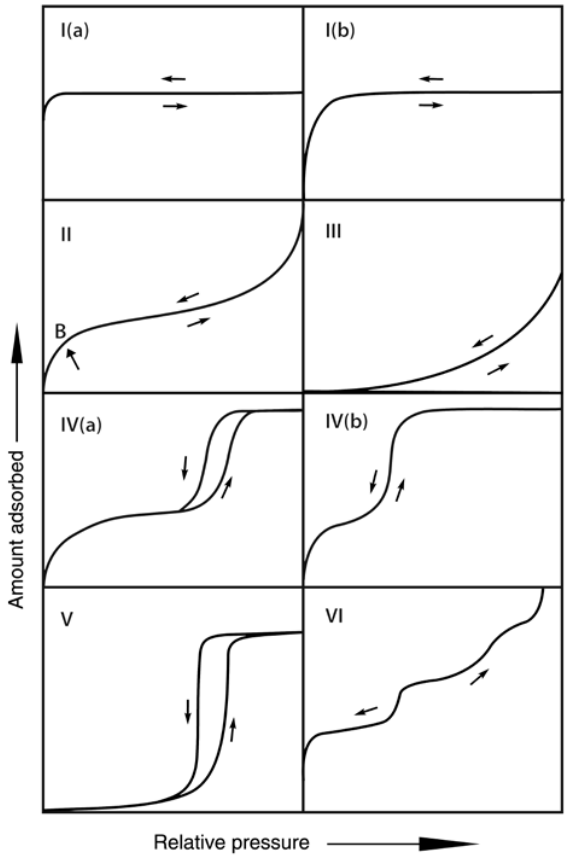

Figure 2.4. Classification of adsorption isotherms by IUPAC[17]

For the purpose of CO_2 removal from natural gas considered in this work, the adsorption isotherms (mainly adsorption isotherms of CO_2 and CH_4 at normal temperature and high pressure) are belonging to type I isotherms. Type I isotherms can be expressed mathematically according to different adsorption models. One of the most commonly used models is the Langmuir model (Equation 2.3), which is derived on a kinetic basis at equilibrium that the adsorption rate is identical to the desorption rate [34]. In the equation, n^* is the saturated adsorption amount at infinity pressure, and b is the Langmuir constant or affinity number which is related to the process temperature and the adsorption

heat Q. R is the universal gas constant.

$$Langmuir\ model: n = n^* \cdot \frac{bP}{1+bP}\ \ where\ b = b_\infty \exp\left(\frac{Q}{RT}\right) \qquad \textbf{Equation 2.3}$$

The original Langmuir equation assumes that the solid surface is uniform, so the heat of adsorption and affinity number is constant. Multisite Langmuir model (Equation 2.4) was derived by Langmuir himself as a further modification on the Langmuir model when apparent heterogeneous adsorptive sites exist in the adsorbent. Here the equation presents a case in which there are m types of adsorptive sites in the adsorbent. Although no upper limits for the number of the total sites are applied for multisite Langmuir model, as discussed by Mathias et al., there would be a negligible benefit when more than two sites are considered [35]. Thus, the dual-site Langmuir equation ($m = 2$) is frequently used.

$$n = n_1^* \cdot \frac{b_1 P}{1+b_1 P} + n_2^* \cdot \frac{b_2 P}{1+b_2 P} + \cdots + n_m^* \frac{b_m P}{1+b_m P}$$

Equation 2.4

$$where\ b_j = b_{\infty,j} \exp\left(\frac{Q_j}{RT}\right),\ j = 1,2,\ldots,m$$

Other approaches for the heterogeneity of the solid surface are introducing new empirical parameters into the Langmuir model. The Sips (Equation 2.5) and Toth model (Equation 2.6) are among the most used empirical models. The new empirical parameter t in both models reflect the degree of homogeneity of the solid surface. When they are at the value of 1, both models are reduced to the Langmuir model which indicates the surface is homogeneous. In contrast, the surface is more heterogeneous as the empirical parameters depart from 1 [18].

$$Sips\ model:\ n = n^* \cdot \frac{(bP)^{\frac{1}{t}}}{1+(bP)^{\frac{1}{t}}} \qquad \textbf{Equation 2.5}$$

$$Toth\ model:\ n = n^* \cdot \frac{bP}{[1+(bP)^t]^{\frac{1}{t}}} \qquad \textbf{Equation 2.6}$$

2.1.4.2 Mixture adsorption isotherms

Pure component adsorption isotherms are important to determine the total adsorption capacity of one adsorbate on solid. However, in practical processes,

the adsorption separation always involves at least two components. Due to the limited number of the adsorptive sites as well as the influence of interaction between gas species, the adsorption equilibrium of a gas-solid pair is undoubtedly affected in mixture adsorption.

One of the most used multicomponent adsorption isotherms is the extended Langmuir model, which was first proposed by Markham et al [36]. It is also derived based on the kinetics basis at an equilibrium state similar to the pure component Langmuir model, where the competitive adsorption rate is equal to the desorption rate for each of the adsorbate, and the resulting equation is shown as Equation 2.7. Compared with the pure component Langmuir equation (Equation 2.3), the additional terms in the denominator are the occupancy of adsorption sites by the competitive adsorbates which prevent the adsorption of the competing adsorbates.

$$Extended\ Langmuir\ model: n_j = n_j^* \cdot \frac{b_j P_j}{1 + \sum_j b_j P_j} \qquad \textbf{Equation 2.7}$$

When considering the heterogeneity of the solid surface, the adsorption of the mixture can also be described by the extended Toth model. The model equation with its modern form is modified from the original literature by Jaronice and Toth [37], and is shown as Equation 2.8.

$$Extended\ Toth\ model: n_j = n_j^* \cdot \frac{b_j P_j}{\left[1 + \left(\sum_j b_j P_j\right)^{t_j}\right]^{\frac{1}{t_j}}} \qquad \textbf{Equation 2.8}$$

Another prevalent theory aiming to address the mixture adsorption is the Adsorbed Solution Theory (AST) firstly developed by Myers and Prausnitz [38]. The central principle of AST is that the adsorbed phase on the surface of the solid can be regarded in a similar way as a fluid mixture. Therefore, following an analogue of Raoult's law, the equilibrium between the bulk gas phase and the adsorbed phase can be defined in Equation 2.9, where P_j is the partial pressure of component j in the bulk gas phase, $P_j^*(\pi)$ is the pure component equilibrium pressure subjected to the spreading pressure π, γ_j is the activity coefficient and x_j is the composition in the adsorbed fluid phase.

$$P_j = P_j^*(\pi) \cdot \gamma_j \cdot x_j$$ **Equation 2.9**

Spreading pressure, π, is a variable reflecting the reduction of the surface energy due to the increasing occupation of adsorptive sites by the adsorbed phase [39]. The spreading pressure can be estimated by the pure component adsorption isotherms. Then, following the fact that at a certain pressure and temperature, the spreading pressures of all adsorbates should be identical at equilibrium condition, the adsorption amount of each adsorbate can be calculated accordingly. The mathematical details for solving AST are not in the scope of this work and are not further detailed. Further information can be found in a range of adsorption texts [18,19].

A simple form of AST is assuming an ideal solution, thus the activity coefficients for all components are unity, and the resulting model is called Ideal Adsorbed Solution Theory (IAST) model, otherwise, the Real Adsorbed solution Theory (RAST) model is defined if the solution is non-ideal. AST offers a relatively simple way to examine the mixture adsorption isotherms and the selectivity of the solid adsorbent from the perspective of thermodynamics, especially under the assumption of IAST the mixture adsorption amounts can be determined with only pure component adsorption isotherms.

2.2 Adsorption for CO_2 removal from natural gas

2.2.1 Adsorption technology

Solid-based adsorption processes are well-developed bulk gas separation technologies in the industry. It has already been extensively applied in hydrogen production [40] and air fractionation [41]. For CO_2 removal from natural gas, the adsorption process is of great potential because it can overcome the major drawback, high regeneration energy required by the absorption process. In addition, the sorbent loss is a minor problem in the regular adsorption process. No chemical degradation nor entrainment of solid is an issue of concern if a reasonable process design and adsorbent selection is conducted.

In an adsorption application, the feed gas stream passes through a bed packed with adsorbents, where the gas molecules with a stronger affinity to the adsorbent will be selectively adsorbed. The raffinate product will contain less

strongly adsorbed components so that the weakly adsorbed component is enriched. When the adsorbent in the bed becomes saturated with the strongly adsorbed component, the feed gas is then disconnected, and the saturated bed is regenerated. In terms of the adsorption column regeneration methods, the regular adsorption processes can be briefly divided into a few categories: pressure swing adsorption (PSA) that enables the adsorption-desorption cycle by changing the pressure in the column, and temperature swing adsorption (TSA) that closes the loading-unloading cycle by employing heat duty to change the column temperature. To ensure a continuous operation, when one bed is under regeneration, a secondary parallel adsorption bed with the same configuration is switched to the adsorption step. This scheme of operation is known as the adsorption operation cycle.

PSA is deemed a promising alternative technology for acid gas sweetening process because it is inherently adapted to the high-pressure natural gas feed. The large pressure difference between the natural gas reservoirs and normal atmosphere can directly be exploited as the driving force for the adsorptive separation, so that only a small amount of energy is needed for the auxiliary units to keep the cyclic operation running. The potential of low energy consumption operation by the adsorption process will bring significant economic and environmental benefits over conventional technologies.

However, as far as is known, adsorption-based technology has not been applied for CO_2 removal from natural gas at large scale. This could be attributed to the selectivity loss of the adsorbents under high operating pressure. For conventional adsorbents, the CO_2 molecule has a stronger affinity because of its quadrupole moment, hence, CO_2 tends to become saturated at a lower pressure than CH_4, which does not have any dipole or quadrupole moment. This leads to a very high selectivity of CO_2 over CH_4 in the low-pressure regime, which has been reported in previous studies [42]. But as the total pressure rises, the competitiveness of CH_4 on the adsorptive sites is strengthened, while the adsorbed amount of CO_2 has plateaued at the saturated amount. Therefore, the selectivity of CO_2 over CH_4 keeps decreasing as pressure increases. This undesired effect becomes the most challenging issue in adsorptive gas sweetening technology.

Two strategic pathways are aiming to improve the overall feasibility of the adsorptive CO_2/CH_4 separations for researchers and engineers to follow.

The first one is to modify the configuration of the adsorption process. The 'configuration' here refers to sophisticated adsorption cycle arrangements and equipment with specific designs adapted to the adsorption cycle. The existing adsorption processes for CO_2/CH_4 separation are reviewed in section 2.2.3.

The other pathway is to improve the performance of the adsorbents. This does not rely merely on finding new materials. It is also important to develop a new scheme to evaluate the materials under practical conditions. Many novel materials have been reported highlighting their potential to separate CO_2 from high-pressure natural gas, which will be presented in section 2.2.4. However, most of them were assessed either by the established criterion which was not designed for evaluating the adsorbents' performance under a high-pressure process, or in a specifically designed process that lacks generality. The absence of a viable and accurate evaluating measure results in material researchers developing numerous adsorbents with overstated potential and engineers being misled on process design from choosing non-optimal adsorbents.

2.2.2 Existing adsorption processes for CO_2 removal from natural gas

Bulk CO_2/CH_4 separation adsorption processes are prevalent in the application of upgrading biogas and landfill gas. Santos et al. carried out a biogas upgrading process on a two-bed PSA system [43]. Y.T. Kang et al. used a four-bed PSA experimental apparatus to separate CO_2 from biogas with a composition of 54.9% CH_4 and 45.1% CO_2 [44]. A good review on this specific topic was conducted by Grande [45]. However, for most of the landfill gas and biogas upgrading applications, the highest pressure during the process was below 5 bar, which was far below the practical pressure for the application to natural gas sweetening.

An early patent for bulk CO_2/CH_4 separation by adsorption was assigned by John in 1973 [46]. The feed stream for this application was at 1,000 psia (68.9 bar) and comprised of 46.6% methane and 52.6% carbon dioxide balanced with other minor components. But the actual performance was not mentioned in the patent description. Grande and his colleagues have recently completed studies on high-

pressure CO_2/CH_4 separation using PSA processes [30]. They used activated carbon as the adsorbent for natural gas sweetening and the separation was achieved by the kinetic separation mechanism. A complex 12-bed 15-step PSA operation cycles were designed to treat a natural gas feed stream with 10% CO_2 at 70 bar. The light product was of a purity of 97.8% CH_4, which satisfied the specification for piping natural gas transportation. The purity of the CO_2 product was 84.5%, which implied that the recovery of methane of the system was around 98.3%. However, as the authors pointed out, the economic consideration of this PSA unit was greatly compromised because of the huge footage requirement for a 12-column PSA plant. Besides, when comparing with the conventional absorption process, the loss of valuable methane along with the extracted heavy product in adsorption is also a significant detraction.

There are very few practical industry cases available for CO_2/CH_4 separation by adsorption. One of the early patents assigned by Air Products & Chemicals is to remove CO_2 from natural gas using carbon-based porous materials in a pressure-vacuum swing adsorption process at a pressure of up to 35 bar (500 psia) [47]. Engelhard (now BASF Catalysts) applied their Molecular Gate™ technology initially for nitrogen rejection from natural gas using pressure swing adsorption processes, and later successfully for CO_2 separation from natural gas as well [48]. The proposed adsorbents for this technology was a type of synthetic titanosilicate ETS-4. Xebec Adsorption Inc. developed a new approach named Rapid Cycle PSA (RCPSA™) [49], which significantly reduced the total footprint of the separation units. Instead of bulky piping and valves, RCPSA™ used two rotary valves in a compact and integrated system, which allowed similar throughput but only in 1/20 of the conventional PSA process footprint. ExxonMobil refinery has built and operated a prototype of RCPSA™ units for obtaining high purity hydrogen production, and theoretically, it could be repurposed for natural gas sweetening.

2.2.3 Adsorbents for CO_2 removal from natural gas

In Section 2.1.2, we have reviewed the categories of adsorbent material for general adsorption process. Regarding the application of CO_2 removal from natural gas, materials of zeolites, silicate materials, carbonaceous materials, and

MOFs were reported to be feasible as the adsorbents for CO_2/CH_4 separation under high pressure. Comprehensive reviews of most reported adsorbents published before 2015 for natural gas sweetening process can be found in two references [50,51].

Upon reviewing the reported adsorbents for CO_2/CH_4 separation, it is disappointing to find that although several conventional porous adsorbents and novel materials have been highlighted by "good" selectivity of CO_2 over CH_4, most of them only provide adsorption isotherm measurements up to atmospheric pressure and at one temperature. Natural gas sweetening by adsorption processes need to operate within a wide pressure range, from the gas reservoir pressure around 100 to 200 bar, to the desorption pressure of 1 to 5 bar. The high-pressure adsorption behaviour cannot be extrapolated accurately with only low-pressure adsorption isotherm data. Besides, the very large pressure swing within the adsorption cycle implies a thermal effect of the adsorption-desorption cycle on the adsorbent, which would amount to 10's of degrees Celsius, significantly influencing the adsorption amounts. The adsorption isotherms at one temperature again are far from enough to predict the actual performance of one adsorbent under operating conditions. Therefore, extra efforts should be paid by future materials research on this topic to provide a completed dataset of adsorption isotherms. Webley and co-workers have specified completed adsorption isotherms data as under at least two temperatures and up to actual operating pressures [52].

Table 2.2 provides a summary of various adsorbents for CO_2/CH_4 separation that have completed data sets and are newly published from 2015 to 2020.

Table 2.2. Summary of existing publications with high pressure (>2 MPa) adsorption isotherms data published in 2015 to 2020

Adsorbent	*Types*	*Temperature (K)*	*Pressure*	*Ref.*
CMS KP 407	Carbonaceous	298, 343	CO_2: 0 to 3 MPa CH_4: 0 to 6.5 MPa	[53]
AC Monoliths	Activated carbon	298, 313, 343	CO_2: 0 to 3 MPa CH_4: 0 to 4 MPa	[54]
AC beads	Activated	293, 303, 333,	0 to 4 MPa	[55]

	carbon	363		
Mordenite *Zeolite β* *Zeolite γ* *ZSM-5*	Zeolite	308, 323, 338	0 to 20 MPa	[56]
ZSM-25 *PST-20*	Zeolite	298	0 to 2 MPa	[57]
ZIF-8 *ZIF-14* *ZIF-71*	MOF	273, 303	CO_2: 0 to 5 MPa CH_4: 0 to 10 MPa	[52]
GrO@MIL-101 composite material	MOF	298, 303, 308, 313	CO_2: 0 to 2.5 MPa	[58]
UTSA-16	MOF	298, 313, 338	CO_2: 0 to 4 MPa CH_4: 0 to 5 MPa	[59]
MIL-101	MOF	263, 273, 283, 293, 303, 313	0 to 0.8 MPa	[60]
ZIF-8 *AL-BDC*	MOF	298, 323, 348	0 to 5 MPa	[61]
SBA-15	Silicate	298	0 to 4 MPa	[62]
COP-1 (covalent organic frameworks)	Others	298, 318, 328, 338	CO_2: 0 to 5.5 MPa CH_4: 0 to 10 MPa	[63]
Zeolite 5A - MOF74 composite material	Hybrid	298	0 to 2 MPa	[64]
Zeolite 13X	Zeolite	180, 220, 269, 323, 373, 473	CO_2: 0 to 6 MPa CH_4: 0 to 8 MPa	[65]
UiO-66(Zr)_(COOH)$_2$	MOF	180, 200, 270, 303, 333, 373	0 to 6 MPa	[66]

2.3 Adsorbent performance indicators

The selection of the adsorbent is absolutely the cornerstone of the adsorption process because all engineering aspects must be designed on the basis of the actual performance of the adsorbent. The adsorption isotherm measurements can present the amount of every component of interest adsorbed on the adsorbent under a given condition, but it is only the starting point for adsorbent assessment. Further data treatments are required to properly reveal the separating ability of adsorbents. The problem of how to apply the available adsorption isotherms data to develop an indicator to grade the adsorbent

quantitively has always been debatable. Numerous and diverse adsorption performance indicators discussed in this section have been defined by researchers and proved valid for some specific adsorption processes.

2.3.1 Evaluating adsorbents by process performance

The natural way to evaluate an adsorbent is to determine the relative success of an adsorption process with the selected material as the core adsorbent. The results of an adsorption process are generally presented as the key component's purity and recovery, with additional points-of-interest depending on the applications. The purity concerned here is the purity of methane in the permeate gas stream, which is methane concentrated, The recovery is the molar percentage of methane in the raffinate product compared to the total molar amount in the feed stream.

For natural gas sweetening, the purity of the sweet gas product stream is a primary requirement, for the CO_2 level of the product is limited to below a certain percentage to meet the downstream specification. The recovery of the valuable component, methane, should be as high as possible in terms of the economic consideration.

Additionally, the release pressure of the removed acid gas stream is also a matter of concern. It must be re-pressurised for CO_2 sequestration [67], or food-grade CO_2 [68]. No matter which destination the CO_2 rich stream ultimately heads to, it is advantageous for this stream to be released from the gas sweetening unit at as high a pressure as possible for energy savings in future compression.

In summary, the evaluation criterion for a natural gas sweetening process can be summarised in a statement: *on the premise of methane purity reaching the product specification, the recovery of methane should be as high as possible, and a higher pressure of the CO_2 rich stream would be a bonus*. Note that the process evaluation here is only at the level of direct process results which aims to estimate the performance of the adsorbents. Comprehensively evaluating a process from the economic and technical aspects would be an additional feature.

Strictly speaking, in order to check one adsorbent's performance in a process in the context of the aforementioned statement, a rigorous process simulation or an

experiment must be conducted. In such a case, any attempts to evaluate all potential materials for a given application would be a tedious and time-consuming task. Therefore, instead of a countless number of process simulations or trial experiments, researchers turned to developing new adsorption performance indicators in a relatively simple and direct form to initially screen the adsorbents to confine the candidate pool of adsorbents or directly determine the best suitable adsorbent.

2.3.2 Heavy component equilibrium loading

The simplest adsorption performance indicator which was used initially is the equilibrium adsorption amount of the heavy component at the feed gas conditions [12]. The indicator might only work when the light component does not adsorb much, or the feed gas is concentrated with the heavy component so that the adsorption of the less adsorbed component is negligible. That is, the adsorbent was solely evaluated by its affinity to the most adsorbed component. Any process factors are not considered by this method.

Today, this simple indicator still has its application in some special scenarios. When the capacity of the most adsorbed component on a novel adsorbent is much higher than that of other previously reported adsorbents, the heavy component equilibrium loading is then the simplest way to display their dominant advantage. For example, many MOF materials are reported as the potential CO_2 removal adsorbents because of their extraordinarily large CO_2 capacity [69].

2.3.3 Selectivity

Another early indicator, separation factor, was used when the adsorption isotherms were linear. It was defined as the ratio between the linear distribution coefficients of the strongly and weakly adsorbed components [70]. Knaebel presented an alternative expression of the same indicator, the ratio of Henry's coefficients as in Equation 2.10 [71]. The Henry's coefficient, H_i, could be calculated as the slope of the isotherms at zero adsorption in Equation 2.11, where n_i is the adsorption amount of one component, and P is pressure.

$$\alpha_H = \frac{H_B}{H_A}$$ **Equation 2.10**

$$H_i = \lim_{n_i \to 0} \left(\frac{dn_i}{dP}\right)$$ **Equation 2.11**

For simplicity, in this work we designate the strongly adsorbed component in a binary gas mixture as component 'A', while the weakly adsorbed component as component 'B' as in Equation 2.10.

Theoretically, Henry's coefficient represents the affinity of adsorbate molecules toward adsorbent at zero surface coverage. It is correlated with purely the interaction between adsorbate and the adsorbent surface, without the influence of adsorbate-adsorbate interaction and competitive adsorption. Thus, Henry's Selectivity is only valid when the adsorption system is under a low-pressure condition and the adsorption isotherms are almost linear. Under such conditions, the ratio of the Henry coefficient is approximately equal to the ratio of adsorption amount under equimolar feeding condition.

It was commonly used in the adsorption application when the operating pressure was relatively low and the fluid was in dilute concentration [72,73]. As the conditions of the adsorption process becomes more complicated and the adsorption isotherms are no longer close to linear, the Henry Selectivity is insufficient.

In separation technology, relative volatility, α_{AB}, is commonly used when a phase shift during the separation is involved. It is calculated as the composition ratio of two specified components in one phase over the other phase (Equation 2.12), where x_i is the composition in the liquid phase and y_i in the gas phase. Since the adsorption processes also include the phase shift from the fluid phase to the solid phase, the relative volatility is regarded as an important selectivity indicator [74].

$$\alpha_{AB} = \frac{x_B}{x_A} \cdot \frac{y_A}{y_B}$$ **Equation 2.12**

Yang suggested an improved selectivity indicator which is analogous to the relative volatility but is more suitable in the scope of solid-based adsorption [12].

Yang's selectivity, α_Y, is defined by Equation 2.13, where y_i is the composition of one component at gas phase.

$$\alpha_Y = \frac{n_B(P,T,y_B)}{n_A(P,T,y_A)} \cdot \frac{y_A}{y_B} \qquad \textbf{Equation 2.13}$$

In this indicator, the solid loading terms could be calculated as the single component adsorption amounts. But to approach the actual conditions, mixture adsorption amounts, which account for the competitive adsorption, are more commonly used. Yang's ideal selectivity is probably one of the most employed metrics because of its concision and practicability, and nowadays it is frequently referred as the ideal selectivity.

The primary drawback of the ideal selectivity is that it only considers one condition but neglects the cyclic operations which is the nature of the adsorption process. After one cycle of adsorption and regeneration, the loading on the adsorbent cannot be completely removed since the pressure inside the adsorption column can never drop to absolute zero. The same logic applies to the compounds remaining in the gas phase in the void space of the column. The factor of the residual loading after regeneration is equally as crucial as the loadings under the adsorption condition. It has a significant impact on the effective amount of gas that can be processed by a single unit of adsorption bed. It has been widely reported that an adsorbent's performance has been severely impacted by insufficient regeneration at regular desorption conditions [51,75,76]. Therefore, the ideal selectivity which only focuses on the feed condition is not sufficient for screening adsorbents in a high-pressure cyclic adsorption process.

Working selectivity has been used alternatively to consider the regeneration of the adsorbents. The working selectivity is calculated as the ratio between the working capacity of the heavy component and that of the light component (Equation 2.15), where the working capacity is defined as the difference in the equilibrium loading of one adsorbate between the adsorption condition and desorption condition (Equation 2.14).

$$WC_i = n_i\left(P_{ad}, T_{ad}, y_{i,de}\right) - n_i\left(P_{de}, T_{de}, y_{i,de}\right) \qquad \textbf{Equation 2.14}$$

$$\beta = \frac{WC_B}{WC_A}$$ **Equation 2.15**

As its name indicates, the working selectivity is meant to display the adsorptive preference under the actual working conditions. However, unlike the adsorption condition, which is normally identical to the feed gas condition, the desorption condition is hard to define without simulations or experimental process running.

At least three process factors are essential to determine the desorption condition: pressure, temperature, and the gas phase concentration. The desorption pressure is the easiest one, as it usually comes from the process specification.

The temperature at the desorption step is difficult to estimate without experiments or simulations. Harlick et al. proposed an indicator named expected working capacity, which assumed isothermal operation, so that no temperature swing between the adsorption and desorption conditions occurs [77]. That is, the T_{ad} and T_{de} in Equation 2.14 were assumed to be identical. The isothermal assumption is reasonable when the pressure swing is small, or when the adsorption bed is on the lab scale such that the thermal conduction is large enough to dissipate the heat or cold wave from the inside of the column due to the adsorption/desorption energy.

For an industrial PSA process, however, it is usually operated close to the adiabatic condition. Adiabatic working selectivity was firstly suggested by Ackley et al. [78], where the desorption temperature T_{de} was not identical to the adsorption temperature T_{ad}. Instead, T_{de} needed to be determined by process experiments or simulations. Zhang and Webley found a simple method to calculate the desorption temperature, therefore, allowing them to screen a batch of adsorbents at different feed condition rapidly [79].

Note that none of the above researches calculated the gas composition at the desorption condition, $y_{i,de}$. They either used the predetermined product composition or sometimes the feed composition.

2.3.4 Lumped parameters

Instead of the basic indicators, some lumped parameters were suggested by

researchers aiming to cover all adsorptive features in a single parameter.

Notaro et al. invented an 'adsorption figure of merit' (AFM) as shown in Equation 2.16 including three factors that they believed to be strongly related to the process performance. The factors considered are the working capacity of the heavy component, the ideal selectivity at the adsorption conditions, and the ideal selectivity ratio between the adsorption and desorption conditions [80].

$$\gamma_{AFM} = WC_B \cdot \alpha_{Y,ad} \cdot \frac{\alpha_{Y,ad}}{\alpha_{Y,de}} \qquad \textbf{Equation 2.16}$$

Another lumped indicator, the sorbent selection parameter, was proposed by Rege and Yang. It was defined as the product of the relative volatility and the working selectivity as shown in Equation 2.17 [81].

$$\gamma_{R\&Y} = \beta \cdot \alpha_{Y,ad} \qquad \textbf{Equation 2.17}$$

Although the significant impacts from the temperature change were realized by the authors, the isothermal assumption was made for both the AFM and Rege and Yang's separation factor. The composition of the bed at the desorption step was assumed as being the same as the heavy product. This approach could provide good direction in screening out a better adsorbent for a particular set of operating conditions. But it was likely to fail when estimating the performance of any adsorbents with large heats of adsorption.

The latest lumped indicator, adsorbent performance indicator (API), was proposed by Wiersum et al. [82]. It was defined as Equation 2.18. The API introduced the heat of adsorption of the heavy component (ΔH_B) into the indicator to include the thermal effect. Because a large thermal effect is adverse to the separation performance, the heat of adsorption term is placed in the denominator. In the meantime, the author highlighted an important feature of the API that different weights (the indexes a, b, and c in Equation 2.18), not necessarily all identical as the other lumped indicators, could be applied to each term. Hence, the API could be adapted to different objectives by selecting proper indexes for any given processes.

$$\gamma_{API} = \frac{(\beta - 1)^a \cdot WC_B^b}{|\Delta H_B|^c}$$ **Equation 2.18**

2.3.5 Validity of the indicators

The applicability of all indicators was demonstrated by their reporters in certain adsorption applications, but the generality still needed to be examined. Recently, Rajagopalan et al. evaluated the capability of most of adsorbent metrics to screen four diverse adsorbents for post-combustion CO_2 capture [83]. Their results showed that only a few metrics could provide the right ranking of performance, but the magnitudes difference of these metrics between different adsorbents did not agree with their actual process performances. Similar results could be expected in the application of CO_2/CH_4 separation.

The limitations discussed above indicated that the existing adsorption metrics which only consider the adsorbent properties, i.e. equilibrium loadings, working capacities, and selectivity, are not capable of accurately predicting the adsorbent process performance. Those common compromises, such as isothermal assumption and the pre-set composition of the column at the desorption step, and other unknown factors need to be included for a more accurate screening metric.

CHAPTER 3

NOVEL ADSORBENTS FOR CO_2/CH_4 SEPARATION

3.1 Introduction

The adsorbent is a key parameter in the adsorption process. In this chapter, we will characterize the adsorption properties of seven novel adsorbents. The adsorption properties measured in this chapter include the textural property of the internal structure, the intermediate pressure adsorption isotherms of both CO_2 and CH_4, the isosteric heat of adsorption at low coverage, the high-pressure adsorption isotherms and IAST selectivity calculated by the isotherm fitting parameter. Also, a process simulation is employed to evaluate the adsorbent performance to compare with the prediction of IAST selectivity.

3.2 Materials and methods

3.2.1 Adsorbents

Commercial type Y zeolites of CBV-760, CBV-780 in powder form were obtained from Zeolyst International. Ultra-stable type Y zeolites of HSZ-320HOA, HSZ-350HUA, HSZ-385HUA, and HSZ-390HUA in powder form were obtained from Tosoh Co. (Japan). Protons are the predominant cations, with a minor amount of sodium cations, in the zeolitic framework of all selected zeolites. These zeolites are strong adsorbents of CO_2 but not as strong as NaX zeolite – as a result, they are potentially better candidates for PSA application (as opposed to VSA application which requires sub-atmospheric pressure operation).

Silica-gel, Sorbead® WS, was obtained from BASF catalysts. It is in a form of light-yellow, hard, spherical beads with a uniform diameter of an average of 2 mm. All materials were used as received without further purification for high-pressure gas adsorption measurements.

3.2.2 Materials characterization

For the purposes of confirming the crystallinity of the sample, lab powder X-ray diffraction (PXRD) measurements were carried out on a Philips Analytical PW1140/90 X-ray diffractometer (Philips Analytical, Netherlands) with Cu Kα radiation. The step size for the measurement is 0.02 ° with a scanning rate of 1 °/min.

Surface areas, pore size distributions and porous volumes of the adsorbents were characterized via volumetric adsorption methods carried out on a 3Flex instrument (Micromeritics Instrument Corporation, USA). N_2 adsorption measurements of all selected zeolites at 77.3 K were conducted with a liquid nitrogen bath. The equilibrium at each pressure point was checked by the pre-set equilibrium criterion and the interval time. After a period of 10 intervals, the pressure change in the measurement chamber is calculated and compared with the average pressure during the period. When the rate of change is less than 0.01%, the adsorption amount is recorded as the equilibrium amount at the corresponding pressure. The "interval time" in this work was set to be 10 seconds.

Before the adsorption measurements, samples were degassed under a vacuum level below 1.33×10^{-2} Pa at 373.15 K for 2 hours followed by another heating period to 623.15 K for a minimum of 12 hours at the same vacuum level. The temperature is ramped to rise incrementally (10 K per minute) to the objective degassing temperature, to prevent the zeolitic framework collapsing from the rapid vaporization of the adsorbed water in the porous structures.

Ultra-high purity helium (>99.995%, BOC Australia) was used to determine the adsorbent volume in the measurement cell, and ultra-high pure N_2 (>99.999%, BOC Australia) was used to characterize these zeolites.

3.2.3 Adsorption isotherm measurements

3.2.3.1 Volumetric isotherm measurement at intermediate pressure ranges

Adsorption isotherms of both CO_2 and CH_4 up to a pressure of 10 bar on selected adsorbents were carried out on an ASAP 2050 gas adsorption instrument(Micromeritics Instrument Corporation, USA). Isotherms at three temperatures, 303 K, 313 K, and 333 K, were measured. The measurement temperatures were maintained by a thermostatic bath (Julabo GmbH, Germany). The equilibrium interval, of the same function as described in the structure characterization section, was set to be 10 seconds. Sample activation and re-degassing between isotherms measurements at different temperatures followed a similar procedure.

Ultra-high purity CH_4 (>99.995 %vol) was provided by BOC Limited Australia.

Ultra-high purity CO_2 (>99.995 %vol) were obtained from Coregas Pty. Ltd., Australia.

3.2.3.2 Gravimetric isotherm measurement at high-pressure ranges

Adsorption isotherms up to 50 bar for CO_2 and 100 bar for CH_4 of all studied adsorbents were measured on a magnetic suspension balance (MSB) system (Rubotherm GmbH, Germany). Isotherms were measured at three temperatures, 303 K, 313 K and 333 K. The temperature of the sample chamber and the balance components were maintained by a thermostatic bath (Julabo GmbH, Germany) with polydimethylsiloxane (PDMS) as the heat transfer fluid. The precision of the temperature control is within ±0.02 K.

All solid samples were directly taken out from their commercial packing and loaded into the sample container in the MSB system. A general degassing procedure was used to remove impurities from these materials before isotherm measurements: the sample was heated *in situ* under vacuum firstly to 393.15 K for 2 hours, followed by 453.15 K for 1.5 hours and eventually 623.15 K for 8 hours. The vacuum in the sample chamber could reach to a level below 1 kPa. The vacuum reading here is limited by the resolution of the pressure transmitter installed in the system. Between each adsorption measurement at a temperature, the adsorbent was also regenerated following the degassing procedure.

After degassing and activating the adsorbent, the adsorption isotherm measurements were carried out by gradually introducing adsorbates into the measurement chamber in a series of increasing pressure points. At each pre-set pressure level, the adsorption equilibrium was considered to have been reached when the pressure inside the measuring chamber remained unchanged for at least 30 minutes. Then, those balance readings at the end of the equilibration period were used to calculate one isotherm data point.

The resolution of the MSB is 0.00001 g, with an accuracy over the weighing range of ±0.02 mg. The temperature of the sample cell was measured by a Pt100 3L thermocouple probe K (Jumo GmbH & Co. KG, Germany) with an accuracy of ±0.015 K within the operating temperatures. The pressure within the measurement chamber is monitored by two different Druck pressure transmitters (GE Measurement and Control Solutions, Germany). One’s measurement range

is from 0 to 40 bar with a resolution of 0.01 bar for intermediate-pressure measurement, and the other is from 0 to 500 bar with a resolution of 0.1 bar for high-pressure measurements, respectively. The data log software as well as the instrumentations of the apparatus will automatically shift to the other pressure transmitters at the crossover pressure, 36 bar.

As indicated above, the high-pressure adsorption isotherms are measured by a gravimetric method. The excess adsorbed amount at a certain pressure can be directly read from the balance reading. But to obtain the absolute adsorbed amount, the volume of the solid sample and the density of the gas must be determined at the same time.

The solid volume, which is the skeleton volume of the solid bearing the buoyancy force from the surrounding gas, was determined by helium measurements at 313 K. This temperature value was considered as the average temperature of the isotherm measurement. Therefore, a helium experiment was conducted at only one temperature. Helium was injected into the measurement cell to a series of pre-set pressure values up to 50 bar by the automatic gas dosing system. At each pressure, 10 minutes were allowed for the sample to achieve the thermal and motion equilibrium in the measurement cell. The balance readings, as well as the temperature and pressure inside the measurement cell, were recorded every 2 minutes. At the end of equilibrium for one pressure point, an extra data logging was conducted. By completing the helium experiment, the buoyancy volume and the accurate mass of the sample under vacuum can be obtained by linear fitting of the measured helium density and the apparent mass from the balance readings. The determination method will be described in the next section.

3.2.4 PSA process simulation

To evaluate the process performance of selected adsorbents for the CH_4/CO_2 separation, we employed a nine-step PSA cycle with the help of the commercial simulation toolkit, Aspen Adsorption V10 (AspenTech, USA).

The one-bed approach was applied in the simulation, which means that only one adsorption bed was simulated rigorously. The other interactive beds shown in Figure 3.1 were treated as stack information storages (First-In-First-Out). They can store the mass, temperature and pressure stream information coming from

the simulated bed temporarily. When the main bed is supposed to receive the material stream, the interactive bed can return the information to complete the adsorption cycle.

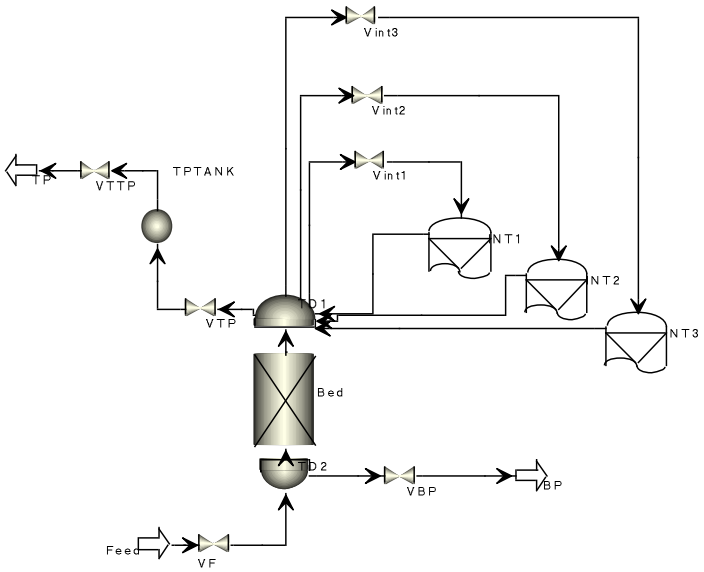

Figure 3.1. **An illustration of the one-bed approach in Aspen Adsorption.**

One great advantage of the one-bed approach is that it saves a great amount of CPU time. In our case, it is a good short-cut to estimate the performance of the adsorbent using only around 1/6 of the computation time without causing significant errors. In addition, another benefit of the one-bed approach is that the consideration of inter-bed step synchronization is not needed in this stage. To enable continuous operating and a programmable control cycle, the step switch time of one bed is under the constraints from other beds in a real PSA cycle configuration. To achieve synchronisation for all steps in the shortest time, one adsorption bed, for instance, has to be set as idle (doing nothing) to wait for the other bed to finish its current step before they can interact with each other [84]. This cycle organization requires extra efforts but contributes little when the simulation is only for adsorbent evaluation. In the one-bed approach, real bed interactions are not included, so that the step times can be adjusted to any numbers. It provides an ideal environment to assess the performance of an adsorbent within any possible cycles.

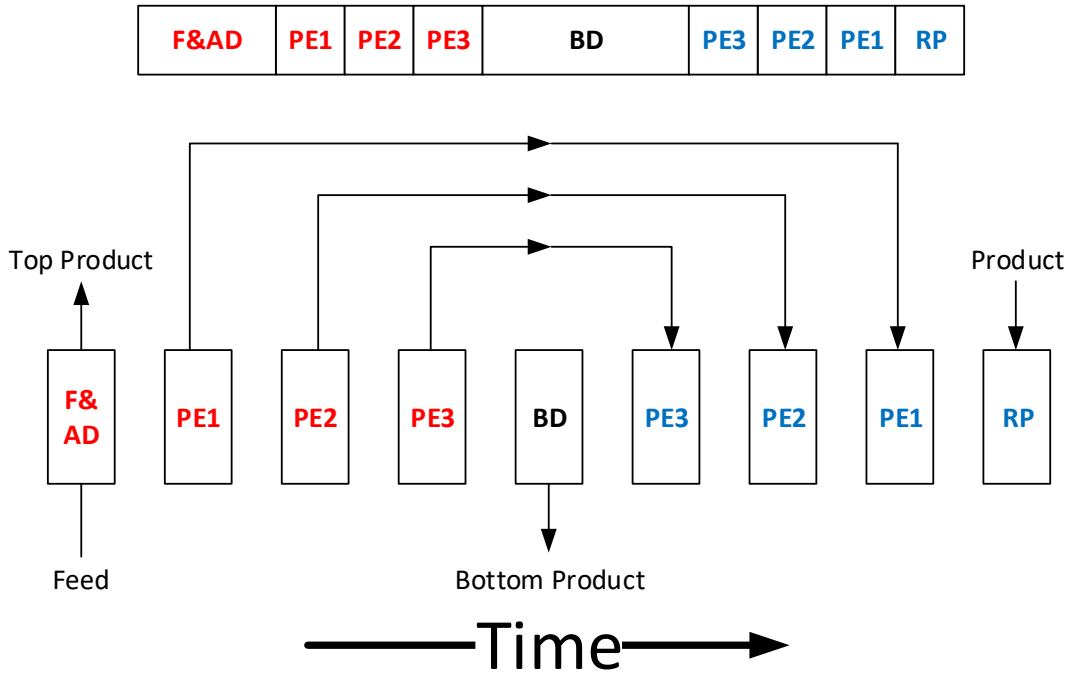

Figure 3.2. **Cyclic configuration of one adsorption bed. F&AD – Feed and adsorption, PE – Pressure equalization, BD – Blowdown, RP – Re-pressurization. The arrow direction refers to the gas stream flowing direction.**

The adsorption cycle used to evaluate the adsorbents in this work is a 6-bed 9-step cycle. The cycle consists of feed & adsorption step, three pressure equalization steps, desorption (blowdown) step, and top product re-pressurization step. A detailed outline of the cycle is shown in Figure 3.2. The effect of the numbers of pressure equalization steps was studied by Yavary et al recently [85]. Increasing the pressure equalization steps will improve the recovery of the light product while worsening the purity. Since in the application of CO_2 removal from natural gas, the recovery of the methane is of more economic significance than the purity, we chose three pressure equalization steps in the cycle. More pressure equalization steps could further improve the recovery of CH_4, but the beneficial effect due to extra increments would be reduced while the associated cost, such as higher capital investment and lower throughput per adsorption column, becomes dominant.

Table 3.1. **Bed characteristics and operating conditions used in the Aspen Adsorption Simulations**

Parameters	*Value*
Packing length (mm)	600

Internal bed diameter (mm)	80	
Feed pressure (bar)	50	
Feed temperature (K)	313	
Feed composition	70% CH_4 / 30% CO_2	
Desorption pressure (bar)	1	
Methane product purity specification	95% CH_4	
Adsorbents	**Zeolites**	**Sorbead® WS**
Packing bulk density (kg/m^3)	750	800
Particle size (mm)	2	
Inter-particle voidage	0.37	
Intra-particle voidage	0.54	

The adsorption bed parameters as well as the process specifications are listed in Table 3.1. The dimensional size of the adsorption bed is not arbitrary and corresponds to the actual size of the adsorption bed we used in a CO_2/CH_4 adsorptive separation demonstration rig [86]. It should be noted that the primary objective of the simulation model is to evaluate the relative merits of the multiple adsorbents, hence, the geometric property of the adsorption bed is not a determining factor.

The pressure, temperature and composition of the feed gas mixture are also the average value of the practical conditions in the demonstration plant, which we will discuss in a later chapter. This ensures that we can make a meaningful comparison between the demonstration plant and the simulation under the same operating conditions. The feed composition (30%/70%) chosen here for the simulations and the demonstration plant is aimed at the separation scenario of bulk CO_2 removing from the natural gas.

The CH_4 product purity is not specified to the strictest condition, 98 mol%, but to a slightly lower value, 95 mol%, to expand the range of application of the simulation. The packing density as well as the inter and intra-particle voidage of selected zeolites is retrieved from the earlier work of our research lab [51].

In this work, the Linear driving force (LDF) model was assumed for the kinetic model. The LDF mass transfer coefficient for both CH_4 and CO_2 used in the simulation are set to be a “large number”, because we assumed the diffusion of gases through adsorbents was sufficiently fast, so that the adsorption separation process is purely equilibrium governed separation. This does not mean that, in reality, the mass transfer rates are very high, but rather that we wanted to focus attention on the equilibrium isotherm properties of the adsorbents, not their mass transfer properties. It should be noted that all of the zeolites are large pore zeolites with negligible molecular sieving restrictions.

The pressure drop and superficial velocity of the gas phase through the bed is estimated by the Ergun equation (Equation 3.1), where μ is the viscosity of the bulk phase, d_p is the characteristic dimension of the adsorbents, ε_b is the voidage of the bed, ρ_b is the bulk density in kg/m^3 and v_0 is the bulk gas superficial velocity in m/s. At the flow rates used in these simulations, the pressure drop in the bed is a negligible fraction of the total pressure.

$$\frac{\partial P}{\partial z} = -\frac{150\mu(1-\varepsilon_b)^2}{\varepsilon_b^3 d_P^2} v_0 - \frac{1.75(1-\varepsilon_b)\rho_b}{\varepsilon_b^3 d_P} v_0^2 \qquad \textbf{Equation 3.1}$$

For the energy balance, the adsorption columns were considered to be at non-isothermal conditions. The wall of the adsorption column was assumed to be a thin wall such that there would be energy exchange between the adsorption column and the environment, where the environment temperature was set to be 313 K. This is to approach the real condition of an adsorption demonstration plant which we will discuss in a later section, whose adsorption column was covered by a heating jacket. The heat transfer coefficient between the gas phase and the column wall was set to be 50 W/(m^2K), which is the value of the heat transfer coefficient between the air and the stainless-steel plate.

3.3 Theoretical calculation

The gravimetric apparatus used for the high-pressure isotherm data collection and data treatment in this work requires greater user intervention than commercial volumetric adsorption apparatuses which are largely automated

within the software provided. In this section, we will, therefore, explain how we acquired the necessary information from the gravimetric adsorption isotherm measurement apparatus, and treated the data to obtain the excess and absolute adsorption isotherms of adsorbents at high pressure, as these are the key parameters for adsorption separation applications.

3.3.1 *In situ* gas density determination

The gravimetric adsorption isotherm measurement apparatus employed in this work has three positions which are illustrated in the schematic diagram in Figure 3.3.

In the first position (zero point, ZP), both the sinker and the sample container are settled and decoupled from the suspension balance. Only the permanent magnet and the coupling rod is lifted. When equilibrium is achieved with given pressure of fluid in the measurement cell, the reading from the balance is reset to zero for taring before each isotherm experiment.

In the second position (measuring position 1, $MP1$), the suspension magnet is lifted to a position in which the sample container is coupled. The equilibrium balance reading includes the mass of the sample container, sample, adsorbed molecules, as well as the buoyancy effects on them.

In the third position (measuring position 2, $MP2$), the suspension magnet rises to a higher position. In addition to the sample container, an alloy sinker with calibrated volume ($V_{sinker} = 4.2199\ cm^3$) and mass ($m_{sinker} = 19.02594\ \mathrm{g}$) is lifted and the weight recorded.

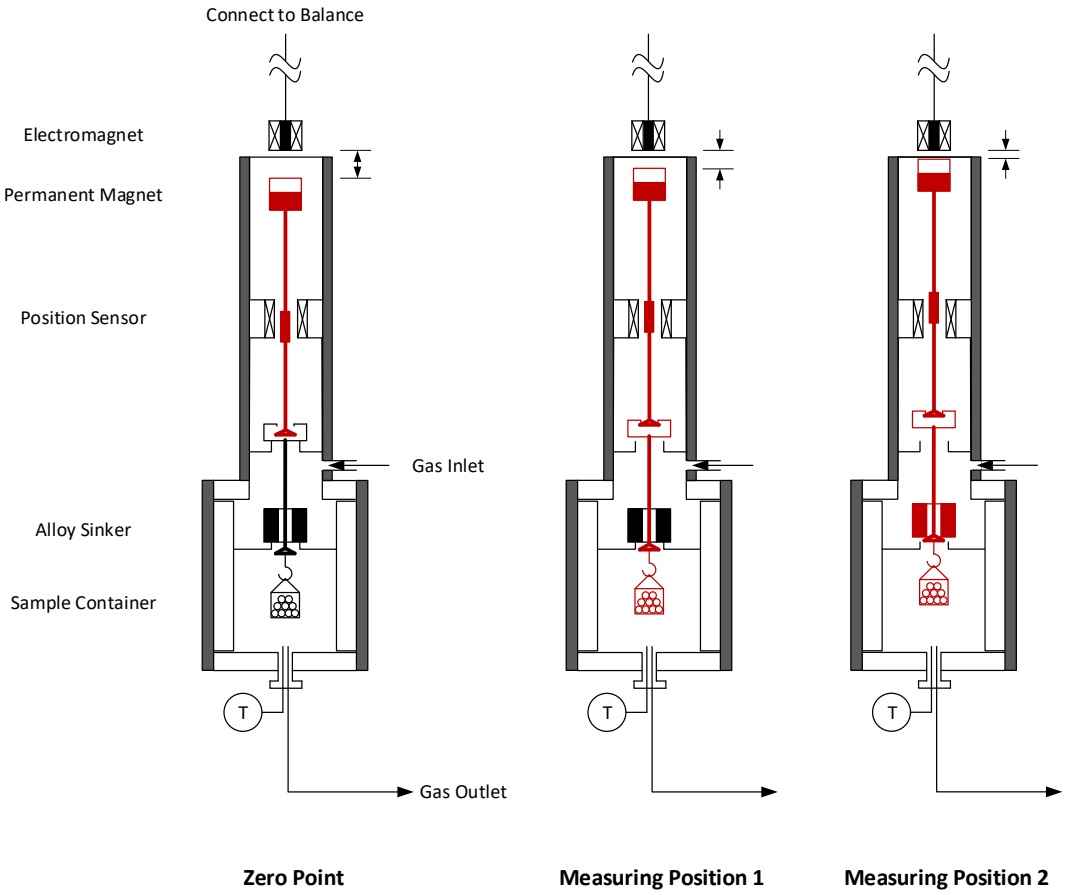

Figure 3.3. Schematic diagram showing the working mechanism of the three-position magnetic suspension balance.

The difference between the equilibrium reading at $MP2$ and $MP1$ gives the apparent mass reading of the alloy sinker under the measuring fluid atmosphere. Then with the calibrated mass and volume of the alloy sinker and the apparent mass, the density of the fluid (ρ_g) inside the measuring cell can be provided by Equation 2.1, which is required for the buoyancy correction of the measured sorption values. The density obtained by Aspen Properties (AspenTech, USA) using the fluid package GERG-2008 [87] for both CH_4 and CO_2 is illustrated in Figure 3.4 which demonstrates that the directly measured gas density matches well with that estimated by this equation of state.

$$\rho_g = \frac{m_{sinker} - (MP2 - MP1)}{V_{sinker}} \qquad \textbf{Equation 3.2}$$

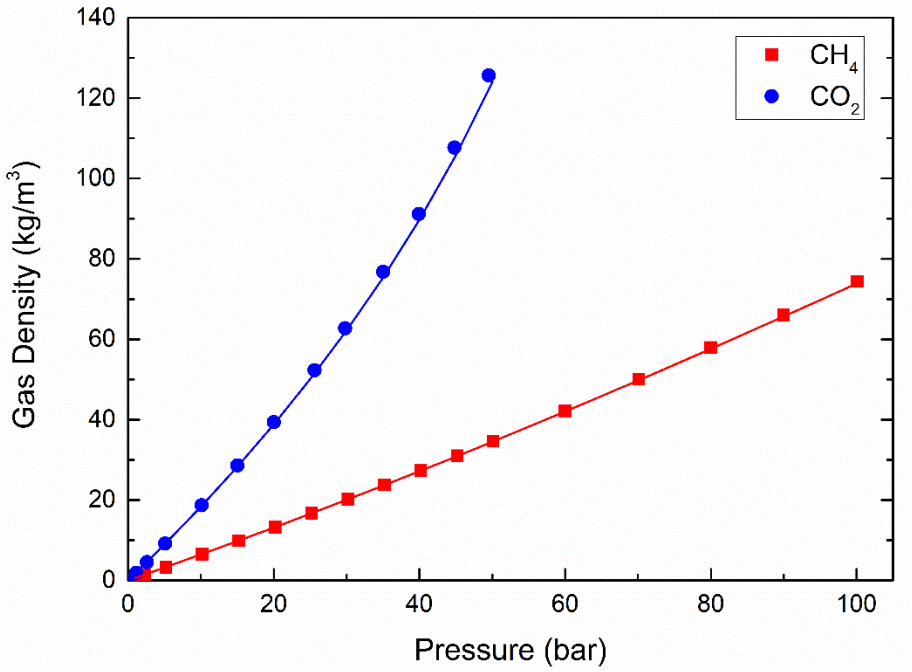

Figure 3.4. Comparison of gas densities at 303 K obtained by the fluid package and direct measurement using the three-positions magnetic suspension balance. (■), measurement density of CH_4; (●), measurement density of CO_2; solid line (–), gas density calculated by the GREG-2008 fluid package.

The direct measurement of the gas density can enhance the reliability of the sorption results. The earlier iterations of the gravimetric method employed equations of state (EoS) to define the density of the adsorptive fluid. It required precise temperature and pressure control, as well as an accurate EoS model. Any errors from either factor would induce significant deviations for the density and volume determination. When applying the three-position method to determine *in-situ* the fluid density, only the uncertainties of the balance are introduced. It is more important that the adsorption amount and the gas density measurement are in the same environment and determined with the same balance. Thus, the error can be reduced to a considerably lower level.

3.3.2 Adsorbent's buoyancy volume determination

The mechanism of the general gravimetric method involves measuring the mass uptake of the adsorbate on the adsorbent directly. However, as the adsorbent sample is always surrounded by the measuring fluid, the balance can only measure the difference between the weight and buoyancy force of the sample. Therefore, the volume of the sample is required to calculate the buoyancy effect. It needs to be determined before the adsorption measurement.

With a common assumption that helium does not adsorb on our materials, the volume required for buoyancy correction can be determined by introducing pure helium into the sample cell. As the pressure of the helium rises, the balance reading at $MP2$ provides the helium gas density (ρ_{He}) profile versus the gas pressure according to the aforementioned procedure (Equation 2.1). Meanwhile, the balance reading at $MP1$ provides the measured mass, namely apparent mass, of the adsorbent and the sample container under each pressure. Then, when fitting a linear regression to the apparent mass ($MP1$) as a function of helium density (ρ_{He}) according to Equation 3.3, the gradient of the resulting curve is the buoyancy volume (V_{buo}) of the adsorbent and its container. The intercept is then the summed mass of the adsorbent and the container weighed under vacuum (real mass).

$$MP1 = (m_{adsorbent} + m_{container}) - \rho_{He} V_{buo} \qquad \textbf{Equation 3.3}$$

Note that the real mass of the container ($m_{container}$) can be measured individually in advance, so the real mass of the adsorbent ($m_{adsorbent}$) is accessible. It will be used as the mass basis to calculate the specific gas uptake with the unit of [mmol/g] in further adsorption measurements.

The adsorbent's buoyancy volume obtained from Equation 3.3 is an overall volume of both the adsorbent skeleton and the sample container which is non-accessible for the measuring fluid. It is a function of the pressure of the surrounding fluid. The volume term would be used in the buoyancy correction for each data point at different pressures. Implicit in this is the assumption that the non-accessible volume would not alter due to thermal or pressure expansion. Also, the individual volume of either the adsorbent or the container is not required, because the buoyancy correction is always carried out in their entirety.

3.3.3 Excess and absolute adsorption equilibria

Upon the determination of the buoyancy volume and the real mass of the adsorbent using helium, the adsorption equilibrium isotherms of CH_4 and CO_2 were assessed by introducing the measuring fluid gradually to the sample cell. The balance readings were recorded at all three measuring positions following the procedure similar to the helium measurement. The adsorbed excess

amounts (n_{exc}) can be then calculated from the raw measurements following Equation 3.4. MW_g is the average molecular weight of the gas molecules. The adsorbed amount here is known as the Gibbs' excess adsorbed amount, or surface excess adsorbed amount as the volume of the adsorbed phase was not considered in the calculation.

$$n_{exc} = \frac{MP1 - (m_{adsorbent} + m_{container}) + \rho_g V_{buo}}{MW_g \cdot m_{adsorbent}} \qquad \textbf{Equation 3.4}$$

For most low pressure (≤10 bar) or high-temperature measurements, the volume of the adsorbed phase is negligible. The results calculated by Equation 3.4 could be directly presented as the absolute adsorbed amount. However, in a high-pressure adsorption experiment, when the volume of the adsorbed phase and the density of the measuring fluid become more important, the effect of the adsorbed phase is no longer insignificant. It contributes to a great extent in the buoyancy correction as the adsorbed phase volume acts as an increase to the buoyancy volume. More details regarding the excess and absoluted adsorbed amount in a high-pressure adsorption experiment can be referred to as the study of Myers et al. [88]

When taking the adsorbed phase volume (V_{ads}) into account, the absolute adsorbed amount (n_{abs}) can be calculated by Equation 3.5.

$$n_{abs} = n_{exc} + \frac{\rho_g V_{ads}}{MW_g \cdot m_{adsorbent}} \qquad \textbf{Equation 3.5}$$

All variables in Equation 3.5, except the volume of the absorbed phase, are known or determined by the aforementioned procedure. The volume of the adsorbed phase cannot be measured directly.

Currently, the selection of methods for the conversion from excess adsorption to absolute adsorption is still controversial. Many approximation methods to calculate either the volume or the density of the adsorbed phase have been reported. Thus, the published absolute results in one study may not be comparable with other literature. In this work, we assume the density of the adsorbed CO_2 to be equal to 0.773 g/cm^3, the liquid density of CO_2 at 293.15 K following the latest study from the National Institute of Standards and Technology

(NIST) [89]. The density of adsorbed CH_4 is assumed to be equal to 0.424 g/cm^3, the liquid density at the boiling point at ambient pressure [90]. Then, the volume of the adsorbed phase (V_{ads}) is approximated by the apparent adsorbed mass and the assumed density as shown in Equation 3.6. Substituting Equation 3.6 into Equation 3.5, we can calculate the absolute adsorbed amount.

$$V_{ads} = \frac{MP1 - (m_{adsorbent} + m_{container}) + \rho_g V_{buo}}{\rho_{ads} - \rho_g} \qquad \textbf{Equation 3.6}$$

3.4 Results and discussion

3.4.1 Material characterization

The six studied zeolites are typical crystalline Faujasite zeolites. To check their crystallinity, the diffraction patterns of one of the zeolites, CBV-780, were characterized and shown in Figure 3.5. There is good agreement between the simulated pattern of zeolite Y and experimentally measured patterns, as well as shows perfect matching with the CBV-780's XRD pattern measured in the literature[91]. The XRD pattern of the silica gel, Sorbead® WS, is also displayed in Figure 3.5. The one broad peak indicates its amorphous structure.

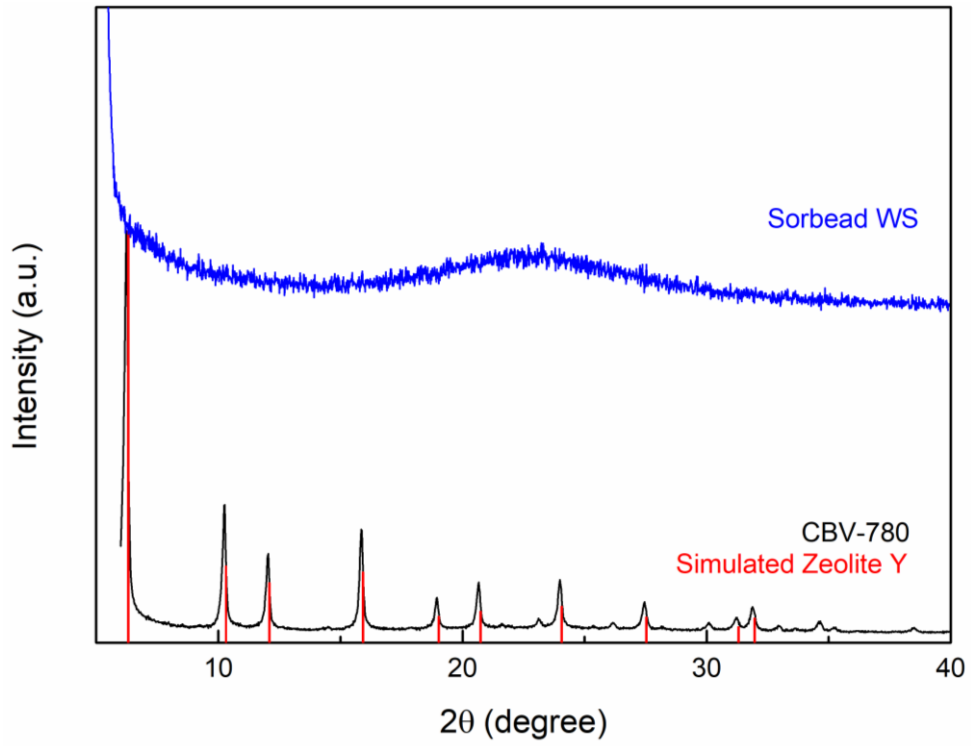

Figure 3.5. **XRD pattern of CBV-780 (black), Sorbead® WS (blue), and simulated XRD pattern of Zeolite Y (red)**

The nitrogen physisorption isotherm at 77.3 K of six selected zeolites are presented in Figure 3.6. According to the latest IUPAC adsorption isotherm classifications in 2015 [17], the observed isotherms are a composite of type I(a) isotherms at low coverage range and type IV isotherms with H4 type hysteresis loops at high coverage, although the hysteresis loops in the isotherms of HSZ-320HOA and HSZ-350HUA are hardly visible.

The pronounced uptake at low P/P^o is associated with the microporous structure originated from the framework of zeolite. Their micropore sizes calculated by the Horvath-Kawazoe (H-K) method were in the range of 6 to 10 Å. The volume of micropores in the material with a pore size width from 3 to 17 Å are shown in Table 3.2, computed by the H-K method as well.

The hysteresis loop in N_2 isotherms at P/P^o greater than 0.4 indicates the presence of mesoporous structures which could be formed during the dealumination process. The Na_2O weight percent and SiO_2/Al_2O_3 ratio in Table 3.2 were provided by the manufacturers. Both are indicators of the level of the dealumination process. As the level of dealumination increases, the sodium cations in the zeolite framework will be extracted simultaneously with the aluminium species. In the meantime, the recrystallization of the zeolite occurs concurrently with dealumination to “heal” the aluminium vacancies creating new pores within the crystals, which are mostly mesopores [92,93]. Moreover, the fact that the adsorption isotherms do not reveal a truly “horizontal” plateau at relative pressures higher than 0.1 also gives a clue to the existence of mesoporosity. The observed slope in the region from 0.4 to 0.9 is associated with the filling of mesopores. The mesoporous volumes in Table 3.2 were obtained from the Barrett–Joyner–Halenda (BJH) theory at a pore width from 17 to 2,000 Å.

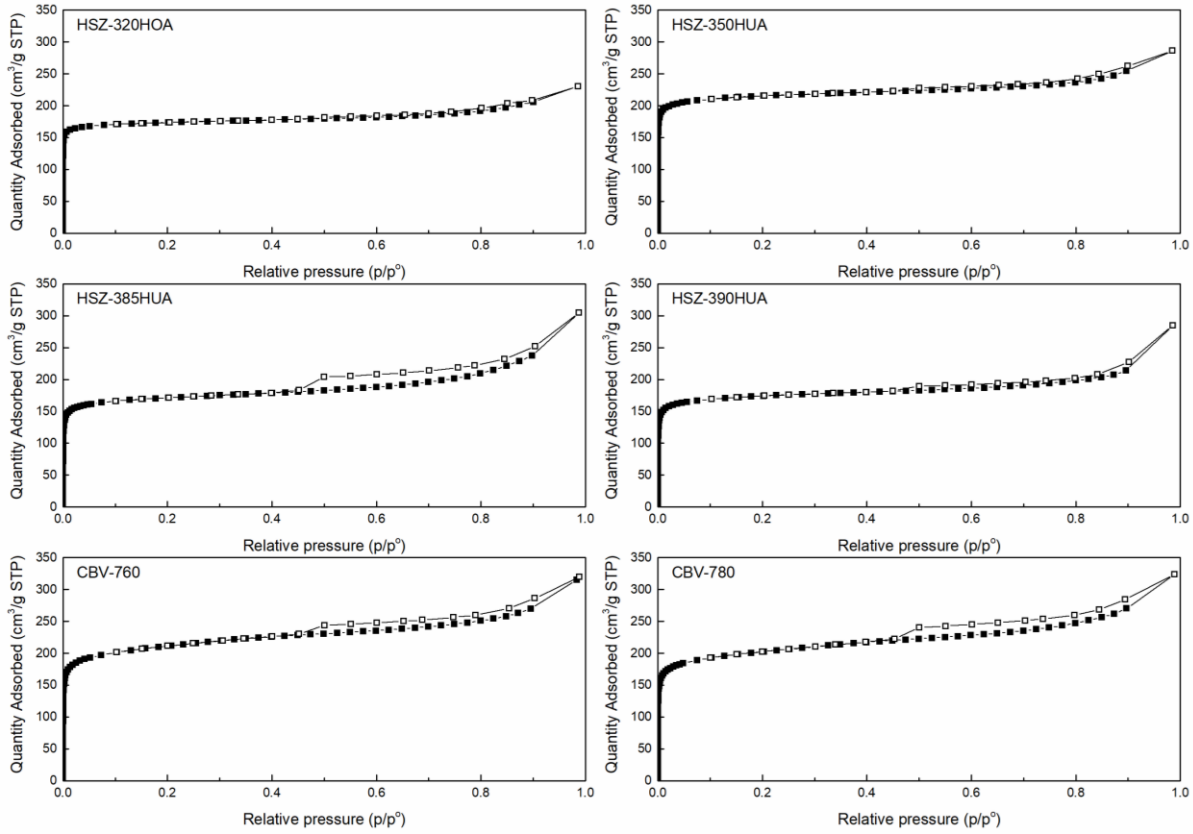

Figure 3.6. **Nitrogen isotherms at 77.3 K on six selected zeolites. (–■–), adsorption curves; (–□–), desorption curves.**

The Brunauer-Emmett-Teller (B.E.T.) surface areas in Table 3.2 were obtained from the linear zone of the B.E.T. plot. However, the B.E.T. theory is in a strict sense not applicable to microporous materials such as Faujasite zeolites, because the several assumptions for B.E.T. theory are not applicable for microporous materials: adsorption taking place in the microporous materials is basically via filling the pores and not necessary on the potential adsorption sites; in addition, the thickness of the adsorption layer is strictly sterically limited by the pore size. Therefore, although there are mesopores in the material, the B.E.T. surface area results reported here still only lead to an apparent surface area but not the actual probe accessible surface area.

The textural properties of all adsorbents are in good agreement with the data provided by the manufactures. However, the B.E.T. surface area and the total pore volume for zeolite, HSZ-390HUA, in this work are about 15% lower compared to the reported values [94].

Table 3.2. **Textural properties of selected zeolites calculated by nitrogen adsorption isotherms at 77.3 K**

	Na_2O (wt%)	*SiO_2/Al_2O_3 ratio*	*Microporous volume (cm^3/g)*	*Mesoporous volume (cm^3/g)*	*B.E.T. surface area (m^2/g)*
HSZ-320HOA	4	5.5	0.268	0.109	540
HSZ-350HUA	0.1	10	0.332	0.123	673
HSZ-385HUA	0.1	100	0.264	0.246	616
HSZ-390HUA	0.05	500	0.268	0.205	630
CBV-760	0.03	60	0.322	0.231	676
CBV-780	0.03	80	0.311	0.253	637

The textural properties of Sorbead® WS is provided by the vendor, which is listed in Table 3.3.

Table 3.3. **Textural properties of Sorbead® WS**

Properties	*Value*	
Chemical composition	SiO_2	97 wt.%
	Al_2O_3	3 wt.%
B.E.T. surface area (m^2/g)	650	
Pore volume (cm^3/g)	0.45	

3.4.2 Intermediate-pressure CH_4 and CO_2 adsorption isotherms

Intermediate-pressure adsorption isotherms from 0 to 10 bar for CH_4 and CO_2 on all studied adsorbents were measured at 303 K, 313 K and 333 K. The results are shown in Figure 3.7 to Figure 3.13.

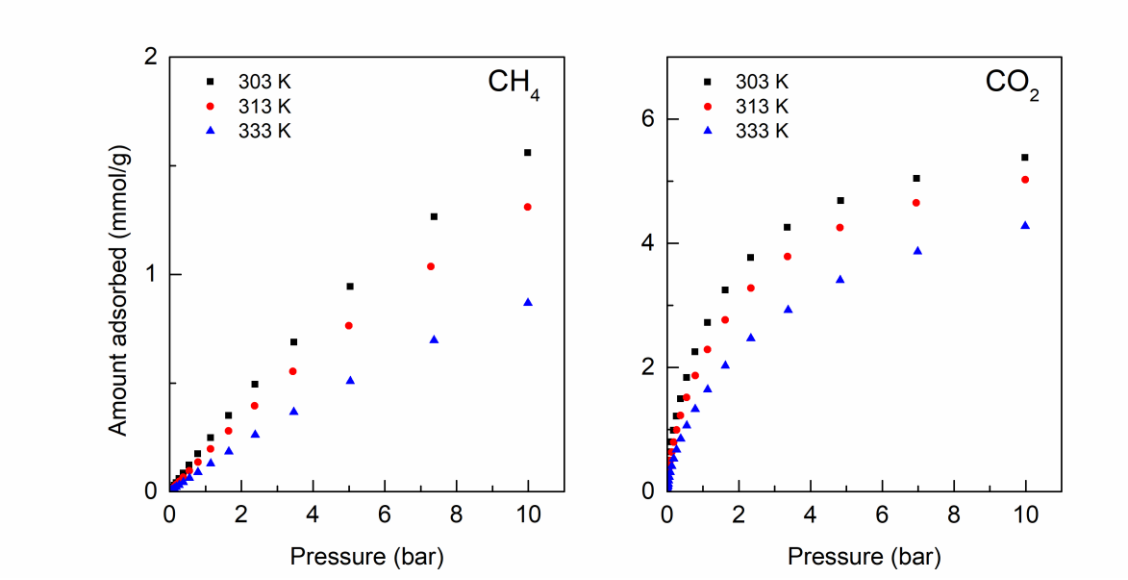

Figure 3.7. Intermediate pressure adsorption isotherms for CH_4 and CO_2 on HSZ-320HOA.

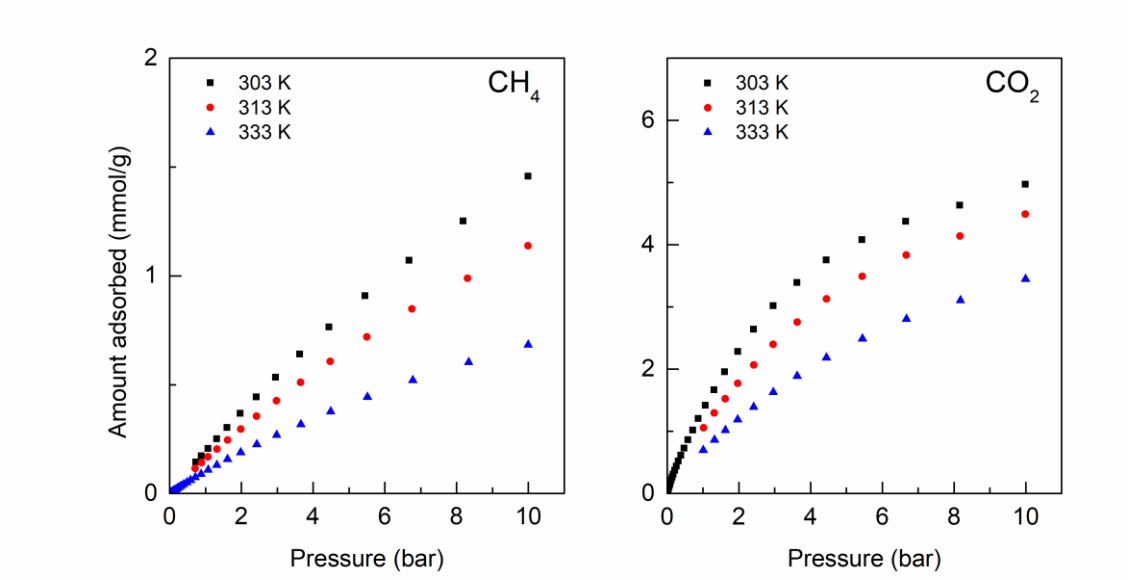

Figure 3.8. Intermediate pressure adsorption isotherms for CH_4 and CO_2 on HSZ-350HUA.

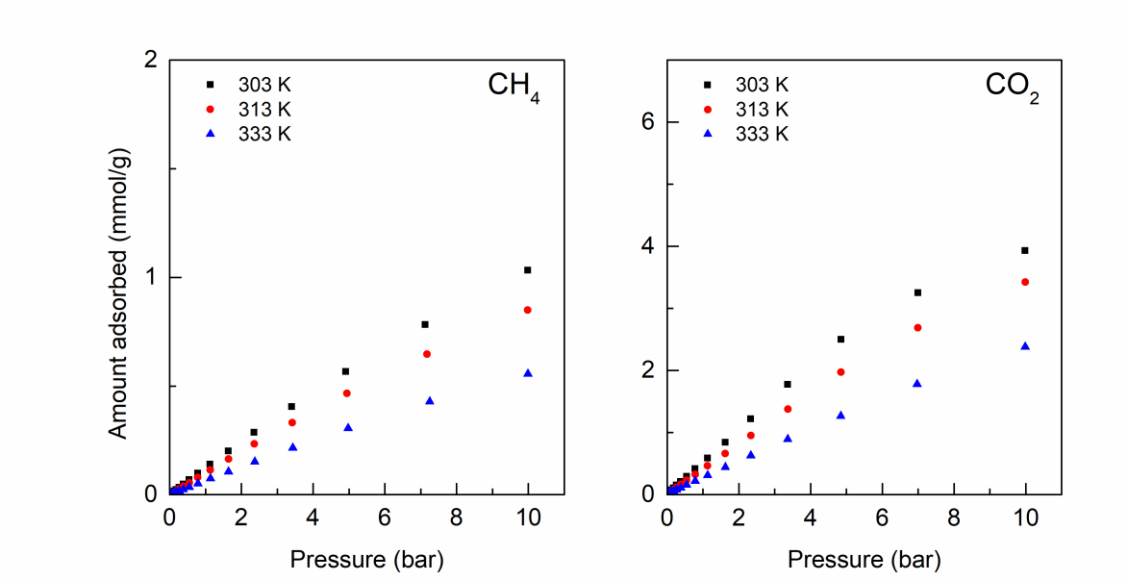

Figure 3.9. Intermediate pressure adsorption isotherms for CH_4 and CO_2 on HSZ-385HUA.

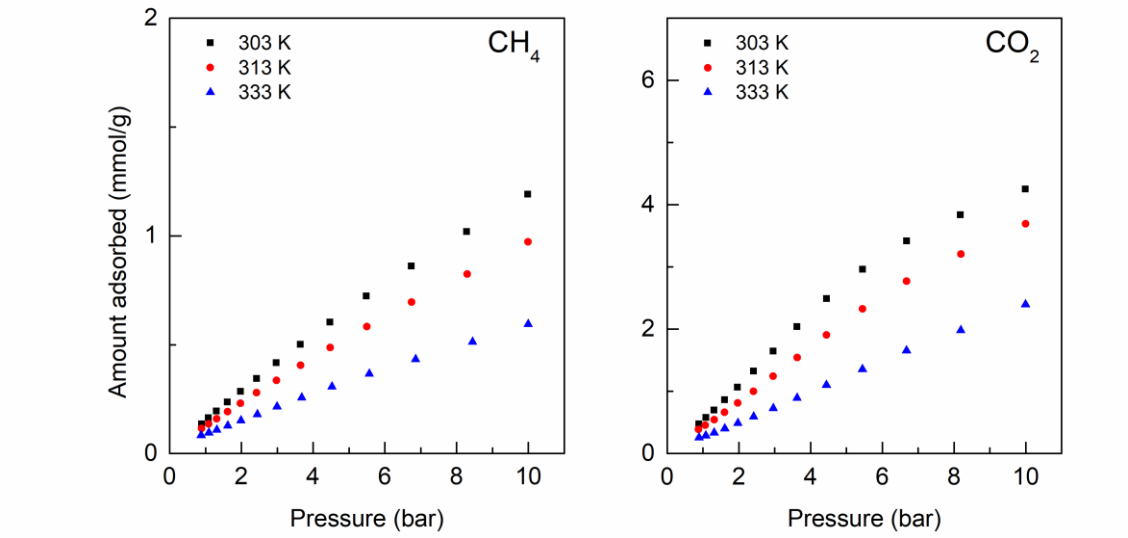

Figure 3.10. Intermediate pressure adsorption isotherms for CH_4 and CO_2 on HSZ-390HUA.

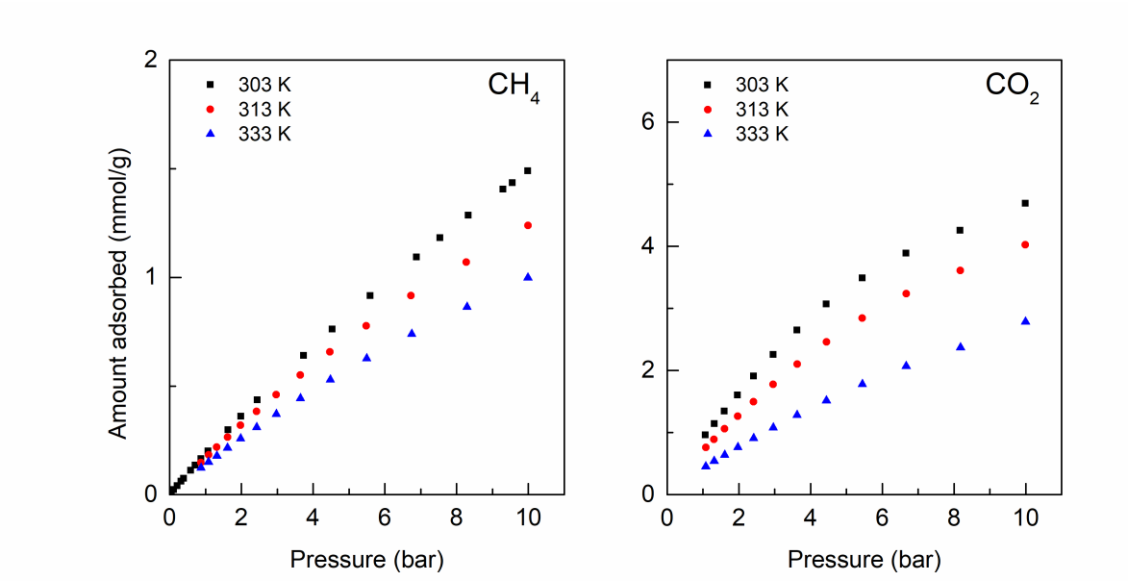

Figure 3.11. Intermediate pressure adsorption isotherms for CH_4 and CO_2 on CBV-760.

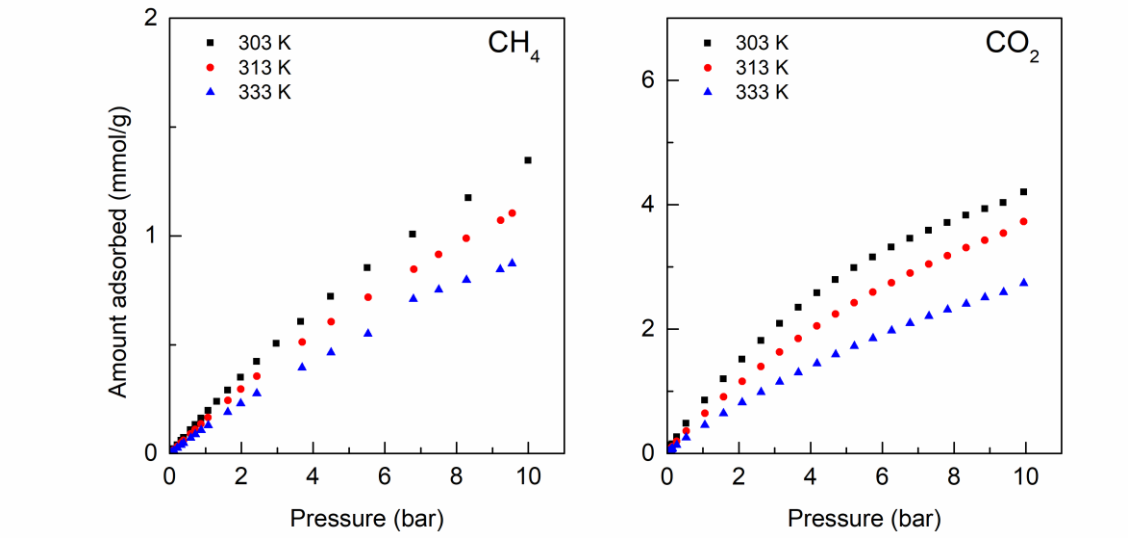

Figure 3.12. Intermediate pressure adsorption isotherms for CH_4 and CO_2 on CBV-780.

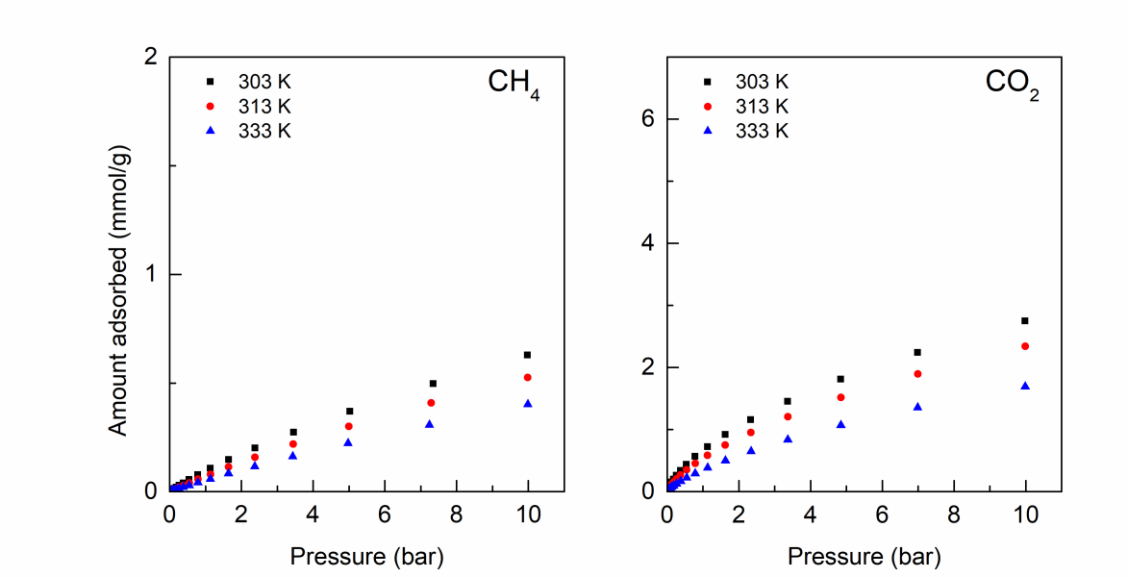

Figure 3.13. Intermediate pressure adsorption isotherms for CH_4 and CO_2 on Sorbead® WS.

As can be seen in the graphs, the adsorption isotherms for CH_4 on all studied adsorbents are approximately linear, while the linearity of the CO_2 adsorption isotherms decreases as the Si/Al ratio increases. This reflects the difference of the affinity between CH_4-solid and CO_2-solid. CO_2 molecules have a large quadrupole moment ($-13.71 \times 10^{-40}\ cm^2$) relative to CH_4 molecule ($0\ cm^2$) which can interact with the charged solid surface. The interaction becomes stronger when the solid surface is charged, like at the place in zeolites where the $[AlO_4]^-$ tetrahedra is negatively charged and balanced by a cation. Zeolites with low Si/Al ratio means more $[AlO_4]^-$ tetrahedra units present in the zeolitic framework, which can enhance the interaction between CO_2 and the solid surface, especially at low coverage. As the Si/Al ratio increases, this enhancement effect is reduced due to the decreasing presence of $[AlO_4]^-$ sites, and the adsorption isotherms of CO_2 become more linear. The CH_4 molecule is perfectly spatially symmetric and has no dipole nor quadrupole moment. The interaction between CH_4 and the solid surface is mainly attributed to the van der Waals force, which is proportional to the exposure rate of the adsorptive sites to the CH_4 molecules, namely the partial pressure of CH_4. Thus, the adsorption isotherms of CH_4 is almost linear in all studied zeolites.

The adsorption amounts of both CO_2 and CH_4 on Sorbead® WS in Figure 3.13 are lower than those on studied zeolites. In addition, the isotherms are more linear than zeolites, which indicates weaker interactions between the gas

molecules and the solid surface.

3.4.3 Isosteric heat of adsorption

Using the low and intermediate pressure adsorption isotherms, the isosteric heats of adsorption were calculated. They were determined based on the Clausius-Clapeyron equation (Equation 3.7, [95]). The isotherm data of one adsorbent were firstly interpolated to create a van't Hoff plot as $ln(P)$ *vs* $1/T$ for any given equilibrium loading, namely generating an isostere. The isostere data were then loaded into MATLAB and linear fitted to obtain the slope, the intercept, and the corresponding fitting errors by a MATLAB function *"polyfit"*. The obtained slope at each equilibrium loading was then the isosteric heat of adsorption for the certain loading.

$$\Delta H_{st} = R\left[\frac{\partial(lnP)}{\partial\left(\frac{1}{T}\right)}\right]_n \qquad \textbf{Equation 3.7}$$

The results, isosteric heat of adsorption of CH_4 and CO_2 on all studied adsorbents are shown in Figure 3.14. The error bars represent the 95 % confidence interval of the result based on their linear regressions. The margin of error is calculated using Equation 3.8, where SE is the standard error determined directly by the MATLAB function *"polyfit"*, $t_{DF,CL=95\%}$ is the value from the t distribution for 95% confidence for the specified number of degree of freedom (DF) for the fitting, and the degree of the freedom is the number of data points minus the number of parameters fit by the linear regression. Figure 3.14 demonstrates that for the calculation of isosteric heat of adsorption, HSZ-320HOA has relatively small errors while CBV-780 has large errors.

$$MoE = SE \times t_{DF,CL=95\%} \qquad \textbf{Equation 3.8}$$

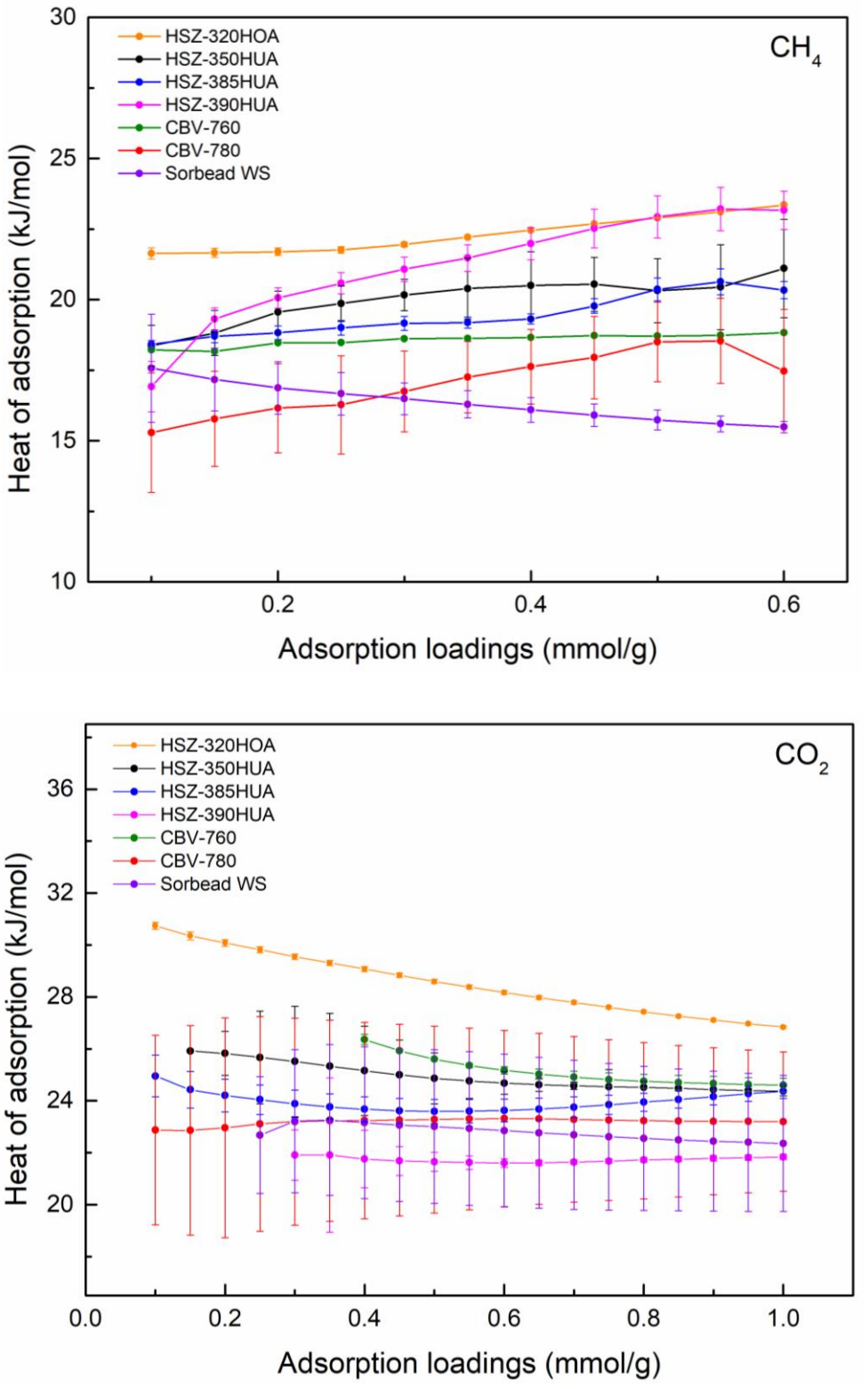

Figure 3.14. **Isosteric heat of adsorption for CH_4 and CO_2 on studied adsorbents.**

Here the graphs show the isosteric heat of adsorption for CH_4 at a loading between 0.1 to 0.6 mmol/g, and for CO_2 at a loading between 0.1 to 1.0 mmol/g. Regardless of the errors, the heat of adsorption for CH_4 is in a range between 16

kJ/mol to 23 kJ/mol, obviously lower than that for CO_2 which are in a range between 22 kJ/mol to 31 kJ/mol. This phenomenon again suggests that the CO_2-solid interaction is stronger than the CH_4-solid interaction at low coverage, as expected.

3.4.4 High-pressure CH_4 and CO_2 adsorption equilibria

High-pressure adsorption isotherms are more important and relevant to the purpose of this study. As explained in the previous section, the high-pressure adsorption isotherms directly measured by the gravimetric method is the excess adsorption isotherms, while the actual adsorption amounts are the absolute adsorption isotherms. The absolute one can only be obtained under certain assumptions and calculated according to the excess adsorption isotherms, as shown previously. The difference between the absolute and the excess adsorption isotherms are illustrated in Figure 3.15.

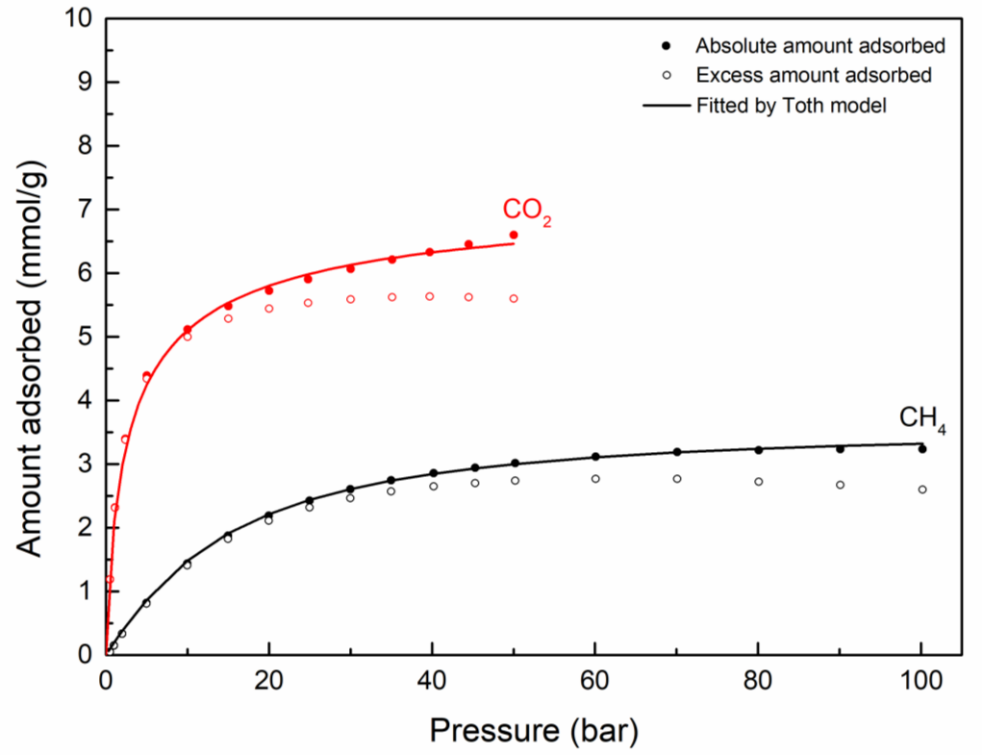

Figure 3.15. A demonstration of the difference between absolute amount adsorbed and excess amount adsorbed on the adsorbents. The graph is plotted using adsorption isotherm data at 313 K on HSZ-320HOA.

The absolute adsorption isotherms of CH_4 and CO_2 on each of the studied materials at three different temperatures are shown in Figure 3.16 to Figure 3.22. The absolute adsorbed isotherms were fitted to both the Toth model (Equation

2.6) and Langmuir model (Equation 2.3) by MATLAB 2019a (The Mathworks, Inc). The residual sum of squares (RSS) was used to show the fitting error following Equation 3.9.

$$\mathrm{RSS} = \sum_{T}\sum_{P}\left(n_{fitting} - n_{\exp data}\right)^2 \qquad \textbf{Equation 3.9}$$

The solid circles in different colours represent the experimental data points. To demonstrate the consistency between intermediate-pressure adsorption isotherms and high-pressure adsorption isotherms, isotherms data of CO_2 and CH_4 on HSZ-320HOA measured by the ASAP 2050 were also shown in Figure 3.16 as symbols of open triangles. As can be seen, CO_2 adsorption isotherms at the low-pressure regime obtained by two different measurement methods are matching better than those of CH_4 adsorption isotherms. One possible reason for this is because the amount of CO_2 adsorbed on the solid is always more than that of CH_4. If the absolute deviation of the amount adsorbed between these two methods is similar, the relative difference between two measurement methods of the strongly adsorbed component, namely CO_2, is then smaller.

The solid lines in the figures are the fits using the Toth model, while the dash lines are the fits by the Langmuir model. All the isotherms were completely reversible. Throughout the range of examined pressures and temperatures, CO_2 adsorbed more strongly than CH_4.

It is seen that the Toth model fits the CH_4 and CO_2 absolute adsorption isotherms better than those fitted by the Langmuir model. However, the fitted lines deviate slightly in the high-pressure regimes. Considering the deviations become significant at high pressure, they could be attributed to the assumption used for the calculation of the absolute amount adsorbed, where we assumed a fixed adsorbed phase density.

For each material, a table is provided (Table 3.4 to Table 3.10) to summarize the fitting parameters of both the Toth model and Langmuir model, along with the standard errors for each parameter of the fitting. Although the Toth model includes an empirical parameter, the heterogeneity number t, it has very good flexibility to fit the experimental data. The goodness of fitting is displayed in terms

of the residues sum of squares (RSS). The trend of RSS again indicates better fittings of the Toth model than that of the Langmuir model.

The shapes of isotherms for CO_2 and CH_4 of these high silica zeolites are relatively similar, however, their adsorption capacities are different. The adsorption capacity of CO_2 is more than twice that of CH_4, and therefore these adsorbents can be exploited for the separation of CO_2 from CO_2/CH_4 gas mixture.

Sorbead® WS, unlike the zeolitic counterparts, has very linear adsorption isotherms for both CO_2 and CH_4. Linear CO_2 isotherms were the undesired type of isotherms in low-pressure adsorption applications because they normally imply low CO_2 adsorption amounts, and subsequently low selectivity. In high-pressure applications, however, the issue of low adsorption amount for linear isotherms can be compensated by the high pressure since CO_2 adsorption amount rises linearly with the pressure. On the contrary, the adsorption amounts of CO_2 in non-linear isotherms are limited by the saturated capacity achieved at a lower pressure due to a much stronger interaction. This means that the adsorbents with linear isotherms could outperform the adsorbent with non-linear isotherms at certain high pressures when they have similar CH_4 isotherms.

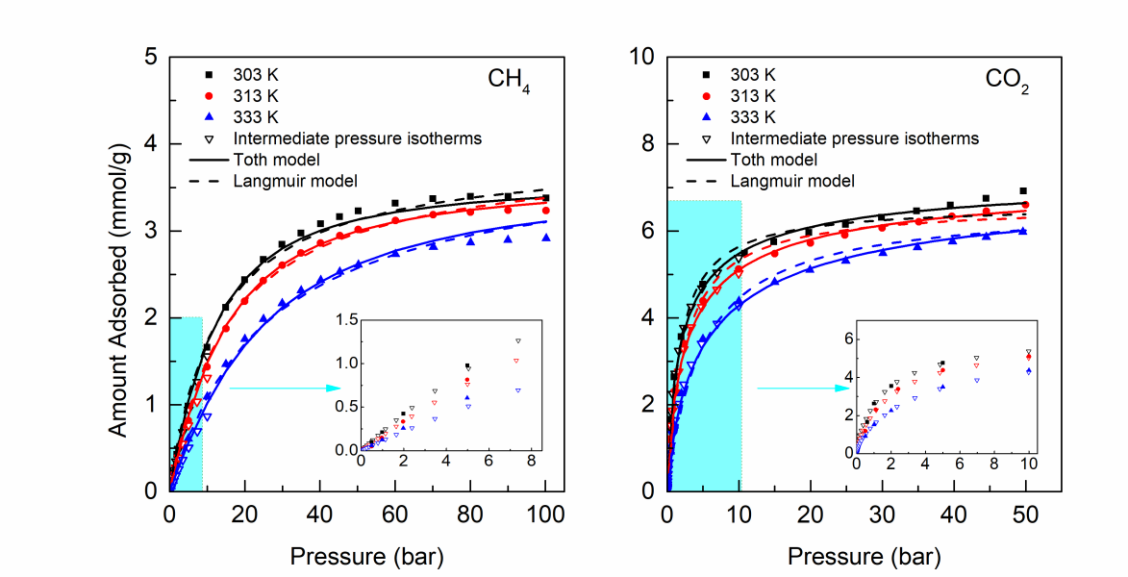

Figure 3.16. High pressure absolute adsorption isotherms of CH4 and CO2 on HSZ-320HOA. Isotherms are fitted to the Toth model shown in a solid line and Langmuir model in a dashed line. The intermediate pressure isotherms measured by the ASAP 2050 instrument are also shown in Figure as the symbol of open triangle.

Table 3.4. High-pressure isotherm fitting parameters of HSZ-320HOA by Toth and Langmuir model.

Model	*Gas*	$n_i^* \ (mol \cdot kg^{-1})$	$b_i \times 10^5 \ (bar^{-1})$	$Q_i \ (kJ \cdot mol^{-1})$	t_i	*RSS*
Toth	CH_4	3.59 ± 0.05	1.96 ± 0.60	20.67 ± 0.80	1.30 ± 0.07	0.204
	CO_2	7.41 ± 0.19	1.63 ± 1.15	27.55 ± 1.75	0.67 ± 0.04	0.872
Langmuir	CH_4	3.91 ± 0.04	2.18 ± 0.78	20.77 ± 0.95	N/A	0.298
	CO_2	6.60 ± 0.06	4.99 ± 1.45	29.45 ± 2.38	N/A	1.825

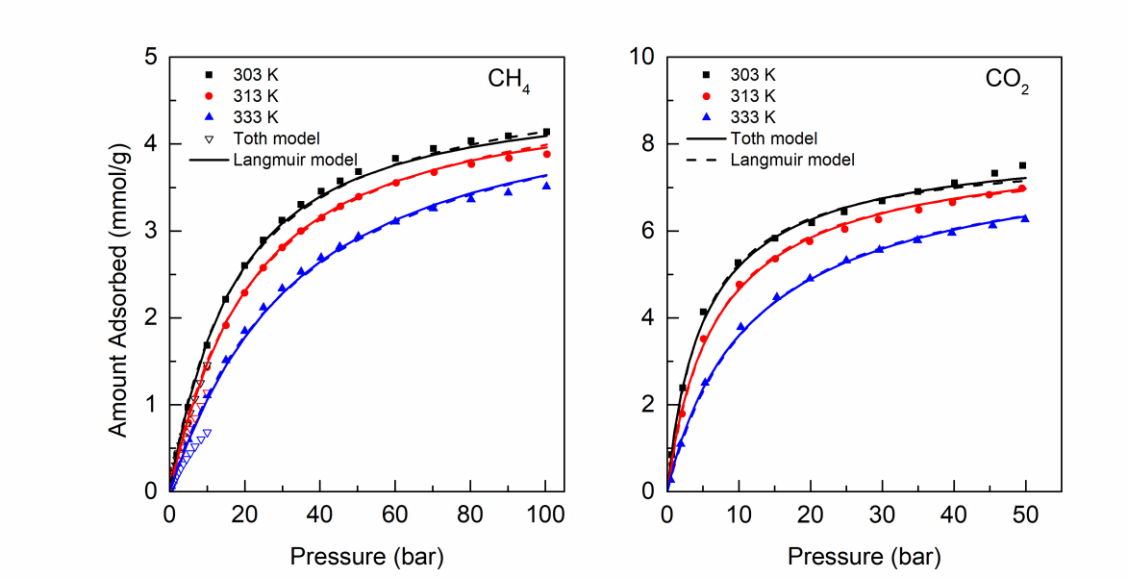

Figure 3.17. High-pressure absolute adsorption isotherms of CH_4 and CO_2 on HSZ-350HUA. Isotherms are fitted to the Toth model shown in a solid line and Langmuir model in a dashed line.

Table 3.5. High-pressure isotherm fitting parameters of HSZ-350HUA by Toth and Langmuir model.

Model	*Gas*	$n_i^* \, (mol \cdot kg^{-1})$	$b_i \times 10^5 \, (bar^{-1})$	$Q_i \, (kJ \cdot mol^{-1})$	t_i	*RSS*
Toth	CH_4	4.60 ± 0.07	3.33 ± 0.62	18.63 ± 0.49	1.16 ± 0.05	0.126
	CO_2	8.18 ± 0.19	1.33 ± 0.51	24.47 ± 0.98	0.90 ± 0.05	0.459
Langmuir	CH_4	4.88 ± 0.03	3.54 ± 0.71	18.63 ± 0.54	N/A	0.156
	CO_2	7.87 ± 0.06	1.06 ± 0.39	24.85 ± 0.97	N/A	0.509

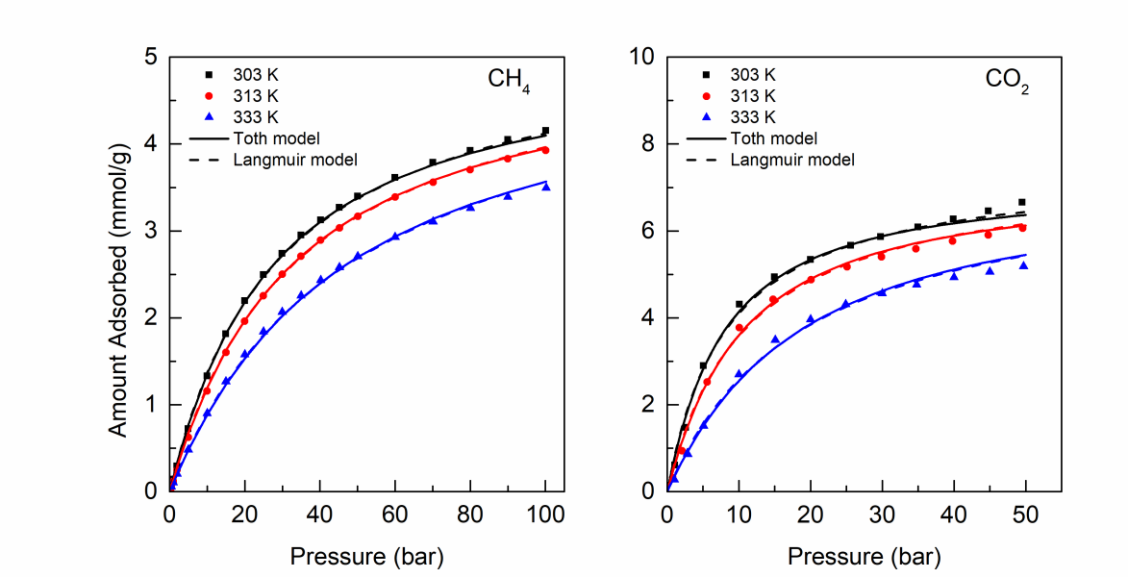

Figure 3.18. High-pressure absolute adsorption isotherms of CH_4 and CO_2 on HSZ-385HUA. Isotherms are fitted to the Toth model shown in a solid line and Langmuir model in a dashed line.

Table 3.6. High-pressure isotherm fitting parameters of HSZ-385HUA by Toth and Langmuir model.

Model	*Gas*	$n_i^* \, (mol \cdot kg^{-1})$	$b_i \times 10^5 \, (bar^{-1})$	$Q_i \, (kJ \cdot mol^{-1})$	t_i	*RSS*
Toth	CH_4	5.07 ± 0.08	6.51 ± 0.66	15.94 ± 0.27	1.08 ± 0.03	0.044
	CO_2	7.13 ± 0.23	0.66 ± 0.30	24.72 ± 1.16	1.13 ± 0.10	0.680
Langmuir	CH_4	5.30 ± 0.03	6.66 ± 0.70	15.91 ± 0.28	N/A	0.050
	CO_2	7.51 ± 0.10	0.75 ± 0.32	24.53 ± 1.13	N/A	0.728

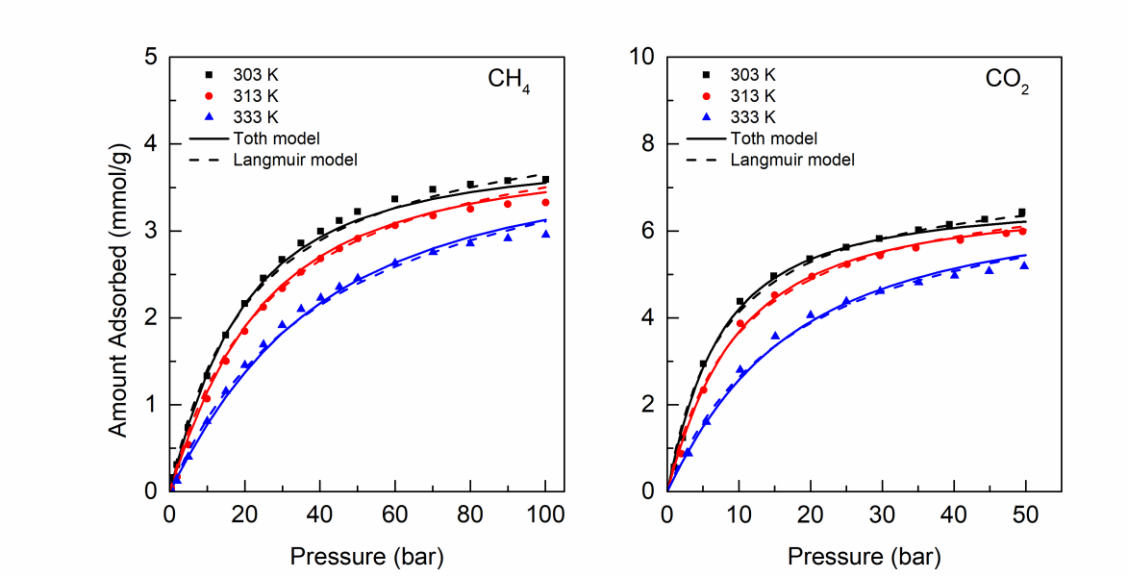

Figure 3.19. High-pressure absolute adsorption isotherms of CH_4 and CO_2 on HSZ-390HUA. Isotherms are fitted to the Toth model shown in a solid line and Langmuir model in a dashed line.

Table 3.7. High-pressure isotherm fitting parameters of HSZ-390HUA by Toth and Langmuir model.

Model	*Gas*	$n_i^* \, (mol \cdot kg^{-1})$	$b_i \times 10^5 \, (bar^{-1})$	$Q_i \, (kJ \cdot mol^{-1})$	t_i	*RSS*
Toth	CH_4	3.91 ± 0.09	1.25 ± 0.38	20.64 ± 0.79	1.36 ± 0.09	0.235
	CO_2	6.72 ± 0.17	0.55 ± 0.26	25.28 ± 1.21	1.28 ± 0.11	0.612
Langmuir	CH_4	4.44 ± 0.06	1.31 ± 0.46	20.77 ± 0.93	N/A	0.331
	CO_2	7.34 ± 0.10	0.71 ± 0.35	24.88 ± 1.31	N/A	0.798

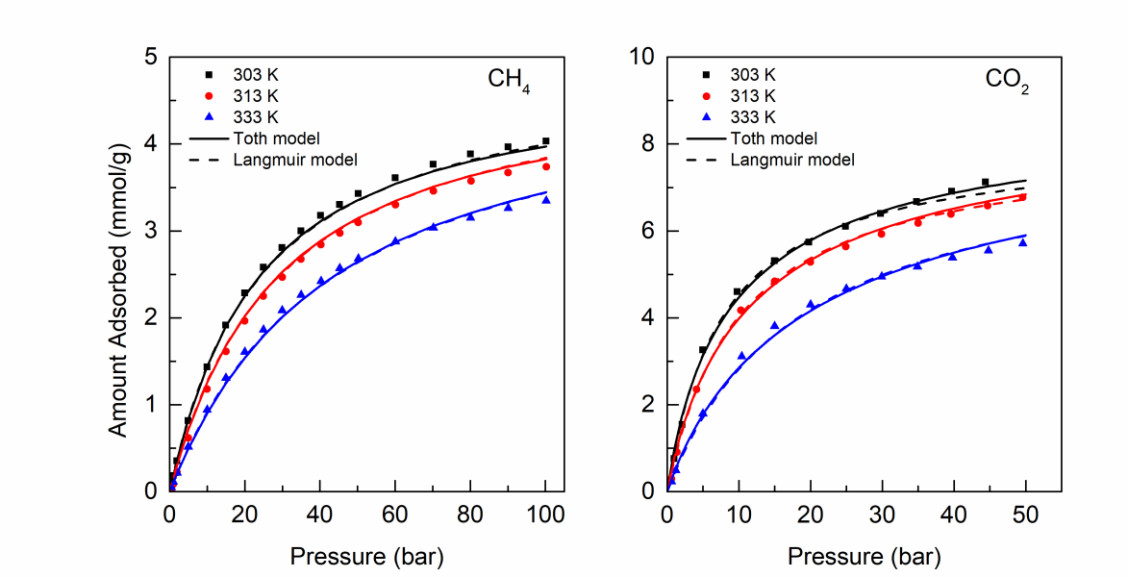

Figure 3.20. High-pressure absolute adsorption isotherms of CH_4 and CO_2 on CBV-760. Isotherms are fitted to the Toth model shown in a solid line and Langmuir model in a dashed line.

Table 3.8. High-pressure isotherm fitting parameters of CBV-760 by Toth and Langmuir model.

Model	*Gas*	$n_i^* \, (mol \cdot kg^{-1})$	$b_i \times 10^5 \, (bar^{-1})$	$Q_i \, (kJ \cdot mol^{-1})$	t_i	*RSS*
Toth	CH_4	4.78 ± 0.13	3.88 ± 0.83	17.94 ± 0.56	1.07 ± 0.06	0.170
	CO_2	8.94 ± 0.40	0.78 ± 0.32	24.66 ± 1.05	0.84 ± 0.07	0.639
Langmuir	CH_4	4.96 ± 0.04	3.93 ± 0.84	17.65 ± 0.56	N/A	0.175
	CO_2	8.08 ± 0.08	0.63 ± 0.20	25.12 ± 0.87	N/A	0.461

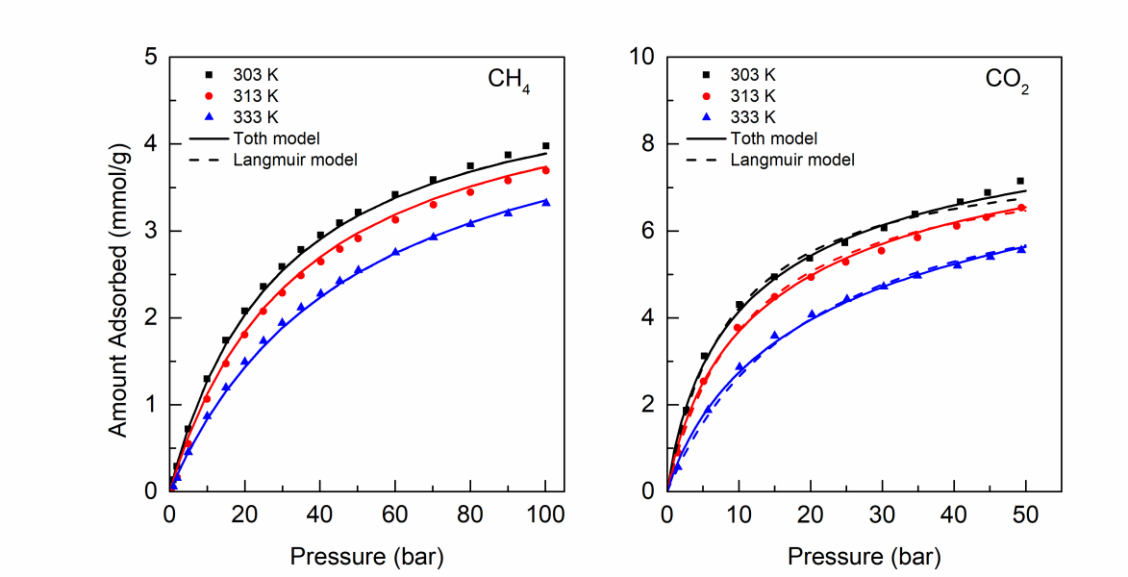

Figure 3.21. High-pressure absolute adsorption isotherms of CH_4 and CO_2 on CBV-780. Isotherms are fitted to the Toth model shown in a solid line and Langmuir model in a dashed line.

Table 3.9. High-pressure isotherm fitting parameters of CBV-780 by Toth and Langmuir model.

Model	*Gas*	$n_i^* \, (mol \cdot kg^{-1})$	$b_i \times 10^5 \, (bar^{-1})$	$Q_i \, (kJ \cdot mol^{-1})$	t_i	*RSS*
Toth	CH_4	5.02 ± 0.17	6.14 ± 1.18	16.04 ± 0.51	1.01 ± 0.06	0.134
	CO_2	9.56 ± 0.54	1.17 ± 0.39	23.73 ± 0.86	0.71 ± 0.06	0.355
Langmuir	CH_4	5.04 ± 0.05	6.12 ± 1.15	16.05 ± 0.50	N/A	0.134
	CO_2	7.94 ± 0.10	0.76 ± 0.30	24.41 ± 1.06	N/A	0.600

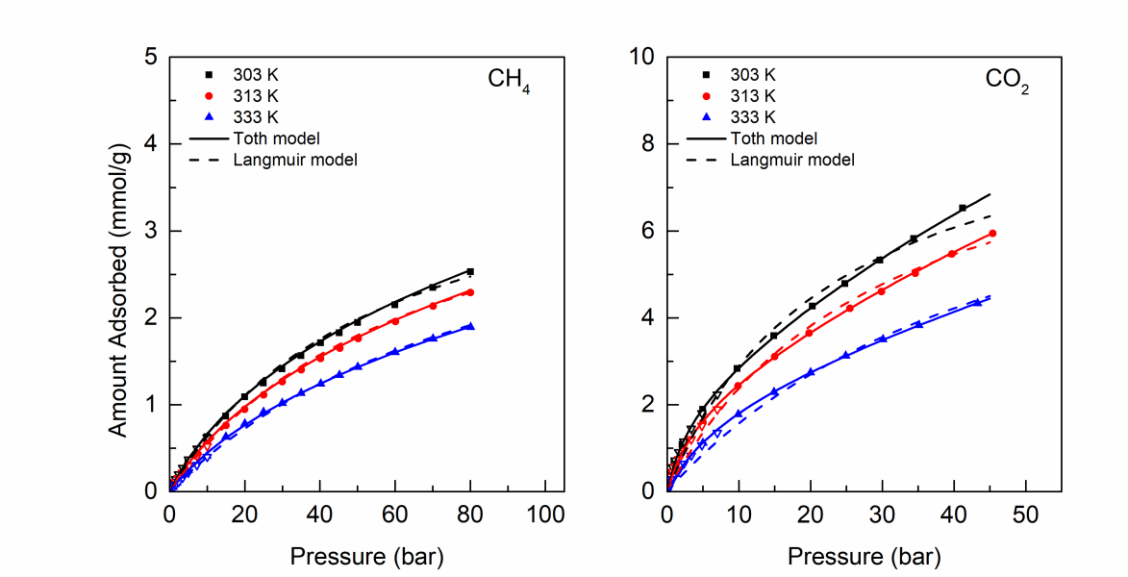

Figure 3.22. High-pressure absolute adsorption isotherms of CH_4 and CO_2 on Sorbead® WS. Isotherms are fitted to the Toth model shown in a solid line and Langmuir model in a dashed line.

Table 3.10. High-pressure isotherm fitting parameters of Sorbead® WS by Toth and Langmuir model.

Model	*Gas*	$n_i^* \ (mol \cdot kg^{-1})$	$b_i \times 10^5 \ (bar^{-1})$	$Q_i \ (kJ \cdot mol^{-1})$	t_i	*RSS*
Toth	CH_4	9.72 ± 0.68	3.68 ± 0.19	14.50 ± 0.12	0.53 ± 0.02	0.004
	CO_2	10.02 ± 0.01	6.84 ± 0.31	22.26 ± 1.23	0.89 ± 0.04	0.775
Langmuir	CH_4	4.21 ± 0.07	5.25 ± 0.68	14.71 ± 0.35	N/A	0.034
	CO_2	9.61 ± 0.40	0.77 ± 0.36	21.76 ± 1.29	N/A	0.884

The adsorption isotherm data of CH_4 and CO_2 for all studied adsorbents are available in the Appendix. Due to the controversial methods of calculating the absolute adsorption, the excess adsorption loadings, together with the absolute adsorption loadings, at each measuring condition are provided.

The ideal selectivity of CO_2 relative to CH_4 at 313 K for all examined zeolites are shown in Figure 3.23. The definition of ideal selectivity is described in Equation 2.13. In this case, the mixture component adsorption amounts with a composition of 30% CO_2/70% CH_4 were calculated according to the IAST method (hence it is called IAST selectivity). The basic concept of IAST is introduced in Section 2.1.2.4. Toth model fitting parameters of adsorbents were used in the IAST calculation.

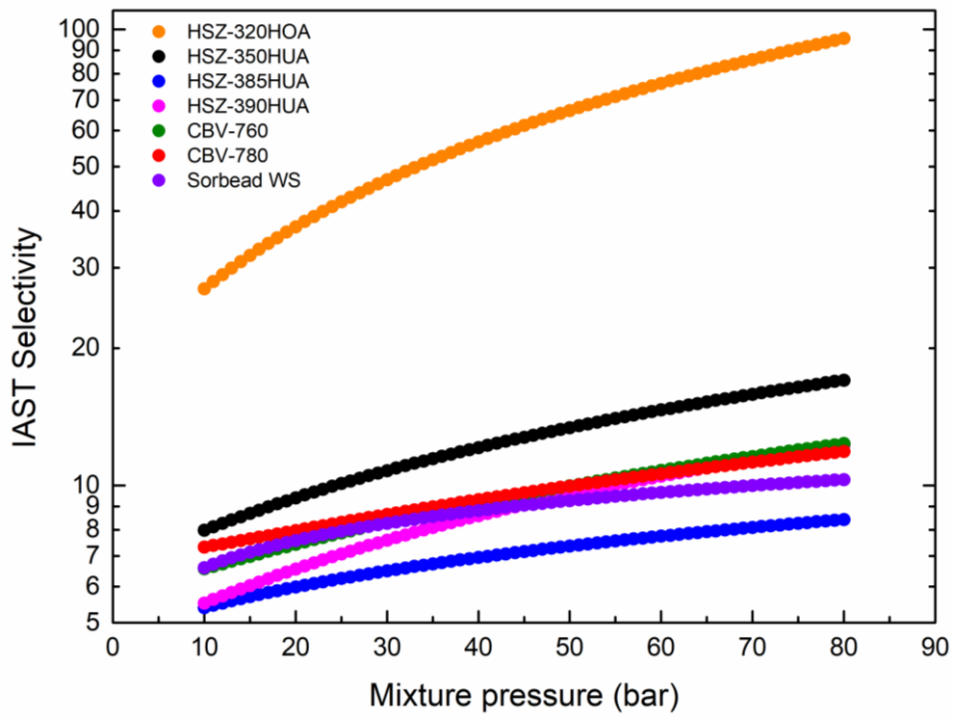

Figure 3.23. IAST selectivity of CO_2 over CH_4 with a gas mixture composition of 30%/70% at 313 K on studied adsorbents.

From the graph, the selectivity of all adsorbents is larger than 5 under the whole pressure range, which means they are all good candidates for high-pressure CO_2/CH_4 separation. The most prominent adsorbent, HSZ-320HOA, the zeolite with the lowest Si/Al ratio among our studied materials, outperforms others by several folds. Since the adsorbent with the strongest CO_2-solid interaction has the highest selectivity, this result suggests that the IAST selectivity is counting

mostly on the material properties than other considerations. We will evaluate the performance of the adsorbents via process simulations to confirm and assess the influence of other factors.

3.4.5 Process simulations

Process simulations were carried out in Aspen Adsorption. The gas isotherms were input into the simulation tools in the form of Langmuir model fitting parameters, and then was used in the extended Langmuir model (Equation 2.7) to predict the mixture adsorption loadings within the simulation. For each simulation, the molar flowrate of the feed gas at the feed & adsorption step was set to be constant ($0.04\ mol/s = 144\ mol/hr$) while the adsorption step time was adjusted to achieve the product specification, 95% purity for CH_4 product in our study. The results from the simulation are summarised in Table 3.11. Although CO_2 purity and recovery are still indicative parameters, considering their coupled relationship with the CH_4 purity and recovery governed by the mass conservation law, the performance of the adsorbents can be solely determined by a single factor of CH_4 recovery.

Table 3.11. Summary of the simulation results on studied adsorbents

	Feed composition	*Feed temperature (K)*	*Feed step time (sec)*	*CO_2 purity ($mol\%$)*	*CO_2 recovery ($mol\%$)*	*CH_4 recovery ($mol\%$)*
HSZ-320HOA	30% CO_2 70% CH_4	313	48.0	50.52	93.45	61.30
HSZ-350HUA			58.9	49.34	92.61	58.52
HSZ-385HUA			63.4	50.11	93.35	60.58
HSZ-390HUA			52.8	48.31	92.99	57.04
CBV-760			51.8	47.74	93.77	56.20
CBV-780			60.2	50.26	93.40	60.84
Sorbead® WS			74.0	57.11	92.03	**71.12**

The simulation results show that Sorbead® WS is a better adsorbent compared with other studied zeolites, and this is a completely different conclusion as indicated by the results of IAST selectivity. Since results from the ideal selectivity only takes account of the pure component isotherms parameters, while process

simulation includes every aspect from the factor of adsorbents to the influence by the cycle configuration, it is obvious that the results of the simulation are more persuasive and that using the ideal selectivity can lead to misleading conclusions.

The feed step times for different adsorbents in Table 3.11 display possible clues why Sorbead® WS outperforms other adsorbents. This feed time is adjusted to a value to ensure the composition of the top product is 95 mol% of CH_4. A larger feed step time with constant molar flowrate means that the adsorbent can absorb more gas molecules before the breakthrough gas stream contains more than 5 mol% CO_2. This statement is generally admitted when one adsorbent has a larger adsorption capacity than the other one. However, according to the measured adsorption isotherms of, for instance, HSZ-320HOA in Figure 3.16 and Sorbead® WS in Figure 3.22, under the condition in simulation (50 bar, 70% CO_2/30% CH_4) HSZ-320HOA has larger adsorption capacities for both CO_2 and CH_4 than Sorbead® WS. From the concentration profiles provided by Figure 3.24, it clearly shows that when we specified the top product to be 95 mol% of CH_4, Sorbead® WS, which has a lower equilibrium adsorption capacity, adsorbed more CO_2 in the feed step than HSZ-320HOA, which has a higher adsorption capacity. Thus, features other than adsorption capacities here govern the adsorbent performance, in particular the condition of the bed at the start of the feed step, which is dependent on the extent of regeneration of the bed during the cycle.

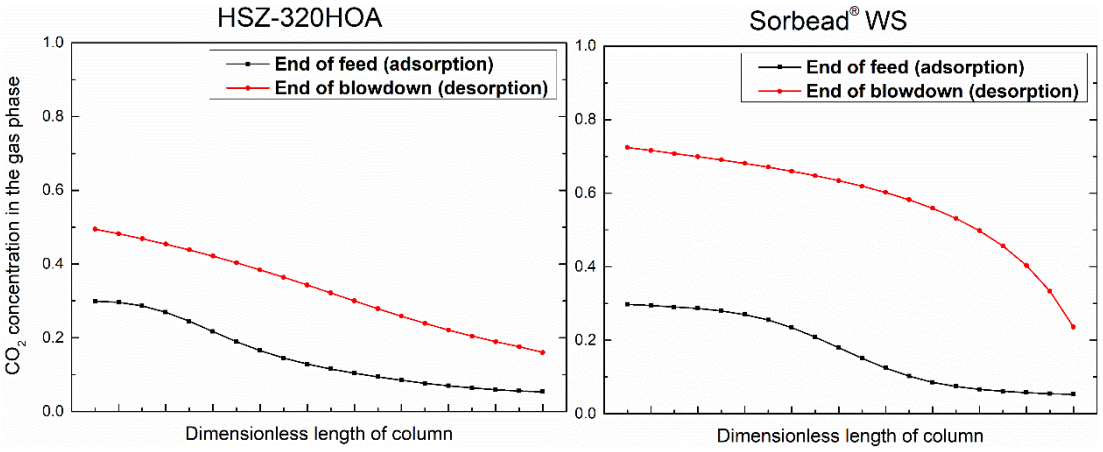

Figure 3.24. Mole fraction profile of CO_2 in the gas phase at the end of different steps during one cycle in simulation

Previous literature has studied the regenerability of the adsorbent in the

application of natural gas sweetening process [96]. According to the amount adsorbed profiles shown in Figure 3.25, Sorbead® WS exhibited much better bed regeneration than HSZ-320HOA. The gap between the two profile lines in the figure represents the amount adsorbed of the bed in the adsorption step. The adsorption bed packed with Sorbead® WS is "cleaner" than that with HSZ-320HOA after the desorption step. Subsequently, within a cycle operation scheme, Sorbead® WS can adsorb more gas in the next cycle. Overall, although HSZ-320HOA has a higher adsorption capacity, Sorbead® WS can proceed with a higher throughput per cycle because of its better regenerability and hence higher "working capacity".

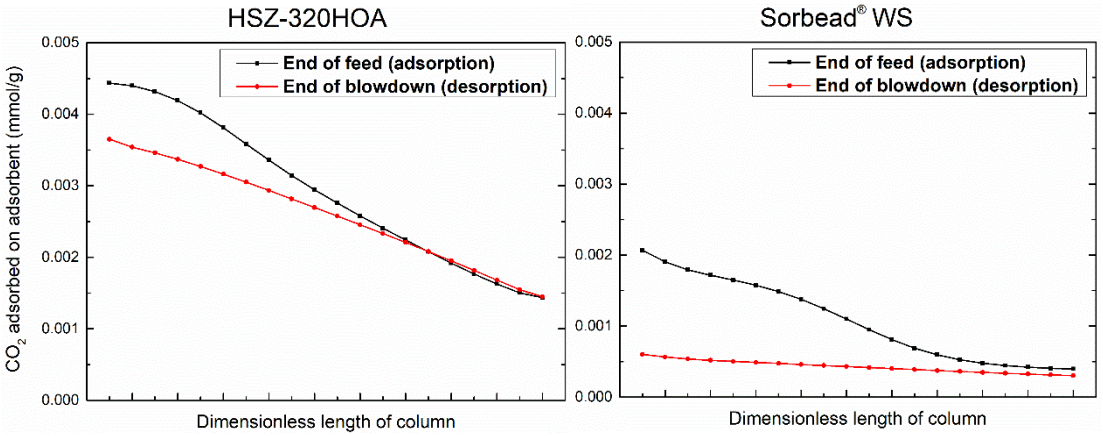

Figure 3.25. Amount adsorbed profile of CO_2 on the adsorbent at the end of different steps during one cycle in simulation

The simulation results raise an interesting question that is worth considering: how many and which factors should we include when we want to evaluate the adsorbent without experiment or simulation? In the next chapter, we further investigate this issue.

3.5 Summary

In this chapter, the adsorption properties of six zeolites (HSZ-320HOA, HSZ-350HUA, HSZ-385HUA, HSZ-390HUA, CBV-760, and CBV-780) and one silica-gel (Sorbead® WS) were measured. The textural structures of selected zeolites were characterized by carrying out N_2 adsorption measurements at 77.3 K.

Intermediate-pressure adsorption isotherms (up to 10 bar) of CO_2 and CH_4 at three temperatures were determined volumetrically by ASAP 2050. With the low adsorption coverage data at different temperatures, the isosteric heats of

adsorption for each gas were calculated using the Clausius-Clapeyron equation.

High-pressure adsorption equilibrium from gravimetric adsorption experiments for CH_4 and CO_2 were measured at three temperatures (303 K, 313 K and 333 K) for all studied materials. The excess adsorption loadings were obtained directly from the readings of a magnetic suspension balance, while the absolute adsorption loadings were calculated under an assumption of fixed density of the adsorbed phase. The Toth model and Langmuir model were used to fit the absolute adsorption isotherms, and both sets of model parameters can be directly used in the future process simulations.

The analysis of the selectivity of CO_2 over CH_4 shown that HSZ-320HOA had the highest IAST selectivity. However, adsorbent evaluation by PSA process simulations conducted by Aspen Adsorption presented completely different results. In the simulations, the gaseous mixture with 30% CO_2/70% CH_4 was separated to get a CH_4 enriched stream with a purity of 95%. The results showed with same final product purity, Sorbead® WS could achieve higher CH_4 recovery (71.12%) than other examined adsorbents.

CHAPTER 4

NOVEL ADSORBENT PERFORMANCE INDICATOR – ADIABATIC COLUMN WORKING SELECTIVITY

4.1 Introduction

In the last chapter, we have characterized six new zeolites and one silica-gel as the adsorbents for CO_2 removal from natural gas. We employed a common performance indicator, IAST selectivity, and process simulation to evaluate the adsorbent performance. However, the results of the two methods are inconsistent. This raises an interesting question “Can any performance indicators obtain similar results as process simulation or experiments?”. We have reviewed most of the common adsorbent performance indicators in Section 2.3. To overcome the known limitations of the existing indicators, we propose a novel adsorbent process performance indicator in this chapter that includes a process factor, the gas phase loading. The existing metrics and the newly proposed indicator are used to screen our characterized seven adsorbents, as well as two MOFs from reference, for the application to CO_2/CH_4 separation.

4.2 Development of a novel adsorbent process performance indicator

Due to the dynamic nature of the adsorption process, the industrial practice is a complicated and integrated process, containing 10 more parallel columns and 20 more sequential steps, to accomplish a certain objective, while the quintessence of such processes can be referred to the first PSA cycle – Skarstrom cycle [97]. Two adsorption beds and four steps are required in Skarstrom cycle, which is demonstrated in Figure 4.1. It can be future simplified to only two crucial steps: adsorption and desorption, which is demonstrated by the schematic in Figure 4.2.

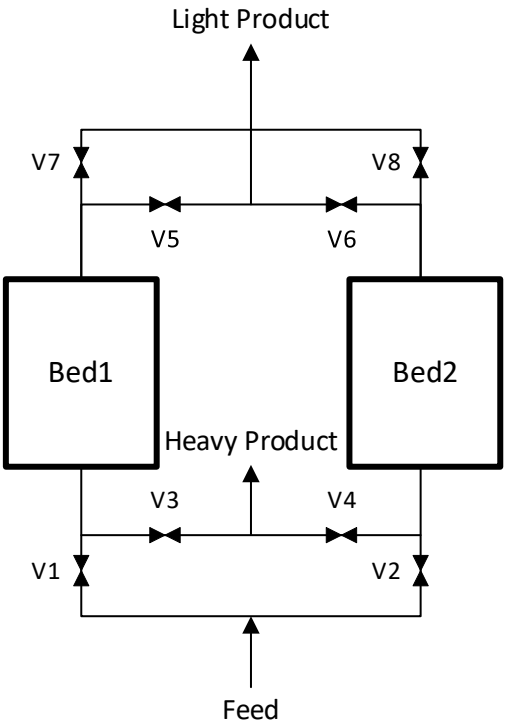

Bed 1	Feed	Blow	Purge	Pressurise
	V1,V7	V3	V5,V3	V1
Bed 2	Purge	Pressurise	Feed	Blow
	V6,V4	V2	V2,V8	V4

Figure 4.1. Schematic of a Skarstrom cycle PSA process

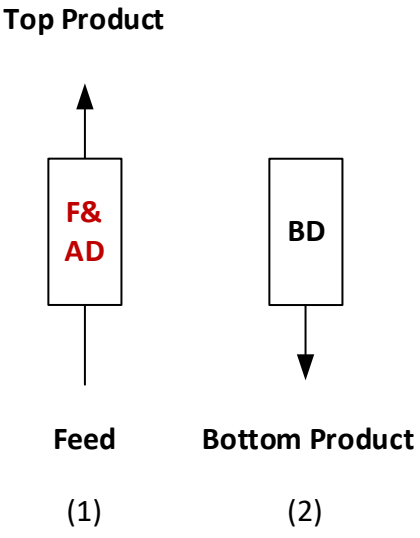

Figure 4.2. Schematic of a basic PSA process

In a PSA process, the feed gas stream at high pressure passes through the adsorption column, where the heavy component is selectively adsorbed by the

adsorbent and the light component elutes from the exit of the column. The adsorption step stops before the adsorbent is saturated by the heavy component. A subsequent desorption step then desorbs the trapped heavy component by releasing the bed pressure to regenerate the adsorbent for the next adsorption cycle. A simple mass balance calculation over this process implies that the bottom product with enriched heavy component is equal to what the adsorption column loaded during the adsorption step. Correspondingly, the top product with the light component enriched is the feed gas without the trapped portion during the adsorption step. Hence, to examine the process performance, i.e. checking the purity and recovery of the light and heavy product, knowing the column loading at the adsorption step is essential.

In the previous studies as discussed in Section 2.3, the column loading at the end of the adsorption step was generally considered as the equilibrium uptake in the adsorbed phase, while the compounds in the void space were assumed to be insignificant. Based on such a fixed mindset, the existing adsorption metrics attached more importance to the adsorbed phase, ignoring the amount of the gas phase compressed in the void space of the adsorption column. The assumption of column loading being equal to solid equilibrium loading was reasonably good when the corresponding adsorption pressure was relatively low.

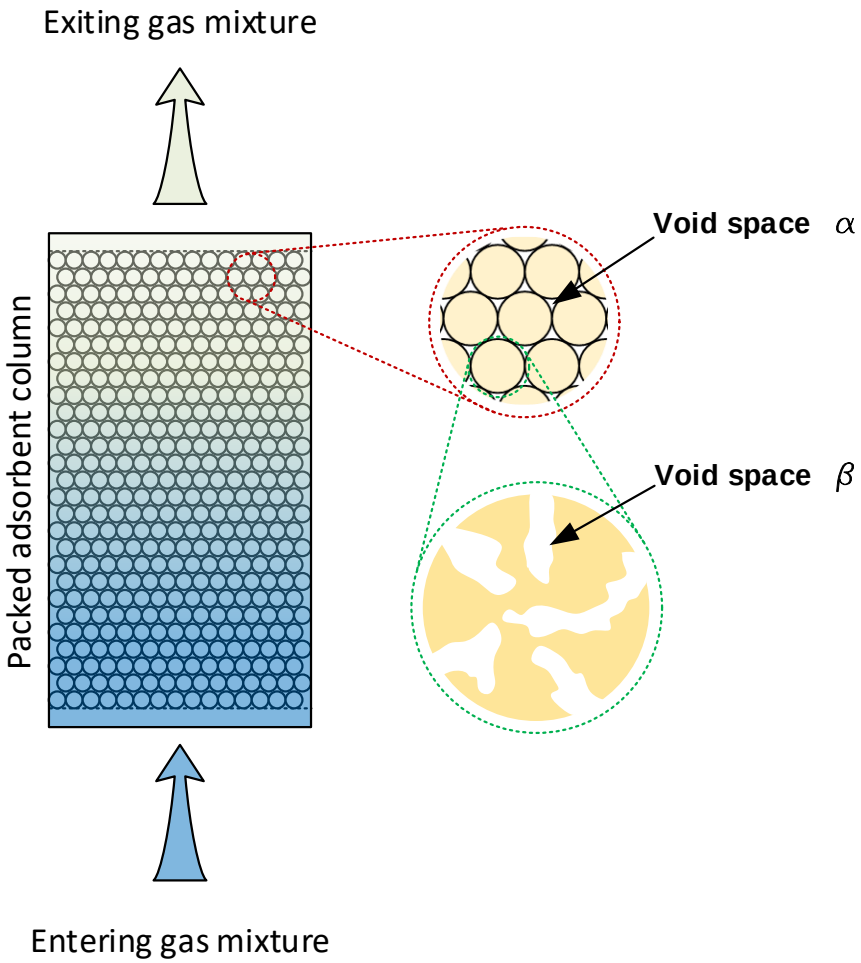

Figure 4.3. **Scheme showing the void space in the adsorption column**

However, the void space of the column is a crucial factor for the adsorption process, particularly when the feed pressure increases. There are two types of void space existing in the adsorption column (Figure 4.3). Void space α is the interspace between the adsorbent particle, while void space β is the large porous space in the adsorbent particle. Yang states that the gas mixture in the void space of the bed cannot be recovered as a useful product, and the overall recovery suffers if the voidage of the column was large [12]. In sophisticated industrial adsorption processes, there are steps, like pressure equalization and purging, whose purposes are to control the gas amount in the void space to the desired targets. For the applications occurring under elevated pressures like pre-combustion capture and natural gas sweetening, the amount of adsorbates stored in the gas phase would increase linearly with the increasing pressure, while the adsorbed phase would eventually be saturated due to the limitation of the adsorption capacity. In this case, the assumption of no gas phase storage is

no longer valid. The heavy component stored in the gas phase under high pressure would grow significantly to a comparable amount to that in the adsorbed phase. The amount of the light component in the gas phase could be much higher, even several times than that in the adsorbed phase depending on the applications.

Figure 4.4 demonstrates an example case for the application of natural gas sweetening. The feed gas was comprised of 30% CO_2 and 70% CH_4 at a total pressure of 100 bar. The adsorption column was filled with an ultra-stable Y zeolite with an overall bed porosity of 0.71. As can be observed, the overall loading of methane in the column was much more than that adsorbed on the adsorbent, as the total pressure approached to the high end. Without a doubt, the adsorption metrics which only consider the solid loading would not be able to produce acceptable results.

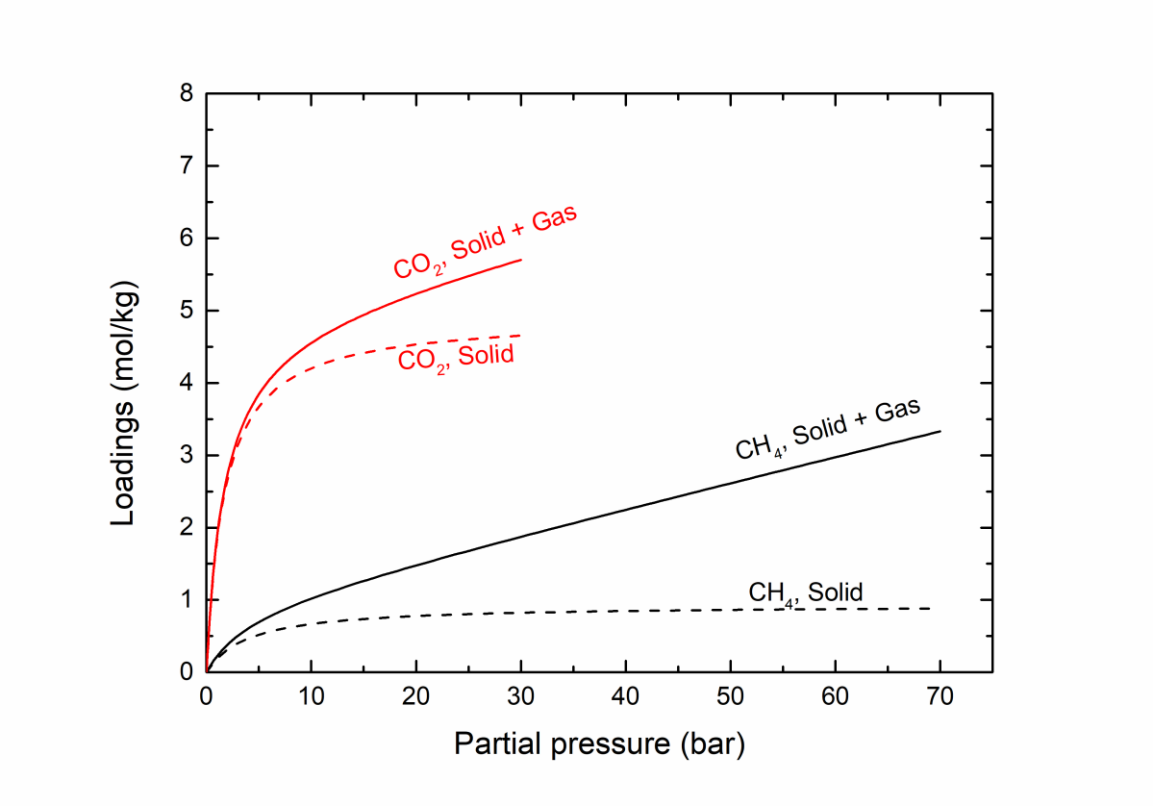

Figure 4.4. A demonstration showing the relationship between the solid loadings and the gas loadings in a high-pressure CO_2/CH_4 separation process

To contain the feature of the adsorbate stored in the gas phase, we here define a new term, column adsorption isotherms $n_{i,column}$, to represent the specific

loading of one component in both solid and gas phases under certain conditions. The column adsorption isotherms in a unit of $[mol/kg]$ is calculated as Equation 4.1, the sum of the solid loading per unit mass of the adsorbent and the amount stored in the gas phase with the same volume that the unit mass of adsorbent occupies in the adsorption column.

$$n_{i,column} = n_{i,solid} + n_{i,gas} \qquad \textbf{Equation 4.1}$$

The solid loading term, $n_{i,solid}$, can be estimated using any available pure and mixture adsorption isotherm model. For example, if the solid loading follows the extended Langmuir model, it can be expressed as Equation 4.2.

$$n_{i,solid} = \frac{n_i^* b_i \exp\left(\frac{Q_i}{RT}\right) P_i}{1 + \sum b_i \exp\left(\frac{Q_i}{RT}\right) P_i} \qquad \textbf{Equation 4.2}$$

The gaseous term, $n_{i,gas}$, needs to be computed in accordance with an equation of state (EoS) given a specific P and T condition. Additionally, to make the solid loading term and the gaseous term additive, they must be evaluated in the same base. Thus, the bulk density (ρ_{bulk}) of the adsorbent and the total voidage (ε) of the column are required. The former gives a clue of the volume of a unit mass of adsorbent when stacked in the adsorption column. The latter can be used to calculate the volume of the gas phase in the same space as the unit mass of adsorbent. If ideal gas is assumed, the gas loading term can be written as in Equation 4.3.

$$n_{gas,i} = \frac{P_i \varepsilon}{RT \rho_{bulk}} \qquad \textbf{Equation 4.3}$$

Note that according to the expressions of Equation 4.2 and Equation 4.3, both solid and gas loadings are related to the temperature and the partial pressure of the component. Therefore, the column loadings under any operation conditions are accessible. Following the same way of defining the working capacity with only solid loadings as in Section 2.3.6, the column working capacity, $WC_{i,column}$, is defined with column loadings between the adsorption and desorption conditions in Equation 4.4. So is the column working selectivity, β_{column}, defined in Equation 4.5, as the ratio of the column working capacity of the heavy and light

component. The column working selectivity is the new adsorption process performance indicator we propose to evaluate and screen adsorbent for process design.

$$WC_{i,column} = n_{i,column}(P_{ad}, T_{ad}, y_{i,ad}) - n_{i,column}(P_{de}, T_{de}, y_{i,de}) \quad \textbf{Equation 4.4}$$

$$\beta_{column} = \frac{WC_{B,column}}{WC_{A,column}} \quad \textbf{Equation 4.5}$$

The new indicator contains all features that the traditional working selectivity holds, i.e. the solid equilibrium loading and the working capacity between adsorption and desorption conditions. To approach the actual process as much as possible, the adiabatic assumption is adopted, which means the temperature of the desorption step needs to be determined before the calculation of the indicator. A more specific name of this indicator would be “adiabatic column working selectivity”.

In addition to the features already considered by other indicators, the adiabatic column working selectivity contains a new factor, the absolute amount of the gas in the void space. This factor reflects the impact of the configuration of the adsorption column, which is a new category of factors other than the property of the adsorbent and the cyclic operating parameters of the process.

To illustrate the versatility of this adiabatic column working selectivity, it will be used along with other existing indicators to compare a series of adsorbents for a CO_2/CH_4 separation process in this chapter.

4.3 Materials and simulation methods

4.3.1 Adsorbents

Nine adsorbents are employed for the adsorbent screening to examine the feasibility of the new adsorption performance indicator. They are six zeolites (HSZ-320HOA, HSZ-350HUA, HSZ-385HUA, HSZ390HUA, CBV-760 and CBV-780), one silica-gel (Sorbead® WS) and two MOFs (UiO-66, and UiO-67). Structures of the zeolites and the silica-gel Sorbead® WS have been characterized in Chapter 3, so have their adsorption isotherms of CO_2 and CH_4 at high pressure and different temperatures. We also selected two MOFs, UiO-

66 and UiO-67, as the candidates to diversify the adsorbent types. They were reported to have suitable CO_2 capacities and mildly non-linear adsorption isotherms for the application of CO_2/CH_4 separation at high pressure [98].

The textural properties of the selected adsorbents are listed in Table 4.1 for comparison. The data of zeolites and Sorbead® were retrieved from Chapter 3, and those of MOFs were reported by Cavka et al [98].

Table 4.1. Textural properties of materials studied in this chapter

Adsorbent	*SiO_2/Al_2O_3 ratio*	*Pore volume (cm^3/g)*	*BET surface area (m^2/g)*
HSZ-320HOA	5.5	0.38	540
HSZ-350HUA	10	0.45	673
CBV-760	60	0.55	676
CBV-780	80	0.56	637
HSZ-385HUA	100	0.51	616
HSZ-390HUA	500	0.47	630
Sorbead® WS	N/A	0.45	650
UiO-66	N/A	0.36	1,013
UiO-67	N/A	0.83	2,556

4.3.2 Adsorbent performance indicators

In Section 2.3 of this work, we presented a comprehensive review covering the most common adsorbent performance indicators. The discussed indicators along with the new proposed indicator, the adiabatic column working selectivity, are listed in Table 4.2.

Table 4.2. **Definition of the adsorbent performance indicators considered in this chapter**

Indicator	*Expression*	*Ref.*
Heavy component solid loadings	$n_{CO_2}(P_{ad}, T_{ad}, y_{CO_2,ad})$	[12]
Ideal selectivity	$\alpha_Y = \frac{n_{CO_2}(P,T,y_{CO_2})}{n_{CH_4}(P,T,y_{CH_4})} \cdot \frac{y_{CH_4}}{y_{CO_2}}$	[12]
Isothermal working selectivity	$\beta_{isothermal} = \frac{WC_{CO_2}}{WC_{CH_4}} = \frac{n_{CO_2}(P_{ad}, T_{ad}, y_{CO_2,ad}) - n_{CO_2}(P_{de}, T_{ad}, y_{CO_2,ad})}{n_{CH_4}(P_{ad}, T_{ad}, y_{CH_4,ad}) - n_{CH_4}(P_{de}, T_{ad}, y_{CH_4,ad})}$	[77]
Adiabatic working selectivity	$\beta_{adiabatic} = \frac{WC_{CO_2}}{WC_{CH_4}} = \frac{n_{CO_2}(P_{ad}, T_{ad}, y_{CO_2,ad}) - n_{CO_2}(P_{de}, T_{de}, y_{CO_2,ad})}{n_{CH_4}(P_{ad}, T_{ad}, y_{CH_4,ad}) - n_{CH_4}(P_{de}, T_{de}, y_{CH_4,ad})}$	[78]
Notaro's AFM	$\gamma_{AFM} = WC_{CO_2} \cdot \alpha_{Y,ad} \cdot \frac{\alpha_{Y,ad}}{\alpha_{Y,de}}$	[80]
Rege and Yang's separation parameter	$\gamma_{R\&Y} = \beta_{isothermal} \cdot \alpha_{Y,ad}$	[81]
Wiersum's API	$\gamma_{API} = \frac{(\beta_{isothermal} - 1)^a \cdot WC_{CO_2}^b}{\lvert \Delta H_{CO_2} \rvert^c}$	[82]
Adiabatic column working selectivity	$\beta_{column} = \frac{WC_{CO_2,column}}{WC_{CH_4,column}} = \frac{n_{CO_2,column}(P_{ad}, T_{ad}, y_{CO_2,ad}) - n_{CO_2,column}(P_{de}, T_{de}, y_{CO_2,de})}{n_{CH_4,column}(P_{ad}, T_{ad}, y_{CH_4,ad}) - n_{CH_4,column}(P_{de}, T_{de}, y_{CH_4,de})}$	This work

4.3.3 Adsorption process simulations

To evaluate the process performance of selected adsorbents for the CH_4/CO_2 separation, we continued to employ the nine-step PSA cycle with the help of the commercial simulation program, Aspen Adsorption V10. The same simulation configuration is used in Chapter 3. The detailed description can be found in Section 3.2.4.

The details of the adsorption bed are listed together with the configuration of the operating conditions in Table 4.3. Bed characteristics used in the Aspen Adsorption and simulated operating conditions. The bulk density and voidage of the packed bed for zeolites and silica were retrieved from a previous work from our research group [51]. Data for UiO-66 and UiO-67 have not been reported to date. Therefore, we instead used the corresponding data of another common MOF material, Cu-BTC, which was available in references [99,100].

Table 4.3. Bed characteristics used in the Aspen Adsorption and simulated operating conditions

Parameters	*Value*		
Packing length (mm)	600		
Internal bed diameter (mm)	80		
Feed pressure (bar)	50		
Feed temperature (K)	313		
Feed composition	70% CH_4 / 30% CO_2		
Desorption pressure (bar)	1		
Methane product purity specification	95% CH_4		
	Zeolites	**Sorbead® WS**	**MOFs**
Packing bulk density (kg/m^3)	750	800	350
Particle size (mm)	2		
Inter-particle voidage, ε_i	0.37	0.37	0.37
Intra-particle voidage, ε_P	0.54	0.54	0.75

4.4 Results and discussion

4.4.1 Adsorption isotherms

The adsorption isotherms of CO_2 and CH_4 on selected adsorbents at 313 K were recreated in Figure 4.5 using the data available in Chapter 3 and the reference [98]. Two adsorption isotherm models, the Langmuir model (Equation 4.6) and Toth model (Equation 4.7), were employed to fit the experimental data.

$$Langmuir\ Model: \quad n_i = \frac{n_i^* b_i \exp\left(\frac{Q_i}{RT}\right) P_i}{1 + b_i \exp\left(\frac{Q_i}{RT}\right) P_i} \qquad \textbf{Equation 4.6}$$

$$Toth\ Model: \quad n_i = \frac{n_i^* b_i \exp\left(\frac{Q_i}{RT}\right) P_i}{\left[1 + \left(b_i \exp\left(\frac{Q_i}{RT}\right) P_i\right)^t\right]^{\frac{1}{t}}} \qquad \textbf{Equation 4.7}$$

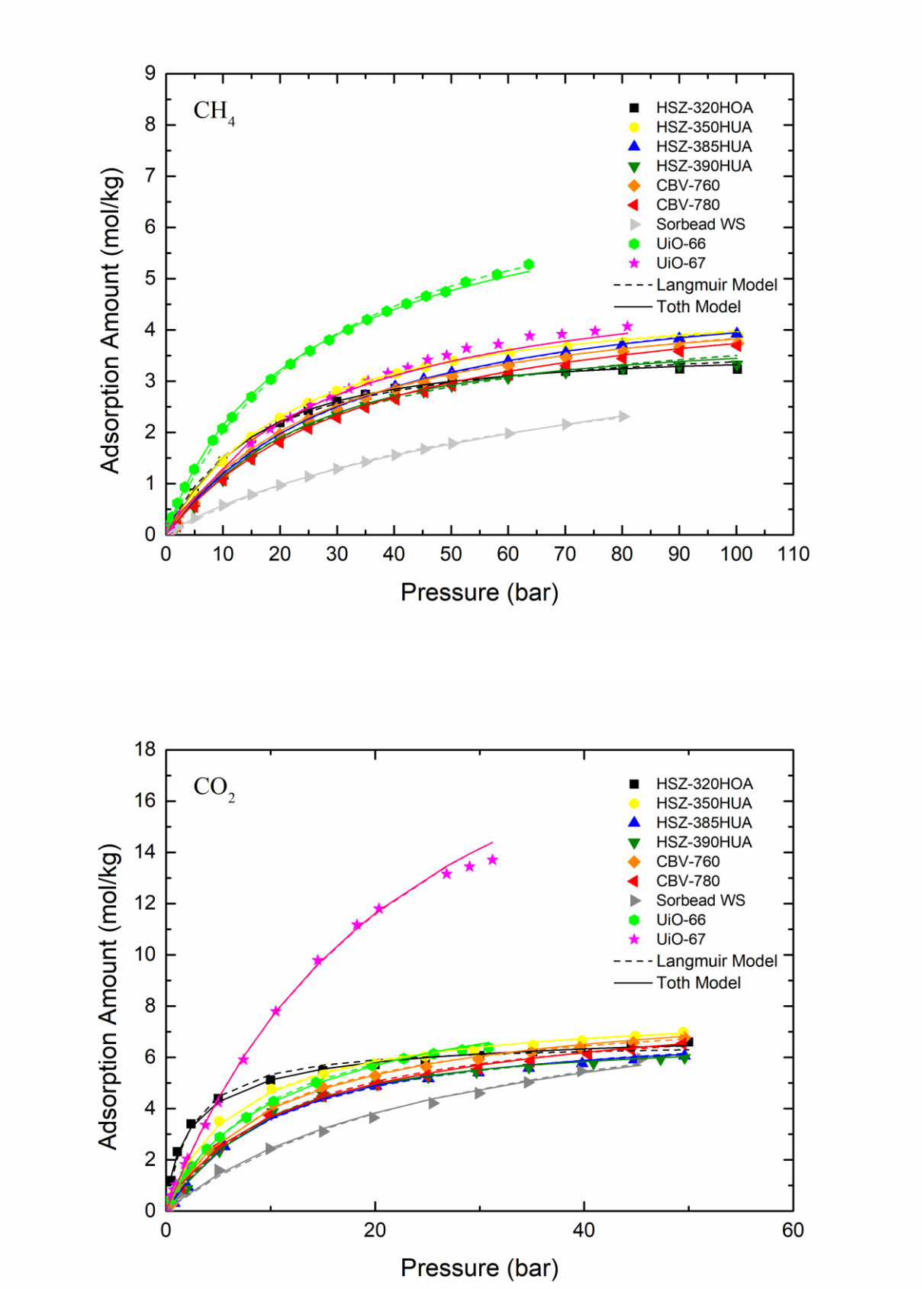

Figure 4.5. **Adsorption isotherms for methane and carbon dioxide at 313 K on selected adsorbents**

The structure of six investigated Faujasite zeolites here are very similar. The main difference of these zeolites is the ratio of the amount of silica and alumina in their framework as shown in Table 4.1. It can be observed from Figure 4.5, HSZ-320HOA, the one with the lowest Si/Al ratio, has the steepest CO_2 isotherm shape and is saturated at relatively low pressure. When the Si/Al ratio increases from 5.5 to 500, the shape of the CO_2 isotherms becomes more linear, and the saturation pressure grows. As the saturation pressure rises, the equilibrium CO_2 loadings on high Si/Al ratio zeolites within the examined pressure range are further below their saturated loadings. This appears as the solid loadings of the high Si/Al ratio zeolites have relatively lower uptakes than those of the lower Si/Al ratio zeolites. Nonetheless, with a glimpse of Figure 4.5, the differences among zeolites are quite small when compared with other types of adsorbents. Their similarity in terms of the structure and adsorption characteristics makes them hard to evaluate from a cursory examination. Any indicators aiming to distinguish these zeolites are required to have high enough resolution to tell one's advantage from tiny differences compared to their peers.

Table 4.4. **Adsorption isotherms fitting parameters by Langmuir Model**

Adsorbent	*Gas*	$n_i^* \ (mol \cdot kg^{-1})$	$b_i \times 10^5 \ (bar^{-1})$	$Q_i \ (kJ \cdot mol^{-1})$	RSS
HSZ-320HOA	CH_4	3.91 ± 0.04	2.18 ± 0.78	20.77 ± 0.95	0.298
	CO_2	6.60 ± 0.06	0.50 ± 0.45	29.45 ± 2.38	1.825
HSZ-350HUA	CH_4	4.88 ± 0.03	3.54 ± 0.71	18.63 ± 0.54	0.156
	CO_2	7.87 ± 0.06	1.06 ± 0.39	24.85 ± 0.97	0.509
CBV-760	CH_4	4.96 ± 0.04	3.93 ± 0.84	17.65 ± 0.56	0.175
	CO_2	8.08 ± 0.08	0.63 ± 0.20	25.12 ± 0.87	0.461
CBV-780	CH_4	5.04 ± 0.05	6.12 ± 1.15	16.05 ± 0.50	0.134
	CO_2	7.94 ± 0.10	0.76 ± 0.30	24.41 ± 1.06	0.600
HSZ-385HUA	CH_4	5.30 ± 0.03	6.66 ± 0.70	15.91 ± 0.28	0.050
	CO_2	7.51 ± 0.10	0.75 ± 0.32	24.53 ± 1.13	0.728
HSZ-390HUA	CH_4	4.44 ± 0.06	1.31 ± 0.46	20.77 ± 0.93	0.331
	CO_2	7.34 ± 0.10	0.71 ± 0.35	24.88 ± 1.31	0.798
Sorbead® WS	CH_4	4.21 ± 0.07	5.25 ± 0.68	14.71 ± 0.35	0.034
	CO_2	9.61 ± 0.40	0.77 ± 0.36	21.76 ± 1.29	0.884
	CH_4	7.50 ± 0.13	4.30 ± 1.26	17.57 ± 0.80	3.796

UiO-66	CO_2	8.65 ± 0.05	1.07 ± 0.10	23.76 ± 0.25	0.964
UiO-67	CH_4	5.29 ± 0.12	1.99 ± 0.77	19.50 ± 1.03	3.747
	CO_2	25.37 ± 0.22	1.10 ± 0.08	21.46 ± 0.20	3.555

Table 4.5. **Adsorption isotherms fitting parameters by Toth Model**

Adsorbent	*Gas*	$n_i^* \ (mol \cdot kg^{-1})$	$b_i \times 10^5 \ (bar^{-1})$	$Q_i \ (kJ \cdot mol^{-1})$	t_i	*RSS*
HSZ-320HOA	CH_4	3.59 ± 0.05	1.96 ± 0.60	20.67 ± 0.80	1.30 ± 0.07	0.204
	CO_2	7.41 ± 0.19	1.63 ± 1.15	27.55 ± 1.75	0.67 ± 0.04	0.872
HSZ-350HUA	CH_4	4.60 ± 0.07	3.33 ± 0.62	18.63 ± 0.49	1.16 ± 0.05	0.126
	CO_2	8.18 ± 0.19	1.33 ± 0.51	24.47 ± 0.98	0.90 ± 0.05	0.459
CBV-760	CH_4	4.78 ± 0.13	3.88 ± 0.83	17.94 ± 0.56	1.07 ± 0.06	0.170
	CO_2	8.94 ± 0.40	0.78 ± 0.32	24.66 ± 1.05	0.84 ± 0.07	0.639
CBV-780	CH_4	5.02 ± 0.17	6.14 ± 1.18	16.04 ± 0.51	1.01 ± 0.06	0.134
	CO_2	9.56 ± 0.54	1.17 ± 0.39	23.73 ± 0.86	0.71 ± 0.06	0.355
HSZ-385HUA	CH_4	5.07 ± 0.08	6.51 ± 0.66	15.94 ± 0.27	1.08 ± 0.03	0.044
	CO_2	7.13 ± 0.23	0.66 ± 0.30	24.72 ± 1.16	1.13 ± 0.10	0.680
HSZ-390HUA	CH_4	3.91 ± 0.09	1.25 ± 0.38	20.64 ± 0.79	1.36 ± 0.09	0.235
	CO_2	6.72 ± 0.17	0.55 ± 0.26	25.28 ± 1.21	1.28 ± 0.11	0.612
Sorbead® WS	CH_4	9.72 ± 0.68	3.68 ± 0.19	14.50 ± 0.12	0.53 ± 0.02	0.004
	CO_2	10.02 ± 0.01	6.84 ± 0.31	22.26 ± 1.23	0.89 ± 0.04	0.775
UiO-66	CH_4	7.50 ± 0.13	4.30 ± 1.26	17.57 ± 0.80	1.01 ± 0.06	3.796
	CO_2	8.65 ± 0.05	1.07 ± 0.10	23.76 ± 0.25	0.71 ± 0.06	0.964
UiO-67	CH_4	5.41 ± 0.42	2.00 ± 0.79	19.50 ± 1.05	0.96 ± 0.11	3.744
	CO_2	24.14 ± 0.81	1.13 ± 0.09	21.46 ± 0.20	1.06 ± 0.04	3.510

Sorbead® WS has the most linear adsorption isotherms. The adsorption amounts of both CO_2 and CH_4 on Sorbead® WS are far from the saturated uptakes within the pressure range of interest in this work and consequently lower than other investigated adsorbents. Low CO_2 loading is not desired because it could impair the CO_2 selectivity. However, the CH_4 loading on Sorbead® WS is less than other adsorbents' loading as well, only half of the studied zeolites and almost one-third of that on UiO-66. Several previous researchers have stated that the ability of an adsorbent to reject the less adsorbed component, i.e. CH_4 in this application,

could be more important than adsorbed more CO_2 [75,76,83]. Hence, Sorbead® WS could be expected to be a good adsorbent for CO_2/CH_4 separation due to its lowest CH_4 loading, though the eventual ranking of the CO_2 selectivity remains unclear before using the performance indicators.

UiO-66 has the highest CH_4 loading among the selected adsorbents when the CO_2 loading is equivalent to that of the zeolites, while UiO-67 presents the highest CO_2 loadings when the CH_4 loading is a little bit higher than zeolites. Without further analysis, we can affirm that the performance of UiO-67 for CO_2/CH_4 separation would be much better than that of UiO-66 under the same operating conditions. But due to the big difference of the physical properties between MOFs and other adsorbents, especially the bulk density of MOFs (which is normally far smaller than zeolites and silica gel), it is still difficult to tell if MOFs are superior for the CO_2/CH_4 separation.

4.4.2 Adsorbent screening using the existing indicators

Using the process parameters in Table 4.3 as well as the adsorption isotherms fitting parameters, the existing indicators listed in Table 4.2 can be calculated for the selected adsorbents. The results of all indicators are listed in Table 4.6. For all indicators, a larger number suggests better performances. To allow a quick comparison, we formatted the table such that the maximal number of one indicator was shaded as navy blue and the minimal number was shaded as red, while the median was left without shading. Other numbers between the maximum and minimum were coloured proportionally. The parameter used as the "benchmark" for comparison was the methane recovery, as calculated by Aspen Adsorption using the full cycle detailed earlier. The quality of each metric may be judged, therefore, by how close the ranking for that metric corresponds to the ranking provided by the Aspen Adsorption methane recovery.

The CO_2 equilibrium loadings at the feed condition in the table were the competitive loadings calculated by the extended Langmuir model. UiO-67 had the highest CO_2 loadings while the Sorbead® WS had the least. The results were reasonable and in accordance with the adsorption isotherm measurements.

Ideal selectivity produced a different performance ranking compared with the

CO_2 equilibrium loading. The results of ideal selectivity show HSZ-320HOA to be the best adsorbent. It can be attributed to the sharp non-linearity of the CO_2 isotherms on HSZ-320HOA, which implies stronger interactions with CO_2. This steep CO_2 isotherms also leads to more advantages when calculating the competitive adsorption amount and consequently results in a higher ideal selectivity of CO_2 over CH_4. The lowest ranking of UiO-66 is because CO_2 and CH_4 isotherms of UiO-66 shows similar linearity and saturated loadings so that the selective adsorption towards CO_2 is weak.

The Isothermal working selectivity was calculated between the feed condition and desorption condition. It was interesting that the ranking from isothermal working selectivity agreed with the ranking of ideal selectivity. The fact that the isothermal working selectivity and ideal selectivity showed the same trends but calculated in different ways revealed that both indicators capture the same feature of the adsorbents when no thermal effect was considered.

With the introduction of thermal effects into the indicator, the best adsorbent expected by adiabatic working selectivity was Sorbead® WS, followed by UiO-67. The only difference between the isothermal working selectivity and the adiabatic selectivity is that the desorption solid loadings are calculated at different temperatures. The ranking shift between these two indicators demonstrated the difference in the sensitivity of the adsorbent isotherms towards the change of temperature. In the meantime, the significant changes in the performance rankings between the isothermal and adiabatic working selectivity show the necessity of including the thermal effect into the performance indicator.

It should be noted that the gas composition at the desorption condition, as well as the temperature under the adiabatic assumption, were unknown variables without further process simulations or experiments. For the desorption composition, we have tried several values between the feed (70% CH_4) and the proposed heavy product (5% CH_4). The result number of individual adsorbents would change accordingly, however, the overall ranking did not shift because of the change. Thus, we used an average value of 20% CH_4 from our previous simulation results. Similarly, we set the desorption temperature to be 273 K, because the temperature swing for the studied PSA process is around 40 K

according to our simulation results. These are solely initially guessed. Considering the purpose of this chapter, we would stick to these assumptions for all occasions requiring the information at the desorption condition.

The lumped parameters emphasized different aspects of the adsorption processes; thus, they ranked the adsorbents in different ways. Rege & Yang's separation parameter is calculated as the product of ideal selectivity and the isothermal working selectivity. Because the latter two indicators already predicted the same ranking, the lumped one will just give the same result.

Notaro's AFM is calculated as the CO_2 working capacity times the ideal selectivity, and the ratio of ideal selectivity between the adsorption condition and desorption condition. The ranking of the AFM was almost the same as that of the adiabatic working selectivity and predicted the same best and worst adsorbent. However, the similarity could be a coincidence since the magnitude of difference in the results by AFM between adsorbents did not correlate with that predicted by the adiabatic working selectivity, and the performance of Sorbead® WS by AFM was worse than that by the adiabatic working selectivity.

For bulk CO_2 separation from natural gas, developers of the API suggested to put more weight on the working selectivity of CO_2 and less weight on the ideal selectivity [82]. UiO-67 benefited from its large CO_2 capacity and was predicted to rank the best.

Table 4.6. Adsorbent performance ranking predicted by the existing indicators, process simulation, and the new indicator

	CO_2 loading at feed condition	*Ideal selectivity*	*Isothermal working selectivity*	*Adiabatic working selectivity*	*Rege & Yang's separation parameter*	*Notaro's AFM*	*Wiersum's API*	*Aspen Adsorption (CH_4 recovery)*	*Adiabatic column working selectivity*
HSZ-320HOA	4.415	5.281	3.411	1.073	42.804	2.160	0.852	0.613	0.662
HSZ-350HUA	3.836	2.514	1.998	0.864	12.013	4.875	0.781	0.585	0.650
CBV-760	3.361	2.156	1.805	0.874	9.270	3.931	0.586	0.562	0.659
CBV-780	3.300	2.240	1.896	1.005	10.077	4.208	0.609	0.608	0.723
HSZ-385HUA	3.200	1.992	1.695	0.971	8.014	4.195	0.565	0.606	0.717
HSZ-390HUA	3.046	2.064	1.714	0.827	8.488	3.969	0.468	0.570	0.627
Sorbead® WS	2.248	2.176	1.956	1.404	10.079	4.806	0.355	0.711	0.848
UiO-66	3.338	1.257	1.046	0.562	3.152	3.119	0.439	0.334	0.484
UiO-67	5.554	2.418	2.094	1.383	12.159	15.376	2.253	0.567	0.756

In summary, based on the results of the traditional indicators without conducting simulations, UiO-67 and HSZ-320HOA were recommended as the potential best adsorbents from some of the indicators. HSZ-320HOA could benefit from its steep CO_2 isotherms when the indicators emphasize the competitive selectivity, while UiO-67 took the advantage of high CO_2 loadings, so ranked in the top place in the indicators counting on the working capacity. With the introduction of thermal effect, i.e. under adiabatic and not isothermal assumption, the adiabatic working selectivity predicted a different rank that emphasized Sorbead® WS.

4.4.3 Simulations and the new indicator

The adsorbent ranking predicted by the process simulation via the simulation program Aspen Adsorption is shown in Table 4.6 as well. For a rigorous simulation, the performance evaluation could be referred to as the statement we summarized in Section 2.3.2: on the premise of methane purity reaching the product specification, the recovery of methane should be as high as possible. The simulations for all selected adsorbents were carried out under the same feed gas conditions. Also, the concentration of the light product was set as a process specification, which is 95% of CH_4. Hence, following the evaluation statement, the performance of the adsorbent can be assessed by a single process result, the CH_4 recovery.

We acknowledge that the absolute values of CH_4 recovery from simulations will inevitably deviate from the results of a practical process due to the systematic errors, but the relative ranking predicted by a rigorous simulator like Aspen Adsorption is typically reliable. On the one hand, an adsorption process simulation contains most of the features that a real process has: cyclic operations, pressure-driven material flows, mass transfer resistance, fluid mechanics governed flow velocity, etc. On the other hand, since all factors in the simulations are identical except for the adsorbent changes, the simulator provides an ideal environment, where the difference of the results can only be attributed to the difference of the adsorbents. Therefore, the performance ranking predicted by the Aspen Adsorption was reasonably a referential case to represent the actual adsorbent ranking.

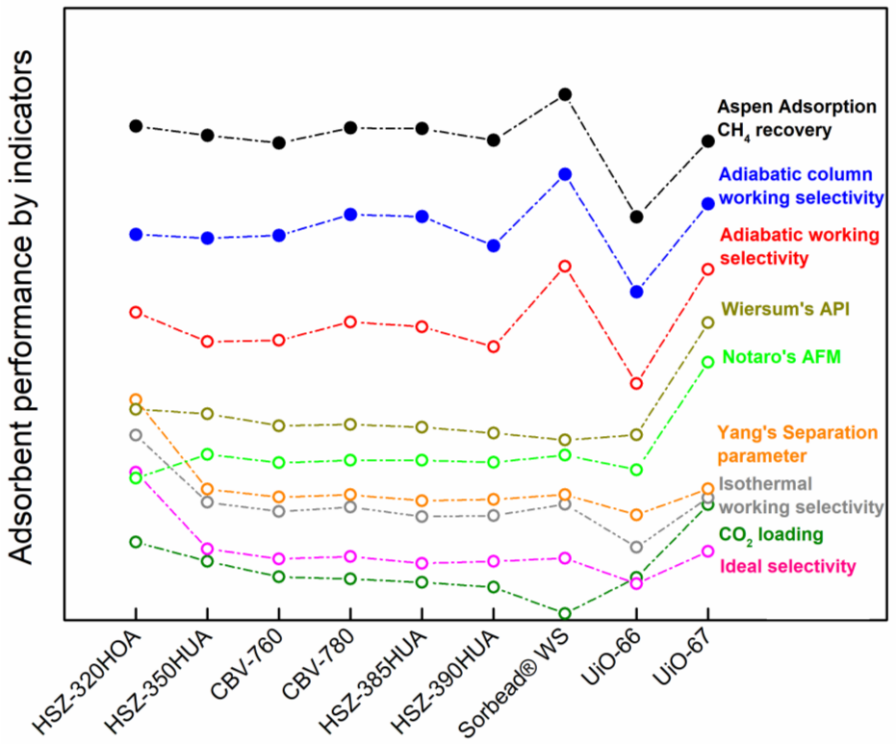

Figure 4.6. **Adsorbent performance by indicators studied in this chapter**

The results of our new indicator, adiabatic column working selectivity, are also shown in Table 4.6. To enable an intuitive comparison, the adsorbent performance in the table are also illustrated in Figure 4.6. The Y-axis of Figure 4.6 is intentionally hidden and the result of each individual performance indicator is rescaled within a range that can be compared with each other. For the result of an individual performance indicator, the higher of the datapoint means the better performance of the corresponding adsorbent indicated in X-axis. As can be seen, the adiabatic column working selectivity agreed very well with the results from the rigorous simulations, while none of the other existing indicators did.

Sorbead® WS was suggested to be the preferred adsorbent for this specific application by the simulation and the adiabatic column working selectivity. But with a quick review of the ranking from other indicators, Sorbead® WS was found to have unsatisfactory rankings on most of them, the lowest CO_2 equilibrium loading, last rank in the API, and unimpressive grades by other indicators, with the exception of the adiabatic working selectivity which ranked it first. This enormous discrepancy implies that it is a synergistic effect of all key adsorption factors which eventually governs the adsorbent's performance. Without any of

the key factors, the prediction of the indicators would be less instructive.

A horizontal comparison between results of the adiabatic working selectivity and the adiabatic column working selectivity reveals the significant effect of involving the gas phase loading in the performance indicator. The only difference between these two indicators is whether the gas phase loading is considered or not. The UiO-67 received a high preference by the adiabatic working selectivity, but when the gas phase loading was included, the performance of UiO-67 was predicted to drop drastically. The major reason is that the framework structure of MOF is loose comparing with zeolites and silica gel. The ultrahigh porosity of MOFs greatly enlarges the specific surface area providing the incredibly large adsorption capacity, however, at the cost of density of the material. The bulk density of UiO-67 used for the calculation was 350 kg/m^3, while for zeolites and silica gel was 700 kg/m^3. The void space percentage per unit volume of the adsorption column packed with UiO-67 was much higher than that filled with zeolites. More void space implied an increasing amount of feed gas was retained in the gas phase and was not able to be selectively adsorbed on the solid and separated. Therefore, it is natural that UiO-67 experienced a huge performance penalty. This is powerful evidence to support the necessity of including the term of the gas-phase loading into the adsorbent performance indicator.

4.4.4 Limitations of the adiabatic column working selectivity

Although the adiabatic column working selectivity seems perfectly correlate well with rigorous Aspen Adsorption simulations in this work, it does have several drawbacks. Firstly, this novel indicator is only effective for equilibrium separation. The inter and intra-particle composition and pressure gradients are absent, and any kinetic factors are not considered in the calculation. The solid adsorbent in the column is regarded to be in thermodynamic equilibrium with the surrounding bulk gas phase at any time. Those adsorbents featured as kinetic separation adsorbents are not able to be screened by this indicator, for example, the carbon molecular sieves (CMS) reported by Rocha et al. [101]. Secondly, because it needs to calculate the solid loading at different temperatures, the adsorption isotherms at least three temperatures are required, and the isotherms must be fitted to a multi-temperature adsorption model. This will somewhat limit the

applicability of the indicator since not all adsorbents have complete sets of adsorption isotherms data available. Last but not least, the desorption conditions, i.e. composition and temperature, are required for the calculation of the column loading at desorption condition. It is difficult to get access to these parameters without simulations or experiments during the adsorbent screening stage. Finding a reliable and rapid method to obtain the desorption conditions for screening adsorbents is a fruitful area for further research.

4.5 Summary

A new adsorbent performance indicator, adiabatic column working selectivity, was defined in this chapter. The new indicator includes the factor of the gas phase loading which has been neglected for all other performance indicators. The adsorbent evaluation and screening on nine adsorbents were carried out using the traditional indicators, rigorous PSA process simulations, as well as the newly defined performance indicators. The results show that only the prediction by the adiabatic column working selectivity can perfectly match the screening results of the rigorous process simulations. It proves the feasibility of the newly defined performance indicator, and also implies the importance of the effect of the gas phase loading in an adsorption process, especially for high-pressure applications like CO_2 removal from natural gas.

CHAPTER 5

SIMPLIFIED SIMULATION MODELS TO OBTAIN PROCESS INFORMATION IN THE DESORPTION STEP IN PSA

In the last chapter, we defined a novel adsorbent performance indicator, the adiabatic column working selectivity. The evaluation results of the novel indicator on the adsorbents we characterized in Chapter 3 agreed with the rigorous simulation results, while other existing adsorbent performance indicators developed under different considerations were not able to predict similar results. The adiabatic column working selectivity offered an opportunity to screen and evaluate adsorbents using a single and simple indicator without conducting extensive experiments or simulations.

Two adsorption process parameters, the temperature and gas-phase composition at the end of the desorption condition, are required to calculate the working capacity between the adsorption and desorption steps. However, neither of these two parameters is accessible without the help of simulations or experiments. It is like a cycle: to evaluate the adsorbents without conducting practical process experiments, we need to employ the adiabatic column working selectivity; but to apply this indicator, we again turn to the process trials to acquire the key parameters. To break this loop requires a simplified method instead of rigorous simulations or experiments to estimate the temperature and gas composition at the desorption step.

We in this work develop a 3-step PSA model based on an earlier work from our research group by Maring and Webley [102]. This new 3-step PSA model is then applied as the fundamental method for a 5-step PSA model which includes the exclusive feature of high-pressure PSA process, the pressure equalization steps. Both simplified models are aimed at finding the desorption conditions of the PSA process.

5.1 Model development and validation

5.1.1 3-step PSA model

The concept of this simplified model is straightforward. As shown in Figure 5.1, it consists of three steps: first, desorption at an initial condition from the highest

pressure P_H to the desorption pressure P_L; then re-pressurisation with the feed stream to increase the bed pressure to feed pressure P_H; and finally collecting the raffinate product at feed pressure with a continuous feed stream until the bed returns to the initial condition.

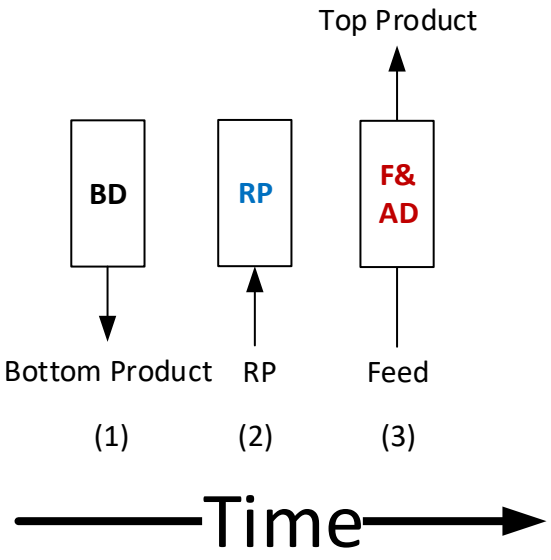

Figure 5.1. Schematic of the 3-step PSA cycle applied in the simplified model. BD – Blowdown; RP – Re-pressurization; F&AD – Feed & adsorption.

Several key assumptions for developing this simplified 3-step PSA model are as follows:

- A cyclic steady state is a default situation. The end condition of the feed & adsorption step is forced to be identical to the initial condition of the blowdown step.
- The adsorption column is always well-mixed, so that there are no radial nor axial thermal, composition, nor pressure gradients within the bed. The outlet stream has the same composition as the bed composition, except the top product at the adsorption step is assumed to be a desired concentration, 95 mol% of CH_4 in this work.
- Perfect adiabatic condition is assumed for the column wall. No heat transfer with the surrounding environment.
- The specific heat capacity of the gas phase and the adsorbed phase is negligible. They are in thermal equilibrium with the adsorbent at any time with negligible heat transfer resistance.

- Mass transfer resistances are negligible as well. The component in the gas phase is in chemical equilibrium with the adsorbed phase instantaneously. The adsorption separation simulated by the simplified model is a complete equilibrium separation.
- The state of the gas phase is governed by the ideal gas law.

The assumption of a well-mixed bed makes the adsorption column for this model become a “point” without any inner profiles to allow concentration or temperature gradients within the column. This is a bold assumption that will overlook a variety of adsorption features. But considering all the performance indicators we applied in the last chapter are calculated under the same assumption, it instead becomes a good simplification that can avoid most of the complicated calculations in an adsorption simulation model.

For the feed & adsorption step, there are two ways to define the concentration of the top product. Maring in the original work assumed that during the adsorption step, a perfectly flat concentration frontier, dividing the residual gas composition from the re-pressurisation step and the new gas entering via the feed stream, propagated through the bed until breakthrough happened [102]. This was a relatively conservative assumption. Since the top product was of less importance in the application of CO_2/N_2 separation as we discussed before, the quality of the top product was not a concern. The other way was to set the composition of the top product to a desired value of, in our case, 95 mol% of CH_4. Because the simplified model only contained 3 steps without any sophisticated process designs, it was usually hard to achieve a top product with high purity. This assumption forced the adsorption bed to extract a high-quality top product until the breakthrough, therefore, providing an opportunity of horizontal comparison between a simplified model and a rigorous model. The drawback of this assumption is the stream flowrate could be sometimes determined as an unexpected negative value restricted by the law of mass conservation. In such a case, the mild assumption should be applied. Nevertheless, these two options do not affect the calculation results of the desorption step, as our main objective is to obtain the temperature and bed composition at the end of the desorption step, not the adsorption step.

The simulations by the simplified model were run step-wise, and for each major step described in Figure 5.1, further sub-steps were defined based on the pressure change interval. For instance, if the pressure change in the blowdown step was from P_H to P_L, then the sub-step within the blow-down step could be defined as a step with pressure change of $\frac{P_H - P_L}{100}$. Hence, the blow-down step would be finished in 100 steps of calculation.

For each of the sub-steps, mass balance and energy balance equations were used to describe the behaviour of the equilibrium adsorption within the column. By solving these equations, the key process parameters, such as temperature, pressure, bed composition in the gas phase, and the inlet/outlet flowrate could be determined.

The total amount of one component in the column is divided into two groups, the adsorbed group and the group in the gas phase, which is calculated as in Equation 5.1.

$$n_{i,column} = n_{i,solid} + n_{i,gas} \qquad \textbf{Equation 5.1}$$

The solid loading term, $n_{i,solid}$, could be determined by any available adsorption isotherm model. In this work, the extended Langmuir model was used to keep the consistency with the simulations we conducted in Chapter 3 and 4.

The gaseous term, $n_{i,gas}$, was calculated by the ideal gas law. To ensure that the solid term and gas term are additive, they must be evaluated on the same basis. To simplify the calculations and ensure comparable results among different materials, we set the mass of adsorbent to be 1 kg for all conducted simulations. The volume of the column was then determined according to the bulk density of the selected adsorbent. Thus, the bulk density (ρ_{bulk}) of the adsorbent and the voidage (ε) of the column were required for the calculation of the gaseous term as in Equation 4.3. With the availability of the total amount in the column, the overall mass balance around the column for each calculation step was then given by Equation 5.2. The superscript "f" and "0" denote the final and initial states of the column, and the subscript "in" and "out" refer to the inlet and outlet stream. F is the molar flowrate.

$$n_{i,column}^{f} - n_{i,column}^{0} = F_{in}y_{i,in} - F_{out}y_{i,out}$$ **Equation 5.2**

The energy balance of the step could be determined solely by the heat of adsorption caused by the change of adsorption amount as shown in Equation 5.3. Since the heat capacity of the gas phase was assumed to be negligible, the enthalpy brought in/removed by the inlet/outlet gas stream were not considered in this model. The mass of adsorbent (m_S) was set to be 1 kg as stated before. The specific heat capacity of the adsorbent ($c_{P,S}$) in [$J\ kg^{-1}\ K^{-1}$] was required to be specified before the simulation. The isosteric heat of adsorption was calculated based on the Clausius-Clapeyron equation which was also used in Chapter 3 (Equation 3.6).

$$m_S c_{P,S}(T^f - T^0) = \sum_i \Delta H_{i,st}(n_{i,solid}^{f} - n_{i,solid}^{0})$$ **Equation 5.3**

For each major step in the cycle, the corresponding equations and the solution procedure were slightly different. The details of each step are provided in the following sections solved by the programming tool, MATLAB (The Mathworks Inc., USA).

The initial state was that the gas phase in the column was identical to the feed stream while the adsorbed phase was in equilibrium with the feed composition. In the actual PSA process, the temperature of the bed after the adsorption step is higher than the feed stream because of the heat of adsorption. The bed composition is also higher than the feed composition due to the axial composition gradient: at the top end of the column, the gas composition is close to the product composition, while at the bottom end of the column, it is close to the feed composition. Nonetheless, the fully saturated with feed composition at the beginning of the blowdown step is still a reasonable assumption as the final state can return to the same state by sacrificing the quality of the top product. What is more important is that all these conditions were available a priori without running simulations, and the same conditions were also used in the calculation of other performance indicators.

As mentioned before, the major step was solved incrementally by dividing the total pressure change into a discrete number of sub-steps. Therefore, the

pressure for each sub-step was available as a pre-set value. Due to the assumption of instantaneous equilibrium and no transfer resistance, the time needed to achieve the desired pressure change was not considered in this model. Material and energy balance equation sets for one sub-step are listed in Equation 5.4. They were solved simultaneously at the k step by taking the solution of the $(k-1)$ step as known variables. The unknown variables of this equation set are the gas composition y_i^k, the bed temperature T^k, and the outlet stream flowrate F_{BD}^k. Given that the number of the equation is equal to the number of unknown variables, the sub-step is a complementary problem with a unique solution. The total amount the blowdown extraction stream F_{BD} is obtained by taking a sum of the all solved sub-step F_{BD}^k values.

$$n_{CH_4,column}^k - n_{CH_4,column}^{k-1} = 0 - F_{BD}^k y_{CH_4}^k$$

$$n_{CO_2,column}^k - n_{CO_2,column}^{k-1} = 0 - F_{BD}^k y_{CO_2}^k$$

$$m_S c_{P,S}(T^k - T^{k-1}) = \sum_i \Delta H_{i,st}^{k-1}(n_{i,solid}^k - n_{i,solid}^{k-1})$$

Equation 5.4

The process conditions at the desorption step were then accessible when all the sub-steps of the blowdown step were solved. The simulation could have halted here if the purpose of the model were only for determining the desorption conditions. However, because we needed to verify the simplified model by comparing the results with a rigorous simulation model, it was essential to complete the further re-pressurisation and adsorption steps.

In terms of the column operation, the re-pressurisation step just reversed what had been done to the adsorption bed in the blowdown step. The pressure in the column increased from the desorption pressure to the pressure of the feed stream. The same discretization method of the pressure as in the blowdown strep could be carried out. The equations of material and energy balance for the re-pressurisation step are listed in Equation 5.5. The initial conditions were retrieved from the final solution from the blowdown step. The composition of the feed stream y_i^{feed} is a known variable by pre-set value. For each of the sub-step, the

unknown variables are the gas composition at k step y_i^k, the bed temperature T^k and the flowrate of the feed stream F_{RP}^k. This is again a complementary problem with a unique solution. The total amount of the re-pressurisation stream is then the summation of all F_{RP}^k of the sub-steps.

$$n_{CH_4,column}^k - n_{CH_4,column}^{k-1} = F_{RP}^k y_{CH_4}^{feed} - 0$$

$$n_{CO_2,column}^k - n_{CO_2,column}^{k-1} = F_{RP}^k y_{CO_2}^{feed} - 0$$

$$m_S c_{P,S}(T^k - T^{k-1}) = \sum_i \Delta H_{i,st}^{k-1}(n_{i,solid}^k - n_{i,solid}^{k-1})$$

Equation 5.5

The adsorption step in this simplified model is different from the other two steps. It was operated isobarically with definite start and final conditions: the start conditions were determined by the calculation of the re-pressurisation step; the final conditions were fully-saturated with feed stream by assumptions, which were also the overall initial conditions of the PSA cycle. As both start and end states were known, the amount of the feed required and the top product obtained in this step were the only variables to be solved. Mass balance equations are listed in Equation 5.6. In the equations, feed stream flow amount F_{FD} and the top product flow amount F_{TP} are the unknown variables to be solved.

$$n_{CH_4,column}^f - n_{CH_4,column}^0 = F_{FD} y_{CH_4}^{feed} - F_{TP} y_{CH_4}^{top}$$

$$n_{CO_2,column}^f - n_{CO_2,column}^0 = F_{FD} y_{CO_2}^{feed} - F_{TP} y_{CO_2}^{top}$$

Equation 5.6

Upon finishing the calculation of the adsorption step, all significant process parameters (temperatures, pressures, compositions) of the PSA process have been determined. Our first objective of this simplified model, fetching the temperature and composition at the desorption steps, was also accomplished. The results could be directly used in the adiabatic column working selectivity, the novel adsorbent performance indicator we proposed in the last chapter (Equation 5.7).

$$\beta_{column} = \frac{n_{CO_2,column}(P_{ad}, T_{ad}, y_{CO_2,ad}) - n_{CO_2,column}(P_{de}, T_{de}, y_{CO_2,de})}{n_{CH_4,column}(P_{ad}, T_{ad}, y_{CH_4,ad}) - n_{CH_4,column}(P_{de}, T_{de}, y_{CH_4,de})}$$

Equation 5.7

In addition, as all process variables of the PSA process were accessible with this simplified model, the regular performance evaluation method could be employed similarly as the rigorous simulation. The purity of the raffinate product from the simplified model was specified to be 95 mol% of CH_4. Hence, it was possible to assess the performance of the adsorbent with a single parameter, the recovery of the light component CH_4. The recovery of CH_4 was defined as the amount of recovered CH_4 in the top product compared with the total feed CH_4 in the feed stream and the re-pressurisation stream (Equation 5.8).

$$\text{Recovery } of\ CH_4 = \frac{F_{TP} \cdot y_{CH_4}^{top}}{(F_{RP} + F_{FD}) \cdot y_{CH_4}^{feed}} \qquad \textbf{Equation 5.8}$$

It is emphasised that the simplified model we developed here is not to provide quantitative agreement with the rigorous simulations and practical experiments. It aims to be able to replicate trends and relative rankings among different adsorbents, and what is important is to provide a rapid and reliable way to acquire the desorption information for the adsorbent screening.

To validate the ability of the model to mimic the desorption conditions, we made a comparison with an adiabatic equilibrium model developed by Kumar to study the blowdown step of the PSA process [103]. In this reference, an adsorption column filled with BPL activated carbon was saturated with equimolar CO_2/N_2 gas mixture at an initial pressure of 15 bar. The pressure in the column was then released to a lower level of 1 bar. The changing of the bed composition and the temperature in the column were recorded to study the blowdown step in the PSA cycle operation. Using the column parameters, adsorption properties of the adsorbent, and the stream information available in the literature, we were able to repeat the same blowdown step by the simplified model we developed. The resulting bed composition and temperature by the model and from the literature are shown in Figure 5.2, and both profiles showed perfect matches as the pressure in the bed decreased to the lowest level. This is strong evidence that proves the validity of the simplified model we developed in this work for the case in which no profiles are present in the bed.

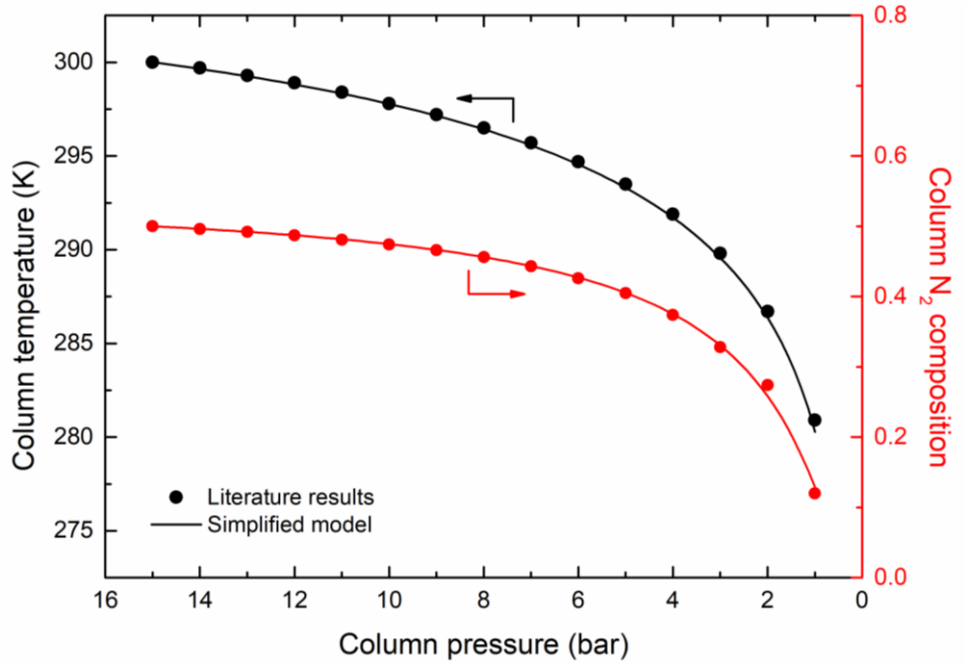

Figure 5.2. Comparison between the results from literature and the simplified model developed in this work

5.1.2 5-step PSA model

A 5-step PSA model including the pressure equalization steps was developed based on the 3-step model as shown in Figure 5.3. The role of the pressure equalization step is critical to practical PSA processes. In Chapter 4, we have demonstrated how the adsorbates remaining in the gas phase could significantly decrease the overall selectivity of the adsorbent at high pressure. To avoid such performance loss in practical processes, the method of pressure equalization is generally applied to reduce the total amount of the gas molecules in the adsorption column through decreasing the pressure before the desorption step in practical adsorption application [84]. The results proved that the pressure equalization step could effectively enhance the recovery of the light product and the purity of the heavy product, at a cost of lowering the throughput per column and increased capital investment for the extra columns and control instrumentations. For the industrial applications when the benefits gained from increasing the recovery of precious compounds exceed other cost considerations, such as H_2 purification and natural sweetening, pressure equalizations are commonly used. Therefore, it is necessary to include the pressure equalization into our model to examine its influence.

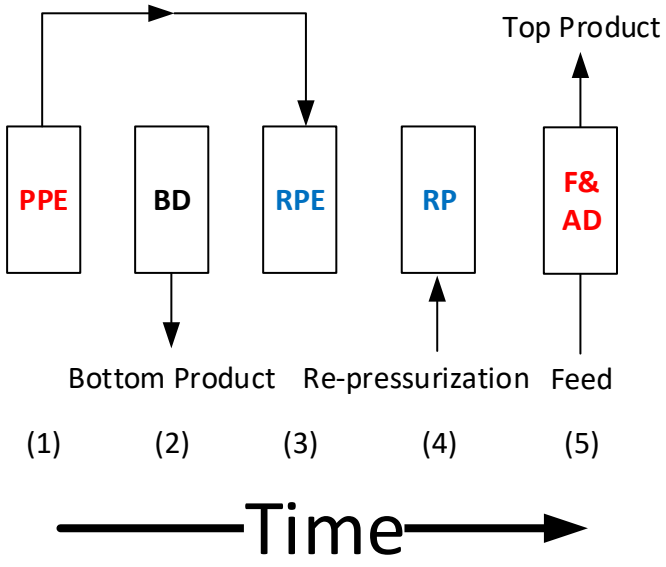

Figure 5.3. Schematic of the 5-step PSA cycle applied in the advanced model. PPE – Providing pressure equalization; BD – Blowdown; RPE – Receiving pressure equalization; RP – Re-pressurization; F&AD – Feed & adsorption.

The 5-step model was built on the same assumptions of the 3-step model. The calculation procedures of the individual major step followed the same principle of discretising the total pressure change into many sub-steps and solving the mass balance and energy balance equation set of each sub-step.

The introduction of the pressure equalization steps did add complexity for solving the whole process. The ultimate target of this model was to find the desorption conditions, which implied the initial conditions of step 3, i.e. receiving pressure equalization step, were unspecified. Without the presence of the initial conditions of step 3, the bed interaction behaviour between step 1 and step 3 was impossible to resolve as well. This further made initial conditions of the blowdown step unattainable, and consequently so were the desorption conditions. An iteration process as shown in Figure 5.4 was employed to simultaneously solve steps 1 to 3.

The conditions at the end of the blowdown step as well as the start of the receiving pressure equalization steps were guessed initially. The pressure equalization interaction between step 1 and step 3 then can be solved simultaneously by carrying out mass balances and energy balances over the individual adsorption column. The bed pressure of step 1 was set to be

decreasing step-wise. As the overall pressure change was an unknown value, the length of the pressure changing step was manually adjusted to an arbitrary size of 0.3 bar to ensure the total number of the steps was approximately 100. Smaller step sizes could enhance the accuracy of the iterative calculation, but CPU-hour required would increase exponentially. The pressure rises of the adsorption bed of step 3 was not pre-specified by discretization but determined by working out the mass balance equations.

$$n^{k}_{CH_4,column\ 1} - n^{k-1}_{CH_4,column\ 1} = 0 - F^{k}_{PE} y^{k}_{CH_4,column\ 1}$$

$$n^{k}_{CO_2,column\ 1} - n^{k-1}_{CO_2,column\ 1} = 0 - F^{k}_{PE} y^{k}_{CO_2,column\ 1}$$

$$m_S c_{P,S}\left(T^{k}_{column\ 1} - T^{k-1}_{column\ 1}\right) = \sum_i \Delta H^{k-1}_{i,st}\left(n^{k}_{i,solid\ 1} - n^{k-1}_{i,solid\ 1}\right)$$

Equation 5.9

$$n^{k}_{CH_4,column\ 3} - n^{k-1}_{CH_4,column\ 3} = F^{k}_{PE} y^{k}_{CH_4,column\ 1} - 0$$

$$n^{k}_{CO_2,column\ 3} - n^{k-1}_{CO_2,column\ 3} = F^{k}_{PE} y^{k}_{CO_2,column\ 1} - 0$$

$$m_S c_{P,S}\left(T^{k}_{column\ 3} - T^{k-1}_{column\ 3}\right) = \sum_i \Delta H^{k-1}_{i,st}\left(n^{k}_{i,solid\ 3} - n^{k-1}_{i,solid\ 3}\right)$$

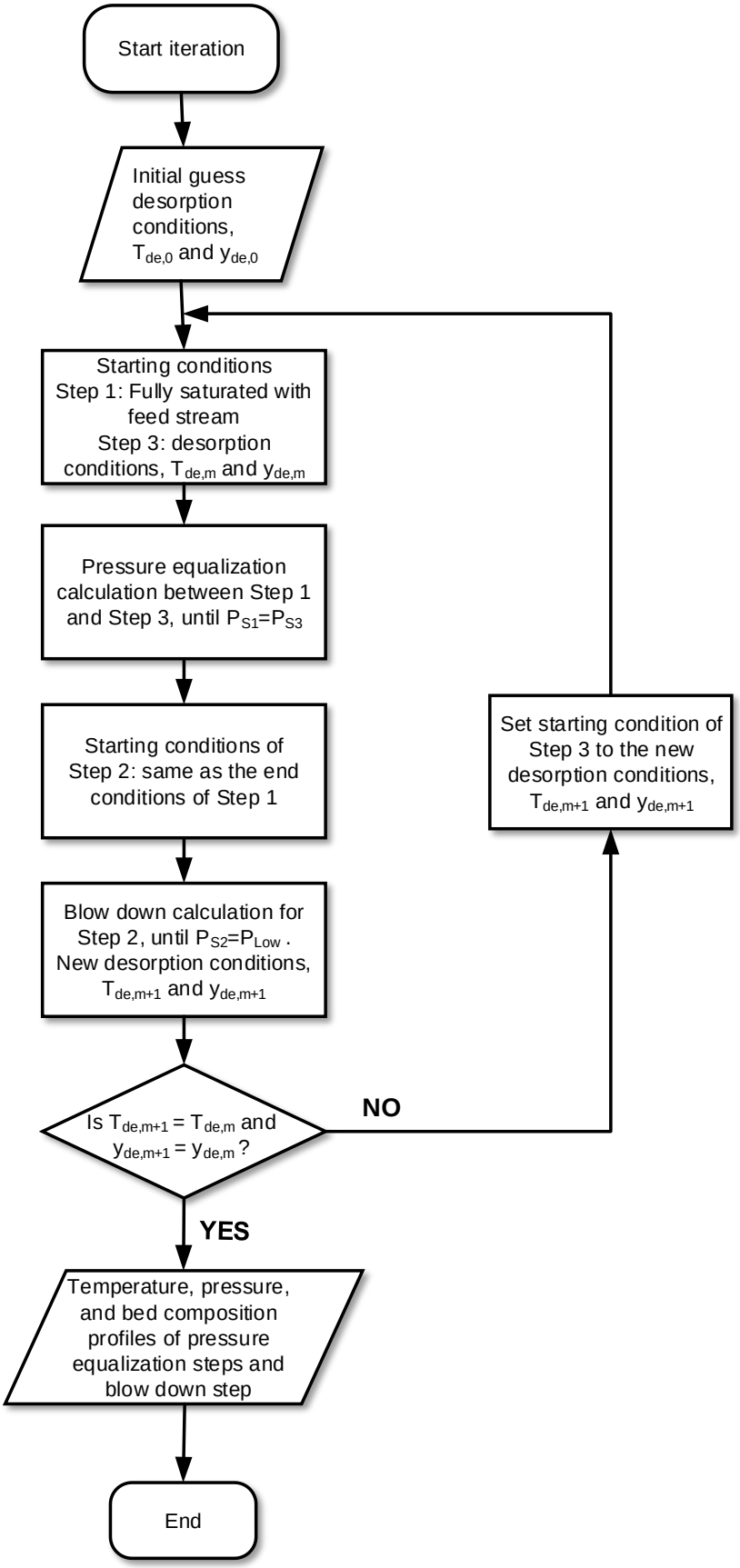

Figure 5.4. **Flow chart of the iteration process for the pressure equalization steps and the blowdown step in the 5-step PSA model**

The mass and energy balance equations for one sub-step of the pressure equalization steps are listed in Equation 5.9. The six variables to be determined by these six equations were the bed temperature of step 1 and 3 ($T^k_{column\,1}$ and $T^k_{column\,3}$), the bed composition of step 1 and step 3 ($y^k_{CH_4,column\,1}$ and $y^k_{CH_4,column\,3}$), the pressure of step 3 ($P^k_{column\,3}$) and the interaction stream flowrate (F^k_{PE}). As the pressure of the column in step 1 ($P^k_{column\,1}$) reduced step-wise to a level lower than the calculated pressure of step 3 ($P^k_{column\,3}$), the pressure equalization between two beds was reached, and the solutions of the sub-step just before the pressure crossover occurred were recorded temporarily as the end conditions of steps 1 and 3.

The starting conditions of the blowdown step were then adapted as the end condition of step 1, and the same method as described in Section **Error! R eference source not found.**was used to determine the desorption conditions. However, considering this result was acquired by utilizing the initial guess of the desorption condition at the very beginning of the procedure, a verification must be done to check if the calculated solution converged to the initial guess. If they deviated from each other, the calculated solution would be used as a new initial guess for the next round of procedure to re-calculate the pressure equalization steps and the blowdown step. Once an agreement between the initial guess and the calculated solution was achieved within a pre-set tolerance, all solutions of the calculation for pressure equalization steps and the blowdown step were recorded as the final acceptable results.

The re-pressurization step and the adsorption step were then solved in the same way as the 3-step PSA model to accomplish the whole calculation procedure of the 5-step PSA model.

5.2 Materials and methods

To check the feasibility of the newly developed simplified models in terms of screening and evaluating adsorbents, those adsorbents used in Chapter 4, i.e. HSZ-320HOA, HSZ-350HUA, HSZ-385HUA, HSZ-390HUA, CBV-760, CBV-780, Sorbead® WS, UiO-66 and UiO-67, were employed in this chapter as well. Their pure component adsorption isotherms were modeled by the single-site Langmuir

model (Equation 2.3), and the mixture adsorption behaviour was then described by the extended Langmuir model (Equation 2.7). The fitting parameters of the Langmuir adsorption model for all selected materials are available in Table 4.4.

To compare the results between the simplified model and the rigorous model, the same process parameters, such as feed composition, pressure, temperature, desorption pressure and product specification, were applied as what we had simulated in Chapter 3 and Chapter 4. The detailed configuration of the simulation can be found in Section 3.2.4 and Section 4.3.3.

5.3 Results and discussion

5.3.1 Process parameters in the desorption steps

The temperature and bed composition at the end of the desorption steps by Aspen Adsorption for all selected adsorbents are listed in Table 5.1.

Table 5.1. Temperature and bed composition at desorption steps by Aspen Adsorption

Adsorbent	*Desorption Temperature (K)*	*Bed Composition (CH_4 mol%)*
HSZ-320HOA	281.93	35.25
HSZ-350HUA	274.87	36.75
CBV-760	275.25	36.69
CBV-780	276.54	31.48
HSZ-385HUA	276.44	32.60
HSZ-390HUA	275.60	37.90
Sorbead® WS	283.37	21.10
UiO-66	271.75	53.30
UiO-67	266.69	35.78

The desorption temperature and the bed composition obtained by the simplified models were compared with the results from the rigorous model, illustrated in Figure 5.5 and Figure 5.6.

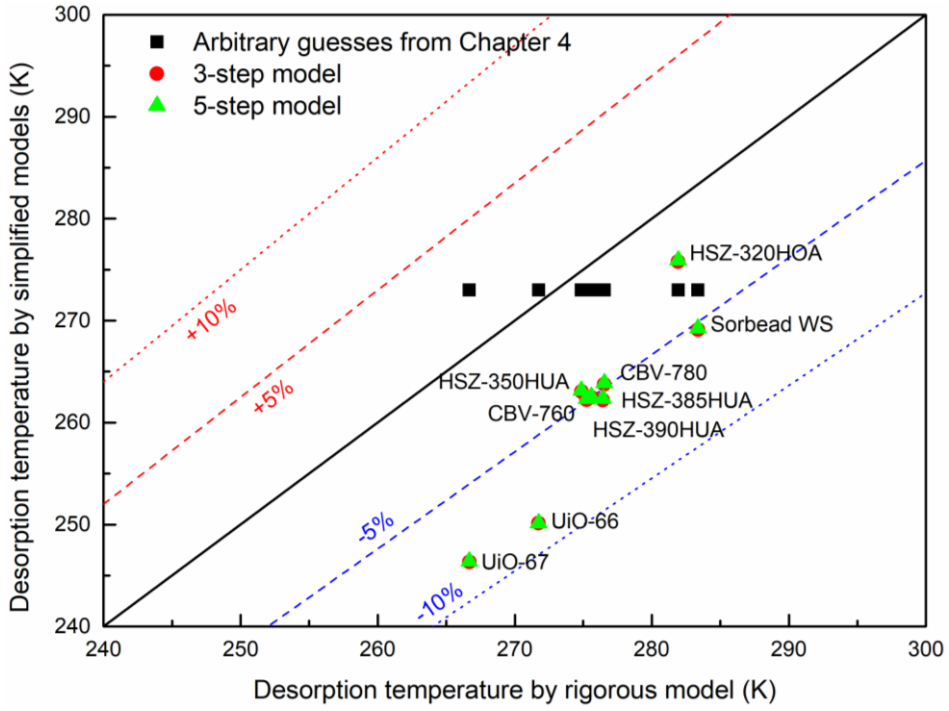

Figure 5.5. **Bed temperature at the end of the desorption step**

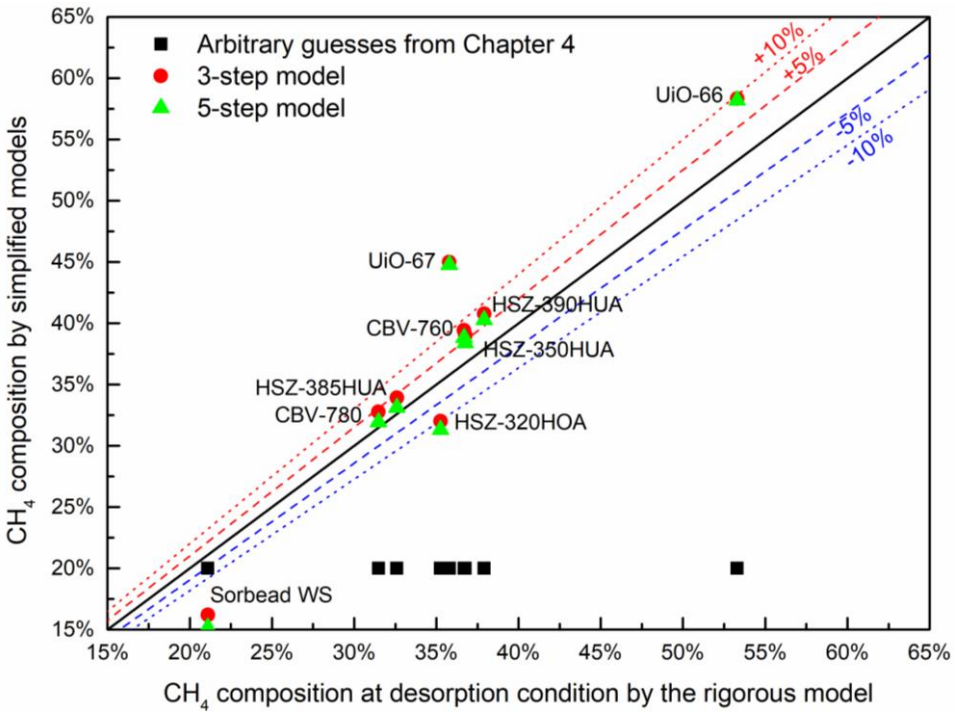

Figure 5.6. **Bed composition of CH_4 at the end of the desorption step**

It is interesting to observe that both key process parameters obtained by the 3-step model and the 5-step model are almost identical. It is largely due to the assumption of well-mixed in the adsorption column. In the 5-step model, the combined effect of the providing pressure equalization step (Step 1) and the

blowdown step (Step 2) is that the pressure in the adsorption bed decreases from the feed pressure to the desorption pressure. Because there is no difference between the outlet stream exits from the adsorption column from the top port or the bottom port since no composition and temperature gradients are present, a fixed amount of pressure drop from the feed level to the desorption level will have the same impact in the both 5-step and 3-step model. Hence, the desorption temperature and the composition from both simplified models are identical. However, as in the rigorous model the composition gradient plays an important role in the separations, pressure decreasing via different routes does lead to the variation of the process parameters. And this variation could be a major reason for the deviation of the results from the simplified model and the rigorous model as shown in the figures. Although the assumption of a well-mixed bed causes us to miss some key adsorption features, it allows us to obtain the same results using a simpler model (3-step) instead of a complicated model (5-step) to further save the computation time.

The desorption temperatures predicted by the simplified model are all lower than those obtained by the rigorous model. This is partially due to the negligence of the heat capacity of the gas component as well as the adsorbed phase due to the assumption of the simplified model. The results from the simplified model are still reasonable within 10% of the rigorous model. The deviation for UiO-67 and Sorbead® WS of the bed composition at the end of the desorption step between the two methods is larger than 10%, while others are in relatively good agreements.

Nevertheless, as we stated before, the simplified models are not intended to reach a perfect quantitative agreement with the rigorous model. The relative ranking between adsorbents in terms of the adsorption performance is more significant.

5.3.2 Adiabatic column working selectivity

With the properties of the feed stream as well as the temperature and bed composition at the desorption step, the adiabatic column working selectivity of each selected adsorbent are calculated and listed in Table 5.2. The CH_4 recovery from the simulations by Aspen Adsorption in the last column can be regarded as

the actual performance of the adsorbents. The performance evaluated by other methods should be compared with these results. We format the table in the same pattern as Table 4.6. The maximal numbers of one indicator are shaded as navy blue and the minimal numbers are shaded as red, while the median is left without shading. Other numbers between the maximum, minimum, and median are coloured proportionally.

Table 5.2. Adiabatic column working selectivity calculated using desorption conditions from different methods

Adsorbent	*Adiabatic column working selectivity*			*CH_4 recovery from Aspen Adsorption**
	Arbitrarily guessed conditions in Chapter 4	*Desorption conditions from 3-step model*	*Desorption conditions from 5-step model*	
HSZ-320HOA	0.662	0.636	0.632	0.613
HSZ-350HUA	0.650	0.606	0.602	0.585
CBV-760	0.659	0.587	0.584	0.562
CBV-780	0.723	0.624	0.620	0.608
HSZ-385HUA	0.717	0.617	0.613	0.606
HSZ-390HUA	0.627	0.596	0.593	0.570
Sorbead® WS	0.848	**0.776**	**0.772**	**0.711**
UiO-66	0.484	**0.482**	**0.481**	**0.334**
UiO-67	0.756	0.585	0.582	0.567

* Process simulation's configuration are described in Table 4.3.

The first column of the table is the adiabatic column working selectivity calculated using the arbitrary guessed desorption conditions, which are 273 K and 20 mol% of CH_4. In Chapter 4, we have compared these results with other adsorbent performance indicators (Table 4.6), and it displayed that only the adiabatic column working selectivity could successfully predict the best and the worst adsorbents.

The comparison between the presumed conditions and the actual desorption conditions obtained by the rigorous model are demonstrated in Figure 5.5 and Figure 5.6. The deviations were large, especially for the case of the bed composition. But still, the novel performance indicator could predict a rough rank among the selected adsorbents under such conditions. It might be because the difference between selected adsorbents were so large that the performance divergence exceeded the impact of the error induced by the uncorrected

desorption conditions.

When the desorption conditions are obtained by simplified models, the adiabatic column working selectivity can perfectly predict the performance ranking as the rigorous model did. As can be seen that not only the best and the worst adsorbents whose structures are largely different can be ranked correctly, those zeolites with similar adsorption properties can also be assigned to the corrected ranking. This result proved the feasibility of the simplified model as the method of acquiring the temperature and the bed composition at the desorption step. It is also a strong supporter of the validity of the adiabatic column working selectivity as an adsorbent screening tool.

5.3.3 CH_4 recovery directly obtained from the simplified model

As the simplified models have determined all key process parameters during the calculation process, the recovery of CH_4 of the adsorption process can be directly calculated via Equation 5.8, and the results are listed in Table 5.3.

The relative order of the CH_4 recovery by both simplified models match the ranking obtained by the Aspen Adsorption simulation. This result means that the simplified models are capable to screen multiple adsorbents without employing other performance indicators. Besides, it is observed that the CH_4 recovery is in an increasing trend from the 3-step model, 5-step model to the Aspen Adsorption simulation which is a 9-step model with three pressure equalization steps. This is as expected that with more pressure equalization steps in the process, the recovery of the CH_4 can be enhanced in this application.

Table 5.3. **CH_4 recovery obtained by different simulation models**

Adsorbent	*CH_4 recovery*		
	3-step model	*5-step model*	*Aspen adsorption**
HSZ-320HOA	35.38%	52.11%	61.30%
HSZ-350HUA	31.95%	47.39%	58.52%
CBV-760	29.38%	44.47%	56.20%
CBV-780	33.90%	50.32%	60.84%
HSZ-385HUA	33.66%	49.92%	60.58%
HSZ-390HUA	30.62%	45.54%	57.04%
Sorbead® WS	47.90%	65.74%	71.12%
UiO-66	12.21%	20.38%	33.43%
UiO-67	29.02%	42.96%	56.74%

* Process simulation's configuration are described in Table 4.3.

It is worth noting that the relative performance trends obtained by the calculation of adiabatic column working selectivity are as same as the ranking of the CH_4 recovery. It is important to note that the calculation method of the CH_4 recovery and the adiabatic column working selectivity are completely different from each other. The CH_4 recovery is determined by process variables, such as the flowrate and the average concentration of the feed and product streams, while the adiabatic column working selectivity is mostly based on the material adsorption properties, namely the adsorption isotherms, with a few process conditions. Their consistent adsorbent screening results implies that the adiabatic column working selectivity does capture the essential features of the adsorption process.

It is well known from previous work that changing the adsorption isotherms of the adsorbents could affect the performance of the adsorption process. The exact relationship between the adsorption isotherms and the process performance, however, were not clear. The ideal selectivity, working selectivity, and various lumped indicators were actual attempts by researchers trying to describe the connection between the adsorbent properties with the process performance. But their results, more or less, deviated from the rigorous simulation results as we have shown in Chapter 4. To the best knowledge of the author, the adiabatic column working selectivity proposed in this work is the first adsorbent performance indicator that can precisely predict a same ranking as the results of rigorous process simulations.

5.4 Summary

In this chapter, to resolve the issue of finding the appropriate desorption temperature and bed composition encountered when applying the adiabatic column working selectivity to screen adsorbents, two simplified simulation models were developed. Both models were under the same assumptions which allowed one to carry out the adsorption process without considering the concentration and temperature gradient within the adsorption bed. Although the desorption temperature and the bed composition determined by the simplified model slightly deviated from the rigorous model, the subsequent calculation of the adiabatic column working selectivity using the model derived desorption information could perfectly match the results of the rigorous model. Besides, the

simplified models themselves could directly determine the adsorbent performance ranking without employing any other performance indicators. And the fact that the adiabatic column working selectivity had the same trend of the process performance variables, such as the recovery of one component, proved that the novel proposed performance indicator could act as a fairly reliable connection between the material property and the process variables.

CHAPTER 6

CO_2 CAPTURE FROM NATURAL GAS BY PRESSURE SWING ADSORPTION AT THE CO2CRC OTWAY DEMONSTRATION CARBON CAPTURE PLANT

In previous chapters, for the aim of removing CO_2 from natural gas at pressure by adsorption technology, we have characterized seven potential adsorbents (zeolites and silica gel). Then, we employed a novel adsorbent performance indicator, as well as newly developed simplified simulation models, to evaluate the measured adsorbent performance under specific working conditions, and found that compared with the zeolites, the silica gel, Sorbead® WS with linear isotherms and lower adsorption capacities, was the best candidate for the application of CO_2 removal from natural gas. In this chapter, we report on the application of Sorbead® WS to a demonstration adsorption plant as the adsorbent for experimental operations of removing CO_2 from the high-pressure natural gas mixture. The actual process results are compared to the simulation models.

6.1 Experiments, Materials and Methods

6.1.1 CO2CRC Otway CO_2 capture rig and PSA apparatus

The CO_2 and methane mixtures produced by the geological structures underground at the Otway Basin, Victoria is a suitable mixture gas source for long term testing of different natural gas sweetening processes at scale, due to the large amount of available gas (over 400,000 tonnes). The gas available from the well at the Otway site contains approximately 79%CO_2 and 21% CH_4 with trace quantities of higher hydrocarbons. CO2CRC Ltd., an Australia's leading carbon capture and storage (CCS) research organisation, has established a CO_2 capture rig at its Otway National Research Facility using the local stored gas to demonstrate CO_2 capture from natural gas using adsorption and membrane technologies. In addition to directly using the geologically trapped gas, a gas mixing and feeding system with deliberate designs can blend gases such as CO2 and natural gas from cylinders into the extraction gas from underground, so that it can provide a feed gas to the capture rig with any compositions of CO_2

balanced with methane and other impurities like heavy hydrocarbons, N_2 and H_2S, spanning the range of most naturally occurring natural gas wells. It is helpful to examine the flexibility and applicability of specific adsorbents and designs of the PSA process to various gas sources in different applications. Figure 6.2 displays a general appearance of the CO_2 capture rig. Most of the auxiliary instrumentals observed in the picture belong to the feed control system.

Figure 6.1. Location of the CO2CRC Otway Research Facility. Retrieved from http://www.co2crc.com.au/wp-content/uploads/2017/05/C02CRC_Map-and-diagrams-1-003.jpg, 10th May, 2020

Figure 6.2. **A general appearance of CO2CRC's Otway CO_2 capture rig. Retrieved from http://www.co2crc.com.au/wp-content/uploads/2016/10/TH_20161011_362.jpg, 10th May, 2020**

The adsorption section of the capture rig has a two-bed PSA arrangement. A picture and process flow scheme of the PSA section is shown in Figure 6.3. Due to the limitation of the footage and the complexity of the design, both of the adsorption beds are connected to a buffer tank (not shown in the photo) to enable sophisticated adsorption cycle designs to be executed by using fewer numbers of adsorption columns. In addition, the adsorption columns are covered by heating jackets along with the insulation materials. The purpose of these heatproof measures is to maintain a relatively stable operation condition of the adsorption column considering the CO_2 capture rig is installed outdoors. However, it makes the PSA process close to an isothermal process instead of a more practical adiabatic process in industrial applications. The geometric details of the fixed-bed and the buffer tank are listed in Table 6.1.

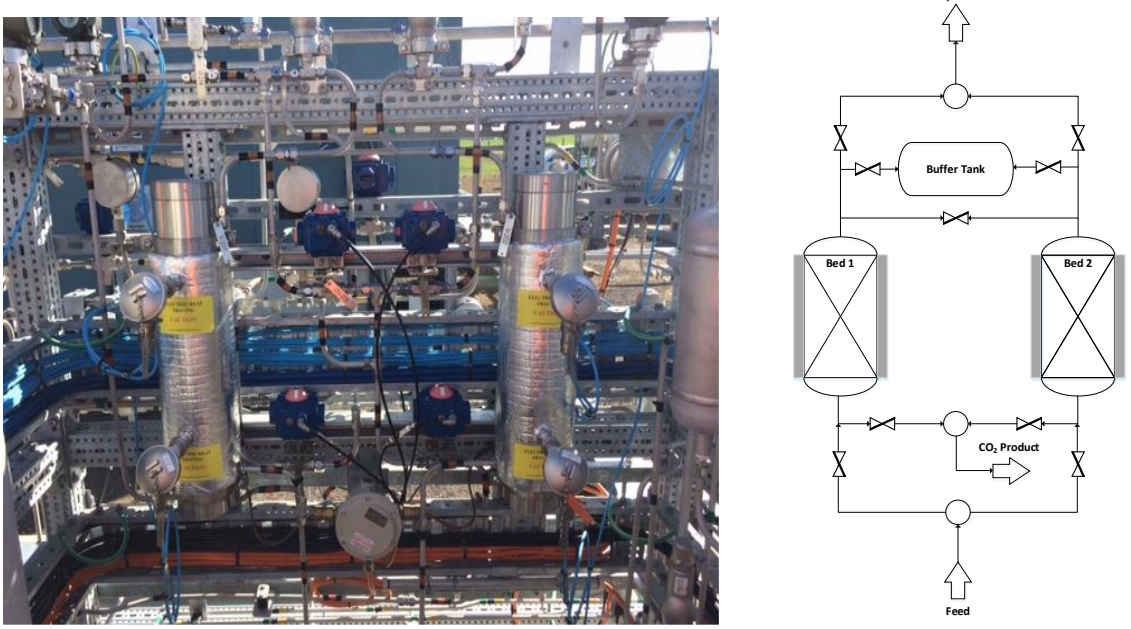

Figure 6.3. **Scheme of the PSA process in Otway site**

Table 6.1. **Geometric details of the column and buffer tank of the adsorption plant**

Properties	*Values*
Adsorption Column radius (mm)	80
Adsorption Column length (mm)	600
Adsorption Column wall thickness (mm)	4.5
Volume of the buffer tank (L)	15

A 10-step cycle including adsorption, pressure equalization with the buffer tank, pressure equalization between two beds, and desorption was implemented, as shown in the schedule Table 6.2. Note that this cycle does not follow the principle of continuous feed as it can be seen that the gas feed is activated only at step 1 and step 6. The same occurs in the desorption operation. This is a compromised solution for the conflict of sophisticated cycle design and the limited number of adsorption columns available. With the insertion of the buffer tank pressure equalization, a further cleaning of the gas phase before the desorption step can be achieved which could enhance the overall performance of the process.

Table 6.2. **Cyclic configuration of the PSA cycle**

	Steps									
	1	**2**	**3**	**4**	**5**	**6**	**7**	**8**	**9**	**10**
Bed 1	AD*↑	PPE BT↑	PPE↑	DE↓				RPE↓	RPE BT↓	RP↑
Bed 2	DE↓		RPE↓	RPE BT↓	RP↑	AD↑	PPE BT↑	PPE↑	DE↓	

***AD – Adsorption, PE BT – Pressure equalization with a buffer tank, PE – Pressure equalization with the other bed, DE – Desorption by blowing down, RP – Re-pressurization by feed. The arrow direction refers to the gas stream flowing direction.**

- **Step 1** – Feed mixture gas enters bed 1 co-currently. CO_2 is selectively adsorbed to the adsorbent and rich CH_4 gas is collected from the top port of bed 1. Bed 2 is under counter-current desorption. Rich CO_2 product exits from the bottom of bed 2.
- **Step 2** – Connect the bed 1 to the buffer tank for a co-current pressure equalization, while bed 2 continues for the desorption process.
- **Step 3** – Connect bed 1 and bed 2 for an inter-column pressure equalization.
- **Step 4** – Bed 1 begins desorption and collect a CO_2-enriched gas stream. Bed 2 is pressurized by the buffer tank.
- **Step 5** – Continue for desorption at bed 1. Bed 2 is pressurized by the feed gas mixture.
- **Step 6 to 10** – Repeat of steps 1 to 5 with the beds switched.

To avoid CH_4 gas emission to the atmosphere, the exiting gas with enriched CH_4 in the top stream and the desorbed gas with enriched CO_2 in the downstream line were combined and passed to a thermal oxidizer.

6.1.2 Adsorbent

As mentioned, the adsorbent used in this study was Sorbead WS, as both our new proposed performance indicator and the process simulations suggested that it was the best adsorbent among a series of selected materials for the application of CO_2 removal from natural gas at pressure (details in Chapter 3, 4 and 5 of this work).

Table 6.3. Textural properties of Sorbead® WS

Properties	*Value*	
Chemical composition	SiO_2	97 wt.%
	Al_2O_3	3 wt.%
B.E.T. surface area (m^2/g)	650	
Pore volume (cm^3/g)	0.45	

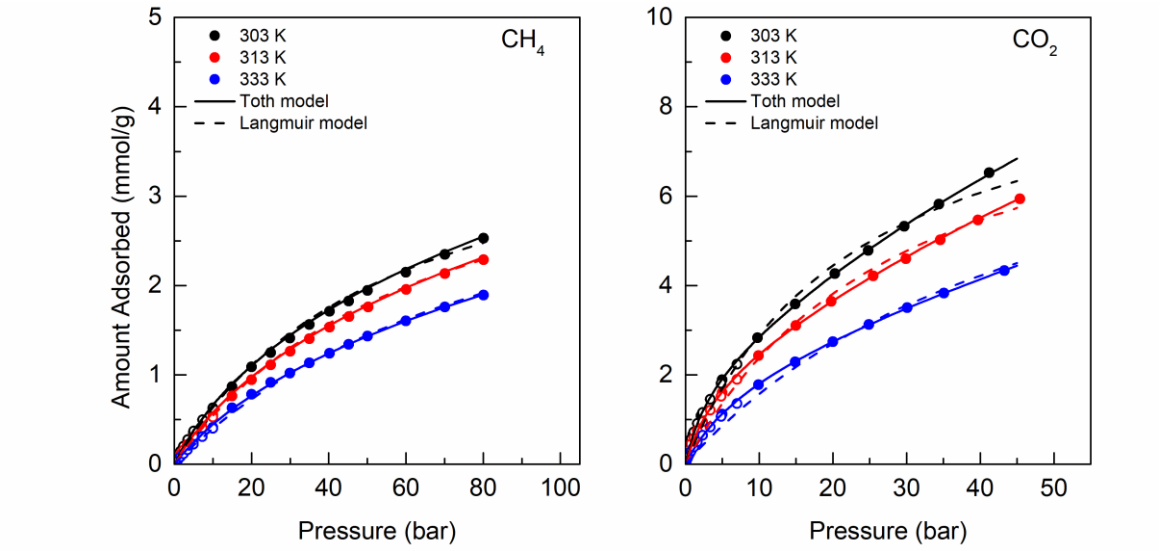

Figure 6.4. Measured isotherms of CH_4 and CO_2 on Sorbead® WS at 303 K, 313 K and 333 K.

The textural properties (surface area, pore volume and composition) of the Sorbead WS were provided by the vendor in Table 6.3. The adsorption Isotherm of CO_2 and CH_4 on Sorbead WS at three temperatures, 303 K, 313 K, 333 K, were measured on a static volumetric analyser ASAP 2050 (Micromeritics Instrument Corporation, USA) in the pressure range of 0 to 10 bar, and on a magnetic suspension balance system (Rubotherm GmbH, Germany) in the pressure range of 0 to 80 bar. The details of the measurement method were described in Section 3.2.3. The measured isotherms are reported in Chapter 3. Here in Figure 6.4, the adsorption isotherms in the intermediate pressure range measured by ASAP 2050 via volumetric method (shown as open circles) and the ones in the high-pressure range measured by Rubotherm via gravimetric method (shown as solid circles) are combined. The results adsorption isotherms were fitted by the Langmuir model (Equation 2.3) and Toth model (Equation 2.6),

respectively, and the fitting parameters, as well as the residual sum of squares (RSS, Equation 3.9) to describe the fitting quality, are listed in Table 6.4.

Table 6.4. Isotherm fitting parameters of Sorbead® WS by Toth and Langmuir model (also reported in Table 3.10)

Model	*Gas*	$n_i^* \ (mol \cdot kg^{-1})$	$b_i \times 10^5 \ (bar^{-1})$	$Q_i \ (kJ \cdot mol^{-1})$	t_i	*RSS*
Toth	CH_4	9.72 ± 0.68	3.68 ± 0.19	14.50 ± 0.12	0.53 ± 0.02	0.004
	CO_2	10.02 ± 0.01	6.84 ± 0.31	22.26 ± 1.23	0.89 ± 0.04	0.775
Langmuir	CH_4	4.21 ± 0.07	5.25 ± 0.68	14.71 ± 0.35	N/A	0.034
	CO_2	9.61 ± 0.40	0.77 ± 0.36	21.76 ± 1.29	N/A	0.884

6.1.3 Process simulation

In Chapter 5, we have developed two simplified PSA models to provide desorption conditions and rough estimates of the recovery of key components. We have verified the newly developed models with simulated results from literature and with another rigorous model we developed in a commercial simulation tool. In this chapter, the process operation results obtained by the PSA process of the Otway CO_2 capture rig were used as the practical process results to compare with the simulation results of the 5-step simplified model we developed, to further check the model's validity. The cycle configuration of the 5-step model is shown in Figure 6.5. The model development was described in detail in Section 5.2.2.

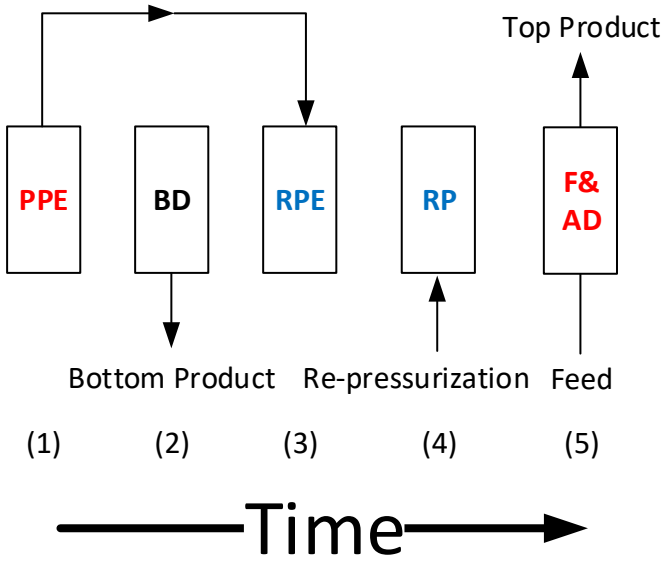

Figure 6.5. Schematic of the 5-step PSA cycle applied in the advanced model. PPE – Providing pressure equalization; BD – Blowdown; RPE – Receiving pressure equalization; RP – Re-pressurization; F&AD – Feed & adsorption. (Also reported in Figure 5.3)

We have noticed the difference between the simplified model and the PSA process of the Otway CO_2 capture rig, that the additional couple of pressure equalization steps are not included in the simulation. But when reviewing the pressure equalization steps between the adsorption column and the buffer tank, we found that the gas capacity of the empty buffer tank without packed adsorbents was undersized, so that it could not provide the excepted pressure decreasing effect of the adsorption column. The overall pressure evolution profile in the Otway PSA process, as a result, was similar to that of the 5-step model.

6.2 Results and discussions

6.2.1 PSA results

Separation experiments were carried out on the PSA plant periodically from May 2017 to May 2019 under various operational conditions. Table 6.5 shows representative process results along with their operating conditions. The CO_2 concentrations in the feed gas stream were in a wide range from 28% to 78% trying to mimic those targeted in sour natural gas sources with high CO_2 contents.

In the first phase of operations (case No. 1 to 8 in Table 6.5), the overall stream flowrates were restricted to very low levels because the piping was undersized and did not allow design flow rates. To deliver enough gas components, the adsorption time had to be set to very large values, such as 1500 seconds, which

substantially reduced the plant's throughput in a unit period. Undeniably, low productivities are not acceptable in industrial applications, but as for this demonstrative PSA plant, showing the technical feasibility of PSA is of the top priority. The economic issues of concern and further process optimizations would be in the second stage.

The relatively small size of the pipes also negatively affected the desorption process. The desorption pressure could not reach the expected value (1 atm) in the given desorption time. As the guiding concept of the PSA process is to make use of the pressure difference between the feed and the desorption condition as the driving force for the separation, higher desorption pressures inevitably lessen the anticipated working capacity of each component, and consequently, weaken the selectivity of the adsorbent. As can be seen, the process results of the first phase were not ideal, however, they demonstrated that separation could be achieved. Minor separation between CO_2 and CH_4 could be observed, but it was far from the expectation.

Process modifications were done to the PSA plant to fix these known issues. During the second phase of operations (case No. 10 to 14 in Table 6.5), the stream flowrate and the desorption pressure could be adjusted to the desired levels.

Case 10 displayed the potential of extracting high-concentration CO_2 from the gas mixture using the PSA process by amplifying the feed flowrate. Both purity and recovery of CO_2 could be very high, although such a process is not fit for the purpose of this work.

Case 11 to 13 were the desired processes for the application of CO_2 removal from natural gas. The purity of methane product was enhanced to a level meeting the specification of the pipeline natural gas, higher than 97 mol%, via one stage of the PSA process. The recovery of methane was in a range of around 60-70%, which might be a concern when considering the economic factors. An attempt to boost the recovery of CH_4 by increasing the total amount of feed gas was done as the Case 14, but the purity of the methane dropped to an unsatisfying value. These results implied that we have reached the upper limit of the performance by current process configurations. To further improve the process performance,

it needs to turn to either switching to an adsorbent with better selectivity than Sorbead® WS or changing to a process with a more sophisticated cycle design.

In a summary of the operational results, both assessment of the adsorbent and the process were completed in the PSA demonstration. Sorbead® WS exhibited adequate adsorption selectivity of CO_2 over CH_4 at pressure, even in the cases when the process was not in a perfect design. The technical feasibility of using PSA to remove CO_2 from natural gas were also demonstrated as high purity (≥95 mol%) methane product with acceptable recovery (≥85%, preferred ≥90%) were obtained after solving the design issues.

Table 6.5. Representative experimental results of the demonstrative plant with Sorbead® WS as the adsorbent

Case No.	Date	Feed composition	Feed pressure	Adsorption time	Feed flowrate	Average bed temperature	Desorption pressure	CH_4 purity	CO_2 purity	CH_4 recovery
		$(CO_2\ mol\%)$	(bar)	(sec)	$(std.L/\min)$	(℃)	(bar)	$(mol\%)$	$(mol\%)$	(%)
1	**11-May-17**	30	30	1500	7.4	45	3.5	83	52	75
2	**24-May-17**	28	30	1500	6.9	45	2.8	88	41	55
3	**29-May-17**	32	30	1000	7.8	45	3.7	83	45	57
4	**7-Jun-17**	29	30	500	8.3	45	5	88	38	43
5	**14-Jun-17**	45	30	500	4.9	52	6.5	81	55	41
6	**20-Jun-17**	45	30	600	4.5	45	6.7	79	56	45
7	**23-Jun-17**	49	30	600	4.5	48	6	79	61	46
8	**25-Jun-17**	54	30	600	4.6	48	6	78	64	40
9	**28-Aug-18**	78	50	15	150	20	2.6	40	92	80
10	**25-Jan-19**	78	50	100	75	40	1	24	94	97
11	**30-Jan-19**	45	50	100	26	55	1	99	72	68
12	**31-Jan-19**	40	50	100	20	55	1	99	62	60
13	**1-Feb-19**	34	50	150	20	55	1	99	63	70
14	**4-Feb-19**	40	50	250	20	30	1	81	70	79

6.2.2 Detailed parameter profiles of the PSA process

The detailed operational process parameters in one day of running (Case 7, 23rd June 2017) were retrieved to show the operating status of the demonstrative PSA process.

Figure 6.6 illustrates the pressure swing patterns during the operation. The adsorption step was conducted at a constant high pressure of 30 bar, and the lowest pressure at the end of the desorption step averaged around 5 bar. The buffer tank provided a reservoir for holding the gas from one bed, reducing the pressure after the adsorption step from 30 bar to an intermediate pressure level of 22 bar. The adsorption column would then equalise with the other bed just finishing the desorption at around 5 bar to reach around 15 bar in this case, and started the desorption step until the pressure reached the lowest level. Following the desorption step, the pressure would be increase to 15 bar by the pressure equalization with the other column, and to 19 bar by receiving the stored gas in the buffer tank. Finally, the feed gas would re-pressurise the column to the feed pressure, ready for producing the light product.

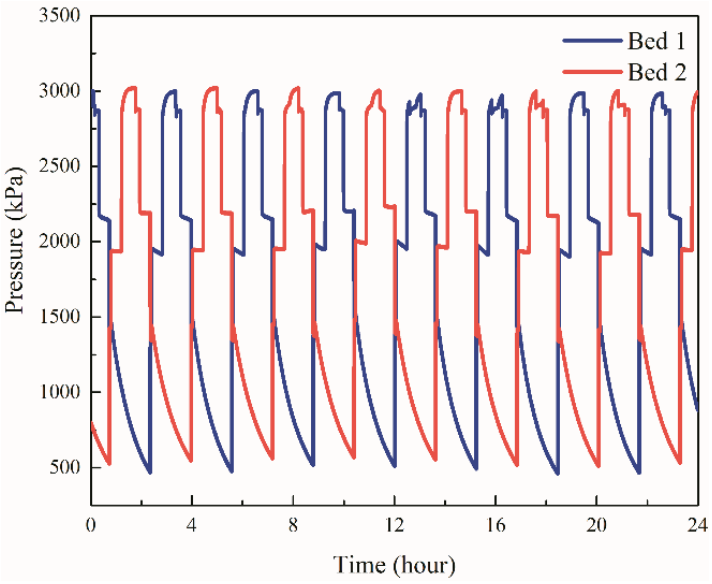

Figure 6.6. Pressure profiles for the two adsorption beds of the PSA process

According to theoretical calculations with the same feed and the lowest pressure as the operation conditions, the pressure at the end of pressure equalization step, namely the start of the desorption step, would be 17.5 bar if only one pair of pressure equalization steps was in the cycle, or 11.25 bar if two pairs were

designed. Thus, we can affirm the positive effect of the buffer tank for decreasing the number of components in the gas phase before the blowdown step, but the overall improvement to the process performance is far less than an additional pair of true pressure equalization steps. Besides, the pressure profile in the buffer tank also evidences its inefficiency. The actual pressure range inside the buffer tank during the operation was between 19 and 22 bar. That is to say, the total buffering capacity was the gas amount equivalent to a pressure change of 3 bar. It is because the buffer tank was not under a cycle scheme like a real adsorption column that a desorption step could clean the gas components in the bed and regenerate the capacity. Any attempts of increasing the capacity of the buffer tank would require extra and unnecessary efforts, which was not the intention of this PSA process.

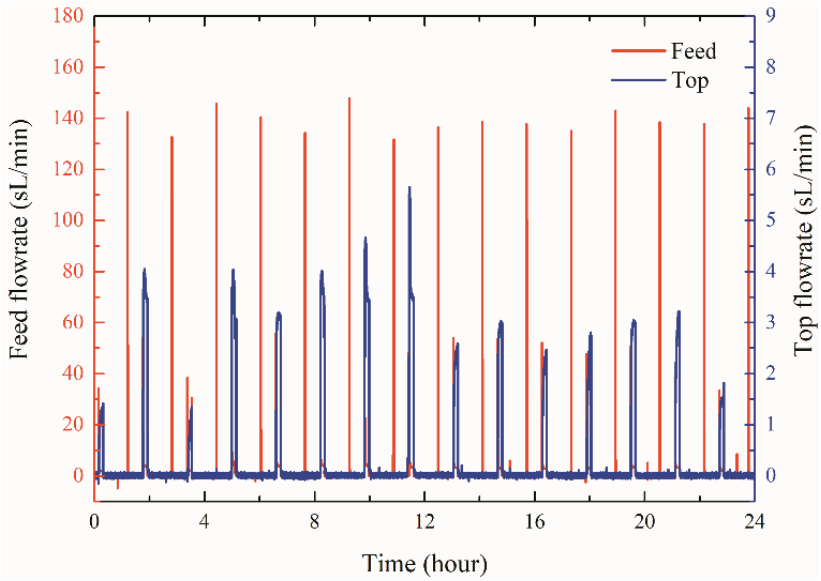

Figure 6.7. Profiles of feed gas flowrate and exiting gas flowrate in the top stream

Figure 6.7 shows the profiles of the feed gas flowrates and exiting gas flowrate of the CH_4 product stream. When combining Figure 6.6 and Figure 6.7, it can be found that majority of the gas entered the system at the beginning of the re-pressurization step when the pressure in feed gas was 30 bar while the pressure inside the column was around 19 bar; then the feed flowrate trended to a very low value or zero once the pressure in the bed was close to that of the feed gas. The same case occurred for the beginning of the adsorption step when the pressure at a feed stream pipeline was higher than that set for the back-pressure regulator. For the exiting stream, a high flowrate only occurred at the adsorption

step for each cycle and then the flowrate decreased gradually once the pressure after the back-pressure regulator had increased.

The outlet flowrate of the pipeline was limited to 3 – 4 $\mathrm{std.L/min}$ to protect the thermal oxidizer. From Figure 6.7, it can be observed that the flowrate peaks in the exiting stream and feed stream for the adsorption step were in good synchronization. The flowrate values of the exiting streams fluctuated as partial gas was taken in the flowrate of 1 – 2 $\mathrm{std.L/min}$ by the gas composition analyser.

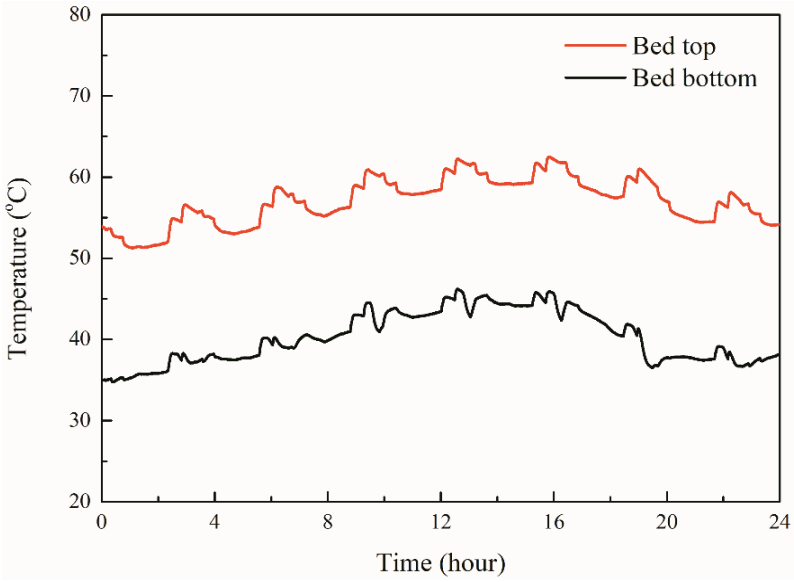

Figure 6.8. **Profile of temperatures in bed**

As mentioned before, the adsorption columns were covered with heating tape and insulation materials to maintain a relatively stable thermal condition from the outdoor environment. In this case, the temperatures at the top and bottom of the bed were maintained at an average of 40 and 55 ^{O}C, respectively, in Figure 6.8. The temperature swing in the bed was clearly shown with the two temperature lines. The feed gas was heated to 40 ^{O}C but it slightly changed with the ambient temperature. Also, the temperature alternation due to the day/night switch could also be observed in the figure.

6.2.3 Process simulation verification

Process simulations were conducted by employing the simplified 5-step model with the process conditions listed in Table 6.5. The key performance indicators, CH_4 recovery and CO_2 purity, determined by the simulation model are compared with the results from the actual PSA plant in Figure 6.9. Notably, the CH_4 purity

from the Otway PSA plant is used as the specification when running the simulation model, therefore, they are not displayed in the comparison graph.

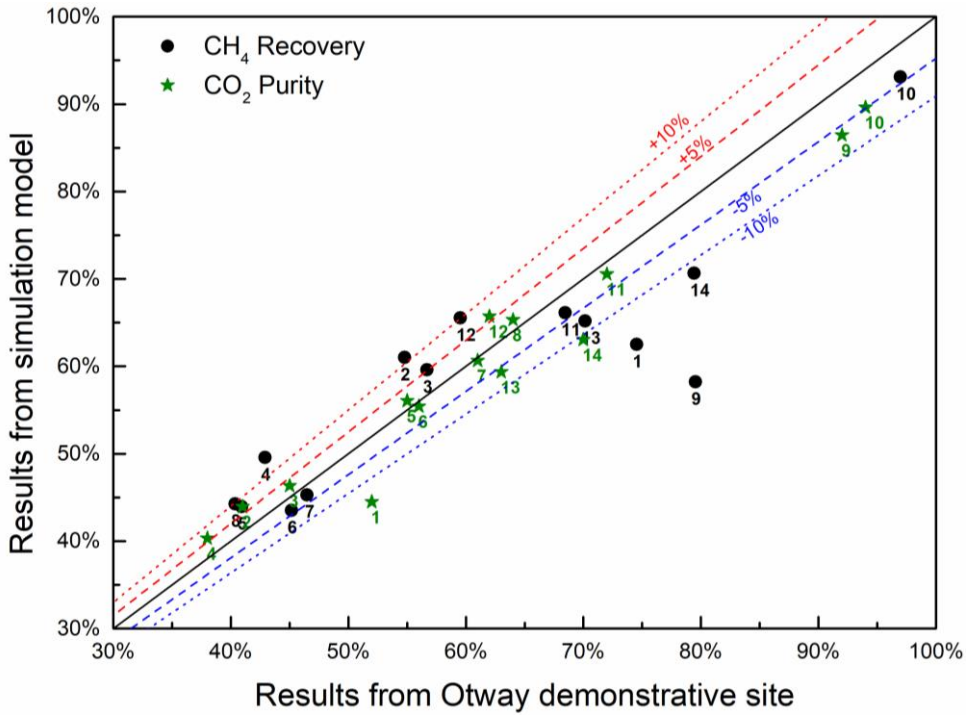

Figure 6.9. Comparison of the key process indicators between the demonstrative PSA plant and the 5-step simplified process simulation model. Case numbers are labeled under the corresponding data points.

The comparison results present that the CO_2 purity predicted by the simplified model is basically within ±10% of the process results, while divergences of the recovery of CH_4 are slightly higher. But still, for most of the cases, the simplified simulation model can reasonably predict the actual results from the demonstrative PSA plant.

These results together with our earlier discussion regarding the capacity of the buffer tank demonstrate that the additional buffer tank for another pair of equalization steps was not significant. In Chapter 5, we have revealed the difference in the resulting CH_4 recovery by introducing an additional pair of pressure equalization steps when comparing the results of the 3-step model and the 5-step model (Table 5.3). If the pressure equalization with the empty tank could reach the expected effects equivalent to a common pressure equalization step, the deviations of the results between the PSA plant (a process with “two” pairs of pressure equalization steps) and the simplified 5-step model (a process with one pair of pressure equalization steps) should be larger and, more

importantly, one-sided. But since no deviation was observed, it affirmed the validity of using the 5-step model to simulate the PSA plant of the Otway CO_2 capture site.

Secondly, the matching results between the PSA plant and the simulation again verify the validity of the simplified model we developed. In Chapter 5, the simplified model was validated by comparing the qualitative trend between different adsorbents with the results of a rigorous simulation model. In this chapter, the quantitative matching of the process results with a real PSA process is evidently more convincing. One more point to emphasize here is that the process conditions of the PSA plants are continuously varying, and the simplified model succeeds in predicting the process results under most of the conditions. This is in contrast to Chapter 5 where the operating conditions were constant, but the adsorbents were changed. Hence, our model is useful not just for adsorbent screening but also for assessing the impact of process parameters on performance for a given adsorbent.

6.3 Summary

The successful operations of the PSA process in the Otway CO_2 capture rig provide valuable data for studying and implementing PSA technology in high-pressure natural gas sweetening processes. The major outcome of the campaign is that it displays the technical feasibility of using a two-bed PSA process with Sorbead® WS as the adsorbent to remove CO_2 from a high-pressure natural gas mixture. Also, by conducting simulations by the simplified model with the operational conditions retrieved from the Otway PSA plant, we found that the 5-step simplified model could predict the actual process results very well. This verifies the validity of the newly developed simplified model.

CHAPTER 7

CONCLUSION AND FUTURE WORK

7.1 Conclusion

Although we have presented an individual summary at the end of each chapter, an integrated summary of the findings of this work is offered here. The main scope is to study the feasibility of the use of adsorption-based technology to remove CO_2 from natural gas at high pressures.

The adsorbent used in the process is a critical parameter for the adsorption technology. The present work commenced in Chapter 3 with characterizing a series of novel adsorbents, six high silica zeolites (CBV-760, CBV-780, HSZ-320HOA, HSZ-350HUA, HSZ-385HUA, and HSZ-390HUA) and a silica gel (Sorbead® WS), with potential high selectivity of CO_2 over CH_4 in the high-pressure applications. Their textural properties and adsorption isotherms at low and intermediate pressure ranges were measured by volumetric isotherms measurement methods. High-pressure adsorption isotherms at three different temperatures for each selected material were determined by gravimetric method. Also, the difference of the absolute adsorption amount and the excess adsorption amount from the results of high-pressure adsorption isotherms were specified, and the measurement data of all materials studied were provided in this work. To evaluate the performance of these adsorbents, two distinct methods were employed. A common adsorbent performance indicator, IAST selectivity, was used to predict the performance of the adsorbents. Besides, the process performances were also obtained by running the process simulation with a rigorous simulation model. The evaluation results of these two methods were significantly deviated, which raised a serious question, “whether the traditional adsorbent performance indicators are capable to evaluate the adsorbent for the CO_2/CH_4 adsorptive separation processes at high pressures”.

Then in Chapter 4, by reviewing the existing adsorbent performance indicators, we found the limitations in current adsorbent evaluation methods, and to overcome the known boundaries we proposed a new adsorbent performance indicator, adiabatic column working selectivity. The new indicator contained all

factors of previous performance indicators and added a new parameter, the component stored in the void phase of the column. The results of the new performance indicator suggested that the high inter- and intra-particle voidage of the adsorbent was detrimental to the process performance. Also, by comparing the adsorbent screening results by traditional and new performance indicators with rigorous process simulation results, we found that the newly proposed one could produce similar results as the process simulation, suggesting Sorbead® WS was the best adsorbent among the selected material, while the existing performance indicators more or less deviated from the simulation outcomes. The finding was an initial evidence supporting the feasibility of adiabatic column working selectivity as a valid performance indicator to evaluate and screen adsorbents for the application of CO_2 removal from sour natural gas at pressure. However, there was a high threshold of applying the newly developed indicator: the temperature and the bulk gas composition at the desorption step of the adsorption process were required for the calculation, but it was hard to get access to both process parameters without a process experiment or a simulation.

In Chapter 5, to ease the application of the adiabatic column working selectivity, we developed two simplified simulation models: the 3-step equilibrium PSA model, and the 5-step equilibrium PSA model including a pair of pressure equalization steps. The simulation result showed that the desorption compositions and temperatures obtained by simplified models agreed very well with the variables determined by the rigorous simulation model. Meanwhile, the results of the adiabatic column working selectivity using the process variables obtained by the simplified model could perfectly match the adsorbent screening results by the rigorous simulation model. This again proved the feasibility of the newly proposed performance indicator in Chapter 4.

In Chapter 6, the actual experiments of using a pressure-swing adsorption process to remove CO_2 from high-pressure natural gas were conducted on the PSA plant in the Otway CO_2 Capture Research Facility. The adsorbent used in the PSA plant was Sorbead® WS, the best adsorbent among the studied materials predicted by rigorous simulations and the adiabatic column working selectivity. The process operational results displayed the technical feasibility of the adsorption for the natural gas sweetening process, that pure CH_4 products

could be obtained with a reasonable recovery from high CO_2 content natural gas mixtures. Also, when using the process conditions as the simulation input to the simplified models we developed in Chapter 5, the results from the simulation model agreed well with the actual PSA process. This point is a critical piece of fact verifying the validity of the simplified model.

Overall, the most significant finding of this work is the novel adsorbent performance indicator, adiabatic column working selectivity. It can be used to evaluate the performance of adsorbents for the application of CO_2 removal from natural gas in the high-pressure. With the help of a newly developed simplified model which is verified by a real PSA process, the calculation results of the adiabatic column working selectivity can more precisely predict and screen adsorbents for the targeted application.

7.2 Recommendations for future work

The adsorbents studied in this work are a very small group of materials among a huge candidate pool. Although we have identified Sorbead® WS as a promising adsorbent for the application of CO_2 removal from natural gas, there is still a gap between its performances to the expected goals. To achieve high purity and high recovery of the methane product at the same time, looking for adsorbents with suitable adsorption properties is of the top priority. The adsorption properties of plenty of materials with various chemical natures can be measured using the same characterization method in this study, and then screened by the adiabatic column working selectivity to find a general best adsorbent for the application of CO_2 removal from natural gas.

Regarding the adiabatic column working selectivity, it is currently only valid for equilibrium separations because no kinetic behaviour is considered. Future research efforts can be focused on extending the application scope to kinetic separations by introducing the mass transfer coefficients of the gas component into the calculation. Besides, in Chapter 4 the screening results of the adiabatic column working selectivity suggests that the high void space and low bulk density of the adsorbent in the packed adsorption column can cause negative impacts on the process performances. Optimization on this factor should be considered for future adsorption process design, especially for those process operated in

the high pressures.

BIBLIOGRAPHY

[1] V. Masson-Delmotte, P. Zhai, H.-O. Pörtner, D. Roberts, J. Skea, P.R. Shukla, A. Pirani, W. Moufouma-Okia, C. Péan, R. Pidcock, Global warming of 1.5 C, An IPCC Spec. Rep. Impacts Glob. Warm. 1 (2018).

[2] International Energy Agency, CO2 emissions from fuel combustion, 2019. https://doi.org/10.1670/96-03N.

[3] International Energy Agency, World Energy Outlook 2019, 2019. https://webstore.iea.org/download/summary/2467?fileName=Japanese-Summary-WEO2019.pdf.

[4] UNFCCC, ADOPTION OF THE PARIS AGREEMENT, 2015. https://unfccc.int/resource/docs/2015/cop21/eng/l09r01.pdf.

[5] B. Shimekit, H. Mukhtar, Natural Gas Purification Technologies - Major Advances for CO2 Separation and Future Directions, Adv. Nat. Gas Technol. (2012). https://doi.org/10.5772/38656.

[6] O.S. Ismail, G.E. Umukoro, Modelling combustion reactions for gas flaring and its resulting emissions, J. King Saud Univ. - Eng. Sci. 28 (2016) 130–140. https://doi.org/10.1016/j.jksues.2014.02.003.

[7] W.F.J. Burgers, P.S. Northrop, H.S. Kheshgi, J.A. Valencia, Worldwide development potential for sour gas, Energy Procedia. 4 (2011) 2178–2184. https://doi.org/10.1016/j.egypro.2011.02.104.

[8] S. Brennan, H. Adrian, F. S. Julio, B. Rorbert C., Natural gas reservoirs with high CO2 concentrations as natural analogs for CO2 storage, in: Greenh. Gas Control Technol. 7, Elsevier, 2005: pp. 1381–1387. https://doi.org/10.1016/B978-008044704-9/50153-1.

[9] J.M. Klinkenbijl, M.L. Dillon, E.C. Heyman, Gas pre-treatment and their impact on liquefaction processes, GPA Annu. Conv. Proc. (1999) 299–307.

[10] A.L. Kohl, R.B. Nielsen, Absorption of Water Vapor by Dehydrating Solutions, Gas Purif. (1997) 946–1021. https://doi.org/10.1016/b978-088415220-0/50011-2.

[11] J.U. Keller, R. Staudt, Gas adsorption equilibria: experimental methods and adsorptive isotherms, Springer Science & Business Media, 2005.

[12] R.T. Yang, Gas Separation by Adsorption Processes, Butterworth Publishers, 1987.

[13] R. Chatti, A.K. Bansiwal, J.A. Thote, V. Kumar, P. Jadhav, S.K. Lokhande, R.B. Biniwale, N.K. Labhsetwar, S.S. Rayalu, Amine loaded zeolites for carbon dioxide capture: Amine loading and adsorption studies, Microporous Mesoporous Mater. 121 (2009) 84–89. https://doi.org/10.1016/j.micromeso.2009.01.007.

[14] F. Su, C. Lu, S.C. Kuo, W. Zeng, Adsorption of CO2 on amine-functionalized y-type zeolites, Energy and Fuels. 24 (2010) 1441–1448. https://doi.org/10.1021/ef901077k.

[15] D.P. Bezerra, F.W.M.D. Silva, P.A.S.D. Moura, A.G.S. Sousa, R.S. Vieira, E. Rodriguez-Castellon, D.C.S. Azevedo, CO2 adsorption in amine-grafted zeolite 13X, Appl. Surf. Sci. 314 (2014) 314–321. https://doi.org/10.1016/j.apsusc.2014.06.164.

[16] X. Wang, J. Jia, L. Zhao, T. Sun, Chemisorption of hydrogen sulphide on zinc oxide modified aluminum-substituted SBA-15, Appl. Surf. Sci. 254 (2008) 5445–5451.

[17] M. Thommes, K. Kaneko, A. V. Neimark, J.P. Olivier, F. Rodriguez-Reinoso, J. Rouquerol, K.S.W. Sing, Physisorption of gases, with special reference to the evaluation of surface area and pore size distribution (IUPAC Technical Report), Pure Appl. Chem. 87 (2015) 1051–1069. https://doi.org/10.1515/pac-2014-1117.

[18] D.D. Do, Adsorption Analysis: Equilibria and Kinetics, 1998. https://doi.org/10.1142/9781860943829.

[19] D.M. Ruthven, Principles of adsorption and adsorption processes, John Wiley & Sons, 1984.

[20] J. Koresh, A. Soffer, Study of molecular sieve carbons. Part 1.—Pore structure, gradual pore opening and mechanism of molecular sieving, J. Chem. Soc. Faraday Trans. 1 Phys. Chem. Condens. Phases. 76 (1980) 2457–2471.

[21] S.H. Joo, S. Jun, R. Ryoo, Synthesis of ordered mesoporous carbon molecular sieves CMK-1, Microporous Mesoporous Mater. 44–45 (2001) 153–158. https://doi.org/10.1016/S1387-1811(01)00179-2.

[22] L. Zhou, X. Liu, J. Li, N. Wang, Z. Wang, Y. Zhou, Synthesis of ordered mesoporous carbon molecular sieve and its adsorption capacity for H2, N2, O2, CH4 and CO2, Chem. Phys. Lett. 413 (2005) 6–9. https://doi.org/10.1016/j.cplett.2005.07.048.

[23] R.C. Bansal, M. Goyal, Activated carbon adsorption, CRC press, 2005.

[24] H.E. Bergna, Colloid Chemistry of Silica, an overview, in: Colloid. Silica, American Chemical Society, 1994: pp. 1–47. https://doi.org/10.1097/00010694-195507000-00014.

[25] O.M. Yaghi, M. O'Keeffe, N.W. Ockwig, H.K. Chae, M. Eddaoudi, J. Kim, Reticular synthesis and the design of new materials, Nature. 423 (2003) 705–714. https://doi.org/10.1038/nature01650.

[26] S.L. James, Metal-organic frameworks, Chem. Soc. Rev. 32 (2003) 276–288.

[27] H.C. Zhou, J.R. Long, O.M. Yaghi, Introduction to metal-organic frameworks, Chem. Rev. 112 (2012) 673–674. https://doi.org/10.1021/cr300014x.

[28] T.G. Glover, B. Mu, Gas Adsorption in Metal-Organic Frameworks: Fundamentals and Applications, CRC Press, 2018.

[29] J.A. Ritter, A.D. Ebner, State-of-the-art adsorption and membrane

separation processes for hydrogen production in the chemical and petrochemical industries, Sep. Sci. Technol. 42 (2007) 1123–1193.

[30] C.A. Grande, S. Roussanaly, R. Anantharaman, K. Lindqvist, P. Singh, J. Kemper, CO2 Capture in Natural Gas Production by Adsorption Processes, Energy Procedia. 114 (2017) 2259–2264. https://doi.org/10.1016/j.egypro.2017.03.1363.

[31] A.F. Ismail, K.C. Khulbe, T. Matsuura, Fundamentals of Gas Permeation Through Membranes, in: Gas Sep. Membr., Springer, 2015: pp. 11–35.

[32] Z.J. Pan, R.T. Yang, J.A. Ritter, Kinetic separation of air by pressure swing adsorption, Butterworths: Boston, 1989.

[33] A.L. Kohl, R. Nielsen, Gas Purification, 5th ed., Gulf Pub., 1997. https://search.ebscohost.com/login.aspx?direct=true&AuthType=sso&db=cat00006a&AN=melb.b4056042&site=eds-live&scope=site&custid=s2775460.

[34] I. Langmuir, The adsorption of gases on plane surfaces of glass, mica and platinum, J. Am. Chem. Soc. 40 (1918) 1361–1403. https://doi.org/10.1021/ja02242a004.

[35] P.M. Mathias, R. Kumar, J.D. Moyer, J.M. Schork, S.R. Srinivasan, S.R. Auvil, O. Talu, Correlation of multicomponent gas adsorption by the dual-site Langmuir model. Application to nitrogen/oxygen adsorption on 5A-zeolite, Ind. Eng. Chem. Res. 35 (1996) 2477–2483. https://doi.org/10.1021/ie950291y.

[36] E.C. Markham, A.F. Benton, The adsorption of gas mixtures by silica, J. Am. Chem. Soc. 53 (1931) 497–507. https://doi.org/10.1021/ja01353a013.

[37] M. Jaroniec, J. Tóth, Adsorption of gas mixtures on heterogeneous solid surfaces - III. Extension of Tóth isotherm on multilayer adsorption of gas mixtures, Colloid Polym. Sci. Kolloid-Zeitschrift Zeitschrift Für Polym. 256 (1978) 690–695. https://doi.org/10.1007/BF01784411.

[38] A.L. Myers, J.M. Prausnitz, Thermodynamics of Mixed-Gas Adsorption, 11 (n.d.) 121–127.

[39] G.M. Dorris, D.G. Gray, Adsorption, spreading pressure, and london force interactions of hydrocarbons on cellulose and wood fiber surfaces, J. Colloid Interface Sci. 71 (1979) 93–106. https://doi.org/10.1016/0021-9797(79)90224-8.

[40] S. Sircar, T.C. Golden, Pressure swing adsorption technology for hydrogen production, in: Hydrog. Syngas Prod. Purif. Technol., Hoboken, New Jersey: John Wiley & Sons, Inc, 2009: pp. 414–450.

[41] S. Sircar, Air Fractionation by Adsorption, Sep. Sci. Technol. 23 (1988) 2379–2396. https://doi.org/10.1080/01496398808058460.

[42] S. Cavenati, C.A. Grande, A.E. Rodrigues, Adsorption Equilibrium of Methane, Carbon Dioxide, and Nitrogen on Zeolite 13X at High Pressures, J. Chem. Eng. Data. 49 (2004) 1095–1101. https://doi.org/10.1021/je0498917.

[43] M.P.S. Santos, C.A. Grande, A.E. Rodrigues, Pressure swing adsorption for biogas upgrading. Effect of recycling streams in pressure swing adsorption design, Ind. Eng. Chem. Res. 50 (2011) 974–985. https://doi.org/10.1021/ie100757u.

[44] Y.J. Kim, Y.S. Nam, Y.T. Kang, Study on a numerical model and PSA (pressure swing adsorption) process experiment for CH4/CO2 separation from biogas, Energy. 91 (2015) 732–741. https://doi.org/10.1016/j.energy.2015.08.086.

[45] C.A. Grande, Biogas upgrading by pressure swing adsorption, Biofuel's Eng. Process Technol. (2011) 65–84.

[46] J. Collins, Bulk separation of carbon dioxide from natural gas, (1973).

[47] R. Kumar, Adsorptive process for producing two gas streams from a gas mixture, (1990).

[48] K.F. Butwell, W.B. Dolan, S.M. Kuznicki, Selective removal of nitrogen from natural gas by pressure swing adsorption, (2001).

[49] S. Alizadeh-Khiavi, J.A. Sawada, A.C. Gibbs, J. Alvaji, Rapid cycle syngas pressure swing adsorption system, (2010).

[50] L. Peters, A. Hussain, M. Follmann, T. Melin, M.-B. Hägg, CO2 removal from natural gas by employing amine absorption and membrane technology—A technical and economical analysis, Chem. Eng. J. 172 (2011) 952–960.

[51] D. Danaci, CARBON DIOXIDE SEPARATION FROM NATURAL GAS: EVALUATION OF ADSORBENTS AND INFLUENCE OF PROCESS VARIABLES, The University of Melbourne, 2018.

[52] D. Danaci, R. Singh, P. Xiao, P.A. Webley, Assessment of ZIF materials for CO2 capture from high pressure natural gas streams, Chem. Eng. J. 280 (2015) 486–493. https://doi.org/10.1016/j.cej.2015.04.090.

[53] L.A.M. Rocha, K.A. Andreassen, C.A. Grande, Separation of CO2/CH4using carbon molecular sieve (CMS) at low and high pressure, Chem. Eng. Sci. 164 (2017) 148–157. https://doi.org/10.1016/j.ces.2017.01.071.

[54] A. Arami-Niya, T.E. Rufford, Z. Zhu, Activated carbon monoliths with hierarchical pore structure from tar pitch and coal powder for the adsorption of CO2, CH4 and N2, Carbon N. Y. 103 (2016) 115–124. https://doi.org/10.1016/j.carbon.2016.02.098.

[55] Y.J. Wu, Y. Yang, X.M. Kong, P. Li, J.G. Yu, A.M. Ribeiro, A.E. Rodrigues, Adsorption of Pure and Binary CO2, CH4, and N2 Gas Components on Activated Carbon Beads, J. Chem. Eng. Data. 60 (2015) 2684–2693. https://doi.org/10.1021/acs.jced.5b00321.

[56] R. Ullah, M. Ali H Salah Saad, S. Aparicio, M. Atilhan, Adsorption equilibrium studies of CO2, CH4 and N2 on various modified zeolites at high pressures up to 200 bars, Microporous Mesoporous Mater. 262 (2018) 49–58. https://doi.org/10.1016/j.micromeso.2017.11.022.

[57] J.G. Min, K.C. Kemp, S.B. Hong, Zeolites ZSM-25 and PST-20: selective carbon dioxide adsorbents at high pressures, J. Phys. Chem. C. 121 (2017) 3404–3409.

[58] X. Zhou, W. Huang, J. Miao, Q. Xia, Z. Zhang, H. Wang, Z. Li, Enhanced separation performance of a novel composite material GrO@ MIL-101 for CO2/CH4 binary mixture, Chem. Eng. J. 266 (2015) 339–344.

[59] V.I. Agueda, J.A. Delgado, M.A. Uguina, P. Brea, A.I. Spjelkavik, R. Blom, C. Grande, Adsorption and diffusion of H2, N2, CO, CH4 and CO2 in UTSA-16 metal-organic framework extrudates, Chem. Eng. Sci. 124 (2015) 159–169.

[60] Y. Zhang, W. Su, Y. Sun, J. Liu, X. Liu, X. Wang, Adsorption Equilibrium of N2, CH4, and CO2 on MIL-101, J. Chem. Eng. Data. 60 (2015) 2951–2957. https://doi.org/10.1021/acs.jced.5b00327.

[61] G. Autié Castro, E. de Oliveira Jardim, E. Reguera, E. Vilarrasa-Garcia, E. Rodriguez-Castellon, C.L. Cavalcante Jr., CH4 and CO2 Adsorption Study in ZIF-8 and Al-BDC MOFs, Biol. Chem. Res. (2017) 234–246.

[62] X. Liu, L. Zhou, X. Fu, Y. Sun, W. Su, Y. Zhou, Adsorption and regeneration study of the mesoporous adsorbent SBA-15 adapted to the capture/separation of CO2 and CH4, Chem. Eng. Sci. 62 (2007) 1101–1110.

[63] S.-P. Lee, N. Mellon, A.M. Shariff, J.-M. Leveque, High-pressure CO2-CH4 selective adsorption on covalent organic polymer, J. Nat. Gas Sci. Eng. 50 (2018) 139–146.

[64] Q. Al-Naddaf, A.A. Rownaghi, F. Rezaei, Multicomponent adsorptive separation of CO2, CO, CH4, N2, and H2 over core-shell zeolite-5A@MOF-74 composite adsorbents, Chem. Eng. J. 384 (2020) 123251. https://doi.org/10.1016/j.cej.2019.123251.

[65] M.A. Moreira, A.M. Ribeiro, A.F.P. Ferreira, A.E. Rodrigues, Cryogenic pressure temperature swing adsorption process for natural gas upgrade, Sep. Purif. Technol. 173 (2017) 339–356. https://doi.org/10.1016/j.seppur.2016.09.044.

[66] M.A. Moreira, R.O.M. Dias, U.H. Lee, J.S. Chang, A.M. Ribeiro, A.F.P. Ferreira, A.E. Rodrigues, Adsorption Equilibrium of Carbon Dioxide, Methane, Nitrogen, Carbon Monoxide, and Hydrogen on UiO-66(Zr)_(COOH)2, J. Chem. Eng. Data. 64 (2019) 4724–4732. https://doi.org/10.1021/acs.jced.9b00053.

[67] P.J. Cook, A. Rigg, J. Bradshaw, Putting it back where it came from: Is geological disposal of carbon dioxide an option for Australia?, J. Aust. Pet. Prod. Explor. Assoc. 40 (2000) 654–666.

[68] N Kaliyan, R V Morey, W F Wilcke, Alagusundaram K., Gayathri P., Applications of Carbon Dioxide in Food and Processing Industries: Current Status and Future Thrusts, in: 2007 ASAE Annu. Meet., American Society of Agricultural and Biological Engineers, 2007. https://doi.org/10.13031/2013.23553.

[69] H. Furukawa, N. Ko, Y.B. Go, N. Aratani, S.B. Choi, E. Choi, A.Ö. Yazaydin, R.Q. Snurr, M. O'Keeffe, J. Kim, O.M. Yaghi, Ultrahigh porosity in metal-organic frameworks, Science (80-.). 329 (2010) 424–428. https://doi.org/10.1126/science.1192160.

[70] Y.N.I. Chan, F.B. Hill, Y.W. Wong, Equilibrium theory of a pressure swing adsorption process, Chem. Eng. Sci. 36 (1981) 243–251. https://doi.org/10.1016/0009-2509(81)85002-6.

[71] K.S. Knaebel, For your next separation consider adsorption, Chem. Eng. (New York). 102 (1995).

[72] H.C. CHENG, F.B. HILL, Recovery and Purification of Light Gases by Pressure Swing Adsorption, in: Ind. Gas Sep., AMERICAN CHEMICAL SOCIETY, 1983: pp. 10–195. https://doi.org/doi:10.1021/bk-1983-0223.ch010.

[73] J.C. Kayser, K.S. Knaebel, Pressure swing adsorption: Development of an equilibrium theory for binary gas mixtures with nonlinear isotherms, Chem. Eng. Sci. 44 (1989) 1–8. https://doi.org/10.1016/0009-2509(89)85226-1.

[74] D.M. Ruthven, C.B. Ching, Counter-current and simulated counter-current adsorption separation processes, Chem. Eng. Sci. 44 (1989) 1011–1038.

[75] S.J. Bhadra, S. Farooq, Separation of methane-nitrogen mixture by pressure swing adsorption for natural gas upgrading, Ind. Eng. Chem. Res. 50 (2011) 14030–14045. https://doi.org/10.1021/ie201237x.

[76] S. Cavenati, C.A. Grande, A.E. Rodrigues, Separation of CH4 / CO2 / N2 mixtures by layered pressure swing adsorption for upgrade of natural gas, Chem. Eng. Sci. 61 (2006) 3893–3906. https://doi.org/10.1016/j.ces.2006.01.023.

[77] P.J.E. Harlick, F.H. Tezel, An experimental adsorbent screening study for CO2 removal from N2, Microporous Mesoporous Mater. 76 (2004) 71–79. https://doi.org/10.1016/j.micromeso.2004.07.035.

[78] M.W. Ackley, Multilayer adsorbent beds for PSA gas separation, (2000).

[79] J. Zhang, R. Singh, P.A. Webley, Alkali and alkaline-earth cation exchanged chabazite zeolites for adsorption based CO2 capture, Microporous Mesoporous Mater. 111 (2008) 478–487. https://doi.org/10.1016/j.micromeso.2007.08.022.

[80] F. Notaro, J.T. Mullhaupt, F.W. Leavitt, M.W. Ackley, Adsorption process and system using multilayer adsorbent beds, US 5,674,311, 1997.

[81] S.U. Rege, R.T. Yang, A simple parameter for selecting an adsorbent for gas separation by pressure swing adsorption, Sep. Sci. Technol. 36 (2001) 3355–3365. https://doi.org/10.1081/SS-100107907.

[82] A.D. Wiersum, J.S. Chang, C. Serre, P.L. Llewellyn, An adsorbent performance indicator as a first step evaluation of novel sorbents for gas separations: Application to metal-organic frameworks, Langmuir. 29 (2013) 3301–3309. https://doi.org/10.1021/la3044329.

[83] A.K. Rajagopalan, A.M. Avila, A. Rajendran, Do adsorbent screening metrics predict process performance? A process optimisation based study for post-combustion capture of CO2, Int. J. Greenh. Gas Control. 46 (2016) 76–85. https://doi.org/10.1016/j.ijggc.2015.12.033.

[84] A. Ntiamoah, J. Ling, P. Xiao, P.A. Webley, Y. Zhai, CO2 capture by vacuum swing adsorption: role of multiple pressure equalization steps, Adsorption. 21 (2015) 509–522. https://doi.org/10.1007/s10450-015-9690-8.

[85] M. Yavary, H.A. Ebrahim, C. Falamaki, The effect of number of pressure equalization steps on the performance of pressure swing adsorption process, Chem. Eng. Process. Process Intensif. 87 (2015) 35–44. https://doi.org/10.1016/j.cep.2014.11.003.

[86] L. Tao, P. Xiao, A. Qader, P.A. Webley, CO2 capture from high concentration CO2 natural gas by pressure swing adsorption at the CO2CRC Otway site, Australia, Int. J. Greenh. Gas Control. 83 (2019) 1–10. https://doi.org/10.1016/j.ijggc.2018.12.025.

[87] O. Kunz, W. Wagner, The GERG-2008 wide-range equation of state for natural gases and other mixtures: An expansion of GERG-2004, J. Chem. Eng. Data. 57 (2012) 3032–3091. https://doi.org/10.1021/je300655b.

[88] A.L. Myers, P.A. Monson, Adsorption in porous materials at high pressure: Theory and experiment, Langmuir. 18 (2002) 10261–10273. https://doi.org/10.1021/la026399h.

[89] H.G.T. Nguyen, L. Espinal, R.D. van Zee, M. Thommes, B. Toman, M.S.L. Hudson, E. Mangano, S. Brandani, D.P. Broom, M.J. Benham, K. Cychosz, P. Bertier, F. Yang, B.M. Krooss, R.L. Siegelman, M. Hakuman, K. Nakai, A.D. Ebner, L. Erden, J.A. Ritter, A. Moran, O. Talu, Y. Huang, K.S. Walton, P. Billemont, G. De Weireld, A reference high-pressure CO2 adsorption isotherm for ammonium ZSM-5 zeolite: results of an interlaboratory study, Adsorption. 24 (2018) 531–539. https://doi.org/10.1007/s10450-018-9958-x.

[90] F. Dreisbach, R. Staudt, J.U. Keller, High pressure adsorption data of methane, nitrogen, carbon dioxide and their binary and ternary mixtures on activated carbon, Adsorption. 5 (1999) 215–227. https://doi.org/10.1023/A:1008914703884.

[91] J. V. Milato, R.J. França, M.R.C. Marques, Pyrolysis of oil sludge from the offshore petroleum industry: influence of different mesoporous zeolites catalysts to obtain paraffinic products, Environ. Technol. (United Kingdom). 0 (2019) 1–10. https://doi.org/10.1080/09593330.2019.1650833.

[92] A. Zukal, V. Patzelová, U. Lohse, Secondary porous structure of dealuminated Y zeolites, Zeolites. 6 (1986) 133–136. https://doi.org/10.1016/S0144-2449(86)80011-2.

[93] K. Sato, Y. Nishimura, N. Matsubayashi, M. Imamura, H. Shimada, Structural changes of Y zeolites during ion exchange treatment: Effects of Si/Al ratio of the starting NaY, Microporous Mesoporous Mater. 59 (2003)

133–146. https://doi.org/10.1016/S1387-1811(03)00305-6.

[94] Z. Bao, L. Yu, T. Dou, Y. Gong, Q. Zhang, Q. Ren, X. Lu, S. Deng, Adsorption equilibria of CO2, CH4, N2, O2, and Ar on high silica zeolites, J. Chem. Eng. Data. 56 (2011) 4017–4023. https://doi.org/10.1021/je200394p.

[95] H. Pan, J.A. Ritter, P.B. Balbuena, Examination of the approximations used in determining the isosteric heat of adsorption from the Clausius-Clapeyron equation, Langmuir. 14 (1998) 6323–6327. https://doi.org/10.1021/la9803373.

[96] M. Tagliabue, C. Rizzo, N.B. Onorati, E.F. Gambarotta, A. Carati, F. Bazzano, Regenerability of zeolites as adsorbents for natural gas sweetening: A case-study, Fuel. 93 (2012) 238–244. https://doi.org/10.1016/j.fuel.2011.08.051.

[97] C.W. Skarstrom, Method and apparatus for fractionating gaseous mixtures by adsorption, (1960).

[98] J.H. Cavka, C.A. Grande, G. Mondino, R. Blom, High pressure adsorption of CO2 and CH4 on Zr-MOFs, Ind. Eng. Chem. Res. 53 (2014) 15500–15507. https://doi.org/10.1021/ie500421h.

[99] J.J. Gutiérrez-Sevillano, A. Caro-Pérez, D. Dubbeldam, S. Calero, Molecular simulation investigation into the performance of Cu–BTC metal–organic frameworks for carbon dioxide–methane separations, Phys. Chem. Chem. Phys. 13 (2011) 20453–20460.

[100] B. Liu, Y. Zhu, S. Liu, J. Mao, Adsorption equilibrium of thiophenic sulfur compounds on the Cu-BTC metal-organic framework, J. Chem. Eng. Data. 57 (2012) 1326–1330. https://doi.org/10.1021/je300130s.

[101] L.A.M. Rocha, K.A. Andreassen, C.A. Grande, Separation of CO2/CH4 using carbon molecular sieve (CMS) at low and high pressure, Chem. Eng. Sci. 164 (2017) 148–157. https://doi.org/10.1016/j.ces.2017.01.071.

[102] B.J. Maring, P.A. Webley, A new simplified pressure/vacuum swing adsorption model for rapid adsorbent screening for CO2 capture applications, Int. J. Greenh. Gas Control. 15 (2013) 16–31. https://doi.org/10.1016/j.ijggc.2013.01.009.

[103] R. Kumar, Adsorption Column Blowdown: Adiabatic Equilibrium Model for Bulk Binary Gas Mixtures, Ind. Eng. Chem. Res. 28 (1989) 1677–1683. https://doi.org/10.1021/ie00095a017.

APPENDIX A

INTERMEDIATE-PRESSURE EXPERIMENTAL DATA OF THE ADSORPTION ISOTHERMS FOR STUDIED ADSORBENTS

This appendix contains the adsorption isotherm data of seven studied zeolites in the intermediate-pressure regime results generated from undertaking the analysis in Chapter 3.

Table A.1. Experimental adsorption isotherms of CH_4 on HSZ-320HOA

T = 303 K		T = 313 K		T = 333 K	
$\boldsymbol{P}$	$\boldsymbol{n}$	$\boldsymbol{P}$	$\boldsymbol{n}$	$\boldsymbol{P}$	$\boldsymbol{n}$
bar	$mmol \cdot g^{-1}$	bar	$mmol \cdot g^{-1}$	bar	$mmol \cdot g^{-1}$
0.00659	0.00127	0.0094	0.00139	0.00975	8.99E-04
0.01318	0.0026	0.01612	0.00233	0.01659	0.00151
0.01977	0.00394	0.02546	0.00393	0.02621	0.00254
0.02633	0.0053	0.03214	0.00495	0.03308	0.00324
0.03289	0.00673	0.04369	0.00696	0.04374	0.0044
0.04377	0.00913	0.06255	0.01025	0.06249	0.0065
0.06239	0.01331	0.09184	0.01536	0.09238	0.00992
0.0896	0.01948	0.12841	0.02174	0.12845	0.01406
0.12842	0.02818	0.18427	0.03162	0.18435	0.02042
0.18437	0.0408	0.26787	0.04628	0.26486	0.02971
0.2678	0.0595	0.38056	0.06612	0.38095	0.04303
0.38087	0.08455	0.55079	0.09578	0.54973	0.06219
0.5493	0.12145	0.78844	0.13654	0.78979	0.08918
0.78943	0.17301	1.1406	0.19592	1.14255	0.12842
1.14246	0.24718	1.64485	0.27893	1.65049	0.18359
1.65002	0.35034	2.37417	0.39425	2.38402	0.26097
2.38622	0.49279	3.44158	0.55308	3.46399	0.36652
3.46464	0.68739	4.99488	0.76366	5.03672	0.50886
5.04254	0.94348	7.28574	1.03589	7.37093	0.69544
7.37851	1.26424	9.98773	1.31003	9.98904	0.8674
9.98718	1.55965				

Table A.2. **Experimental adsorption isotherms of CO_2 on HSZ-320HOA**

T = 303 K		T = 313 K		T = 333 K	
$\boldsymbol{P}$	$\boldsymbol{n}$	$\boldsymbol{P}$	$\boldsymbol{n}$	$\boldsymbol{P}$	$\boldsymbol{n}$
bar	$mmol \cdot g^{-1}$	bar	$mmol \cdot g^{-1}$	bar	$mmol \cdot g^{-1}$
0.00157	0.02299	0.00209	0.02072	0.00323	0.01607
0.00966	0.1216	0.01184	0.10166	0.01011	0.04681
0.01395	0.1654	0.01374	0.11552	0.01597	0.07149
0.02113	0.23105	0.02157	0.16954	0.02113	0.09204
0.0308	0.30778	0.03149	0.2308	0.03068	0.128
0.04369	0.3964	0.04316	0.29509	0.04438	0.17561
0.06236	0.50544	0.06206	0.3862	0.06356	0.23627
0.08931	0.63758	0.08969	0.5001	0.09039	0.31209
0.12824	0.79687	0.1284	0.63441	0.12948	0.40911
0.18353	0.98592	0.18417	0.79714	0.18491	0.52792
0.26355	1.21561	0.26422	0.9926	0.26594	0.67519
0.37783	1.49318	0.37875	1.22817	0.3796	0.85028
0.54536	1.83742	0.54568	1.51851	0.54537	1.06522
0.78583	2.24864	0.7857	1.86994	0.78378	1.32646
1.12879	2.72196	1.12998	2.28716	1.12946	1.64545
1.62587	3.24368	1.62542	2.76419	1.62437	2.02506
2.33693	3.7693	2.33773	3.27819	2.33752	2.46715
3.35454	4.25506	3.36381	3.78674	3.37507	2.92334
4.84326	4.68305	4.82701	4.25138	4.82366	3.40332
6.96285	5.04398	6.95038	4.65108	6.98452	3.86604
9.98752	5.38054	9.98747	5.02677	9.98462	4.27841

Table A.3. **Experimental adsorption isotherms of CH_4 on HSZ-350HUA**

T = 303 K		T = 313 K		T = 333 K	
$\boldsymbol{P}$	$\boldsymbol{n}$	$\boldsymbol{P}$	$\boldsymbol{n}$	$\boldsymbol{P}$	$\boldsymbol{n}$
bar	$mmol \cdot g^{-1}$	bar	$mmol \cdot g^{-1}$	bar	$mmol \cdot g^{-1}$
0.73094	0.14323	0.71413	0.1156	0.71392	0.07443
0.88594	0.17213	0.89103	0.14196	0.87425	0.08993
1.06965	0.2061	1.07089	0.16796	1.07233	0.10877
1.31257	0.25041	1.31865	0.2035	1.31593	0.13118
1.60544	0.30281	1.61562	0.24531	1.61652	0.15756
1.97301	0.36755	1.98001	0.29552	1.98185	0.18851
2.41788	0.44362	2.42727	0.35543	2.42944	0.22484
2.95834	0.5333	2.97818	0.42633	2.98285	0.26793
3.62975	0.64058	3.65116	0.50968	3.65871	0.31782
4.44589	0.76462	4.48051	0.60698	4.49006	0.3758
5.44725	0.90759	5.50143	0.7192	5.51601	0.44368
6.67716	1.07037	6.75677	0.84757	6.77886	0.51982
8.18669	1.25072	8.30583	0.98804	8.33598	0.60256
9.99339	1.4575	9.99323	1.13809	9.994	0.68287

Table A.4. **Experimental adsorption isotherms of CO_2 on HSZ-350HUA**

T = 303 K		T = 313 K		T = 333 K	
$\boldsymbol{P}$	$\boldsymbol{n}$	$\boldsymbol{P}$	$\boldsymbol{n}$	$\boldsymbol{P}$	$\boldsymbol{n}$
bar	$mmol \cdot g^{-1}$	bar	$mmol \cdot g^{-1}$	bar	$mmol \cdot g^{-1}$
0.01213	0.02574	1.01806	1.05457	1.01091	0.69423
0.01683	0.03553	1.31834	1.2939	1.32473	0.86287
0.02281	0.04766	1.62005	1.5221	1.62287	1.01756
0.02829	0.05863	1.96966	1.77174	1.9708	1.18529
0.03617	0.0741	2.4151	2.06784	2.41283	1.3899
0.04316	0.08718	2.95924	2.39858	2.96112	1.62569
0.05315	0.1057	3.62599	2.75532	3.6256	1.888
0.0641	0.12547	4.44313	3.12689	4.4431	2.18042
0.07877	0.1516	5.44511	3.49196	5.44751	2.49002
0.09633	0.18194	6.66756	3.83255	6.67198	2.80444
0.11653	0.21591	8.1703	4.13795	8.18024	3.10461
0.14294	0.2586	9.9931	4.49227	9.99437	3.44444
0.17471	0.30873				
0.2136	0.36769				
0.26102	0.4368				
0.31807	0.51703				
0.38995	0.61424				
0.47743	0.72757				
0.58384	0.86009				
0.71559	1.01743				
0.87664	1.20195				
1.07251	1.4162				
1.31307	1.666				
1.60812	1.95507				
1.97164	2.28146				
2.41656	2.63928				
2.96184	3.0156				
3.62543	3.38899				
4.43944	3.7506				
5.44021	4.08122				
6.65992	4.37629				
8.16479	4.63319				
9.9929	4.97077				

Table A.5. **Experimental adsorption isotherms of CH_4 on HSZ-385HUA**

T = 303 K		T = 313 K		T = 333 K	
$\boldsymbol{P}$	$\boldsymbol{n}$	$\boldsymbol{P}$	$\boldsymbol{n}$	$\boldsymbol{P}$	$\boldsymbol{n}$
bar	$mmol \cdot g^{-1}$	bar	$mmol \cdot g^{-1}$	bar	$mmol \cdot g^{-1}$
0.00948	9.93E-04	0.00959	6.15E-04	0.00976	4.54E-04
0.01379	0.00134	0.01643	0.00103	0.01675	6.60E-04
0.02273	0.00225	0.02324	0.00154	0.02475	8.45E-04
0.0307	0.00308	0.03308	0.00242	0.03172	0.0012
0.04369	0.00456	0.04635	0.00369	0.04381	0.00182
0.06249	0.00679	0.06257	0.00522	0.06401	0.00298
0.09225	0.01119	0.09218	0.00818	0.08953	0.00462
0.13026	0.01593	0.13042	0.01208	0.13079	0.00723
0.18405	0.02265	0.18425	0.01765	0.18422	0.01078
0.26619	0.03303	0.26463	0.02591	0.26701	0.01628
0.38	0.0474	0.38031	0.03776	0.38052	0.02391
0.5469	0.06826	0.54692	0.05499	0.54773	0.03513
0.7861	0.09795	0.78666	0.07936	0.7881	0.05093
1.13158	0.1402	1.1325	0.11417	1.14037	0.07398
1.63605	0.20095	1.63943	0.16425	1.64293	0.1062
2.35515	0.28538	2.36243	0.23393	2.37219	0.15107
3.4028	0.40438	3.41575	0.33124	3.43315	0.21538
4.91665	0.56648	4.9421	0.46559	4.97962	0.30466
7.12614	0.78237	7.17875	0.64653	7.25268	0.42874
9.98645	1.03187	9.98769	0.84942	9.98916	0.55536

Table A.6. **Experimental adsorption isotherms of CO_2 on HSZ-385HUA**

T = 303 K		T = 313 K		T = 333 K	
$\boldsymbol{P}$	$\boldsymbol{n}$	$\boldsymbol{P}$	$\boldsymbol{n}$	$\boldsymbol{P}$	$\boldsymbol{n}$
bar	$mmol \cdot g^{-1}$	bar	$mmol \cdot g^{-1}$	bar	$mmol \cdot g^{-1}$
0.00623	3.50E-03	0.00643	2.57E-03	0.0096	2.55E-03
0.01483	0.00886	0.01529	0.0066	0.01918	5.30E-03
0.02397	0.01445	0.02668	0.01183	0.02689	7.43E-03
0.03138	0.01898	0.0358	0.01602	0.03612	0.01015
0.04594	0.02787	0.04518	0.02034	0.04572	0.01295
0.06415	0.03864	0.0645	0.02915	0.06248	0.01789
0.09092	0.05413	0.09001	0.04079	0.09	0.02616
0.12936	0.07579	0.1309	0.05877	0.13	0.03796
0.18524	0.10651	0.1848	0.08223	0.18522	0.05394
0.26614	0.14959	0.26582	0.11668	0.26641	0.07713
0.38167	0.20968	0.38077	0.16432	0.38084	0.10934
0.5468	0.29343	0.54724	0.23186	0.54685	0.15536
0.78585	0.41326	0.78632	0.32722	0.7851	0.21949
1.12825	0.58549	1.13046	0.46334	1.13111	0.31135
1.62458	0.84004	1.62538	0.66019	1.62378	0.44126
2.33738	1.21893	2.33556	0.94972	2.33846	0.62779
3.36624	1.77443	3.36598	1.37831	3.36352	0.89086
4.85565	2.50107	4.84614	1.97359	4.84152	1.2664
7.0002	3.25001	6.99374	2.68999	6.97454	1.7792
9.98629	3.92842	9.98668	3.42434	9.98497	2.38191

Table A.7. **Experimental adsorption isotherms of CH_4 on HSZ-390HUA**

T = 303 K		T = 313 K		T = 333 K	
$\boldsymbol{P}$	$\boldsymbol{n}$	$\boldsymbol{P}$	$\boldsymbol{n}$	$\boldsymbol{P}$	$\boldsymbol{n}$
bar	$mmol \cdot g^{-1}$	bar	$mmol \cdot g^{-1}$	bar	$mmol \cdot g^{-1}$
0.89139	0.1354	0.89297	0.11464	0.87765	0.08297
1.08585	0.1626	1.08799	0.13541	1.09211	0.09567
1.31136	0.19374	1.31537	0.1598	1.31391	0.10841
1.61445	0.23529	1.61382	0.19197	1.61965	0.12758
1.97824	0.28463	1.97971	0.23114	1.9873	0.15096
2.42549	0.34422	2.42642	0.27873	2.44189	0.17975
2.97502	0.41594	2.97656	0.33607	2.99582	0.21455
3.64648	0.50142	3.65009	0.40467	3.68171	0.25658
4.47695	0.60322	4.479	0.48664	4.52568	0.30638
5.49022	0.72228	5.49677	0.58266	5.5655	0.36561
6.74294	0.86084	6.74986	0.69563	6.85467	0.43308
8.28351	1.01896	8.29513	0.82462	8.44203	0.51312
9.99326	1.19017	9.99325	0.97237	9.9938	0.59376

Table A.8. **Experimental adsorption isotherms of CO_2 on HSZ-390HUA**

T = 303 K		T = 313 K		T = 333 K	
$\boldsymbol{P}$	$\boldsymbol{n}$	$\boldsymbol{P}$	$\boldsymbol{n}$	$\boldsymbol{P}$	$\boldsymbol{n}$
bar	$mmol \cdot g^{-1}$	bar	$mmol \cdot g^{-1}$	bar	$mmol \cdot g^{-1}$
0.89139	0.1354	0.89297	0.11464	0.87765	0.08297
1.08585	0.1626	1.08799	0.13541	1.09211	0.09567
1.31136	0.19374	1.31537	0.1598	1.31391	0.10841
1.61445	0.23529	1.61382	0.19197	1.61965	0.12758
1.97824	0.28463	1.97971	0.23114	1.9873	0.15096
2.42549	0.34422	2.42642	0.27873	2.44189	0.17975
2.97502	0.41594	2.97656	0.33607	2.99582	0.21455
3.64648	0.50142	3.65009	0.40467	3.68171	0.25658
4.47695	0.60322	4.479	0.48664	4.52568	0.30638
5.49022	0.72228	5.49677	0.58266	5.5655	0.36561
6.74294	0.86084	6.74986	0.69563	6.85467	0.43308
8.28351	1.01896	8.29513	0.82462	8.44203	0.51312
9.99326	1.19017	9.99325	0.97237	9.9938	0.59376

Table A.9. **Experimental adsorption isotherms of CH_4 on CBV-760**

T = 303 K		T = 313 K		T = 333 K	
$\boldsymbol{P}$	$\boldsymbol{n}$	$\boldsymbol{P}$	$\boldsymbol{n}$	$\boldsymbol{P}$	$\boldsymbol{n}$
bar	$mmol \cdot g^{-1}$	bar	$mmol \cdot g^{-1}$	bar	$mmol \cdot g^{-1}$
0.01217	0.00202	0.86824	0.14837	0.87477	0.1234
0.05023	0.00941	1.08303	0.18272	1.08575	0.14997
0.11534	0.02188	1.31235	0.21868	1.3169	0.17864
0.21482	0.04086	1.61376	0.2646	1.61517	0.21479
0.31939	0.06096	1.97807	0.31898	1.97866	0.25812
0.39169	0.07479	2.42292	0.38348	2.42511	0.30981
0.58655	0.11127	2.97287	0.46009	2.97523	0.37103
0.71527	0.13515	3.64405	0.55022	3.64763	0.4431
0.8801	0.1654	4.47306	0.65628	4.47929	0.52814
1.07502	0.20044	5.48425	0.7772	5.49397	0.62592
1.62892	0.29762	6.73279	0.91567	6.74686	0.73841
1.99215	0.36061	8.2697	1.07041	8.29057	0.86367
2.44478	0.43603	9.99328	1.23854	9.99326	0.99764
3.73609	0.64003				
4.53502	0.76164				
5.59011	0.91452				
6.8846	1.09251				
7.5364	1.1817				
8.32684	1.286				
9.29849	1.40486				
9.56086	1.43444				
9.98816	1.48991				

Table A.10. **Experimental adsorption isotherms of CO_2 on CBV-760**

T = 303 K		T = 313 K		T = 333 K	
$\boldsymbol{P}$	$\boldsymbol{n}$	$\boldsymbol{P}$	$\boldsymbol{n}$	$\boldsymbol{P}$	$\boldsymbol{n}$
bar	$mmol \cdot g^{-1}$	bar	$mmol \cdot g^{-1}$	bar	$mmol \cdot g^{-1}$
1.07343	0.95803	1.0831	0.76078	1.07856	0.45422
1.32195	1.14306	1.30465	0.89052	1.31451	0.53764
1.60156	1.34575	1.60243	1.05939	1.60334	0.63756
1.96919	1.60404	1.97013	1.26197	1.97186	0.76185
2.41508	1.90635	2.41231	1.49726	2.41425	0.90621
2.96041	2.2567	2.95716	1.77638	2.95767	1.07849
3.62667	2.6477	3.62699	2.10047	3.62356	1.2808
4.44515	3.06628	4.44386	2.45996	4.44283	1.51606
5.44507	3.48645	5.44473	2.84483	5.44524	1.77823
6.66959	3.88723	6.67208	3.2385	6.66978	2.0684
8.16885	4.25681	8.177	3.61174	8.18192	2.36745
9.99315	4.6908	9.99317	4.02509	9.99402	2.78121

Table A.11. **Experimental adsorption isotherms of CH_4 on CBV-780**

T = 303 K		T = 313 K		T = 333 K	
$\boldsymbol{P}$	$\boldsymbol{n}$	$\boldsymbol{P}$	$\boldsymbol{n}$	$\boldsymbol{P}$	$\boldsymbol{n}$
bar	$mmol \cdot g^{-1}$	bar	$mmol \cdot g^{-1}$	bar	$mmol \cdot g^{-1}$
0.01222	0.00209	0.01242	6.89E-04	0.01243	5.75E-04
0.04438	0.00738	0.04824	0.00585	0.04834	0.00473
0.11547	0.02055	0.1167	0.0167	0.11536	0.0127
0.2116	0.03901	0.21422	0.03215	0.21332	0.025
0.31885	0.05935	0.31934	0.04892	0.319	0.0383
0.38821	0.07242	0.38862	0.05991	0.38923	0.04731
0.58258	0.10857	0.58538	0.09031	0.58652	0.0714
0.71353	0.13256	0.71386	0.1105	0.71683	0.08744
0.87775	0.16213	0.87629	0.13528	0.87845	0.10674
1.07673	0.19742	1.07337	0.16498	1.07525	0.12965
1.31367	0.23856	1.62248	0.24355	1.62103	0.18972
1.61678	0.28983	1.98502	0.29497	1.98135	0.22968
1.98177	0.35004	2.43354	0.35513	2.43232	0.2762
2.43111	0.42195	3.70104	0.51112	3.69155	0.39348
2.97869	0.50567	4.5026	0.60578	4.49717	0.46374
3.65704	0.60515	5.53912	0.71792	5.52915	0.54984
4.48829	0.7207	6.81164	0.8465	6.7958	0.70931
5.51263	0.85364	7.50312	0.91473	7.50192	0.75185
6.77394	1.00647	8.27359	0.98813	8.27973	0.79646
8.3305	1.1736	9.23414	1.07124	9.21743	0.84612
9.9937	1.34534	9.55158	1.10455	9.54921	0.87222

Table A.12. **Experimental adsorption isotherms of CO_2 on CBV-780**

T = 303 K		T = 313 K		T = 333 K	
$\boldsymbol{P}$	$\boldsymbol{n}$	$\boldsymbol{P}$	$\boldsymbol{n}$	$\boldsymbol{P}$	$\boldsymbol{n}$
bar	$mmol \cdot g^{-1}$	bar	$mmol \cdot g^{-1}$	bar	$mmol \cdot g^{-1}$
0.01503	0.0166	0.01524	0.01145	0.01524	0.00977
0.03593	0.04006	0.03362	0.02615	0.03362	0.01957
0.0468	0.05188	0.04932	0.0391	0.04932	0.02598
0.06483	0.07143	0.06311	0.04969	0.06311	0.03495
0.07927	0.08666	0.0792	0.06204	0.0792	0.04259
0.09812	0.106	0.09653	0.07521	0.09653	0.05176
0.11381	0.12198	0.11404	0.08852	0.11404	0.06129
0.12802	0.13663	0.12955	0.10018	0.12955	0.06878
0.14479	0.15318	0.14669	0.11284	0.14669	0.07732
0.26878	0.26693	0.26913	0.19624	0.26913	0.13817
0.5339	0.48382	0.53372	0.35982	0.53372	0.25446
1.05277	0.85525	1.05354	0.64598	1.05354	0.4584
1.57481	1.19566	1.57548	0.91035	1.57548	0.64386
2.09535	1.51257	2.09524	1.15998	2.09524	0.81939
2.61759	1.81222	2.6168	1.39977	2.6168	0.98753
3.13724	2.09155	3.13706	1.6287	3.13706	1.14924
3.65726	2.34836	3.65735	1.84667	3.65735	1.3022
4.17859	2.58388	4.17797	2.05076	4.17797	1.44814
4.69704	2.7944	4.69752	2.24125	4.69752	1.59416
5.21673	2.98699	5.2186	2.42451	5.2186	1.72634
5.7373	3.15865	5.7383	2.59483	5.7383	1.85138
6.25651	3.3149	6.25843	2.74609	6.25843	1.97543
6.77669	3.45977	6.77749	2.9006	6.77749	2.09483
7.29797	3.58891	7.29915	3.04503	7.29915	2.20866
7.81653	3.71039	7.8193	3.17911	7.8193	2.31016
8.33771	3.82912	8.33937	3.30944	8.33937	2.40652
8.85884	3.93423	8.86	3.42996	8.86	2.50813
9.37788	4.03099	9.37897	3.54108	9.37897	2.59185
9.94652	4.2054	9.94544	3.73135	9.94544	2.73675

Table A.13. **Experimental adsorption isotherms of CH_4 on Sorbead® WS**

T = 303 K		T = 313 K		T = 333 K	
$\boldsymbol{P}$	$\boldsymbol{n}$	$\boldsymbol{P}$	$\boldsymbol{n}$	$\boldsymbol{P}$	$\boldsymbol{n}$
bar	$mmol \cdot g^{-1}$	bar	$mmol \cdot g^{-1}$	bar	$mmol \cdot g^{-1}$
0.00843	8.79E-04	0.00908	6.72E-04	0.00951	4.92E-04
0.01245	0.00131	0.01332	9.65E-04	0.01385	7.16E-04
0.0186	0.00197	0.02208	0.00162	0.02294	0.00121
0.02468	0.00265	0.03072	0.00227	0.03074	0.00163
0.03079	0.00333	0.04634	0.00344	0.04368	0.00233
0.04474	0.00487	0.06249	0.00466	0.0625	0.00337
0.06252	0.00681	0.09102	0.00681	0.08952	0.00485
0.08954	0.00965	0.12837	0.00963	0.12832	0.00696
0.12818	0.01371	0.18431	0.01379	0.18628	0.01012
0.18693	0.0198	0.26468	0.01971	0.26476	0.01432
0.2648	0.02778	0.38064	0.02814	0.38298	0.02059
0.38096	0.03933	0.54759	0.04006	0.5469	0.0291
0.54801	0.05522	0.79135	0.05702	0.78758	0.04131
0.78886	0.07679	1.1384	0.08031	1.13389	0.05838
1.14101	0.10648	1.64525	0.11294	1.64304	0.08265
1.64771	0.14655	2.37523	0.1575	2.37014	0.11563
2.38508	0.20073	3.44393	0.21836	3.43003	0.16121
3.45675	0.27319	4.99797	0.29976	4.97263	0.22289
5.0297	0.36959	7.29283	0.40871	7.24205	0.30696
7.35391	0.49703	9.98569	0.52564	9.98725	0.40104
9.98409	0.6281				

Table A.14. **Experimental adsorption isotherms of CO_2 on Sorbead® WS**

T = 303 K		T = 313 K		T = 333 K	
$\boldsymbol{P}$	$\boldsymbol{n}$	$\boldsymbol{P}$	$\boldsymbol{n}$	$\boldsymbol{P}$	$\boldsymbol{n}$
bar	$mmol \cdot g^{-1}$	bar	$mmol \cdot g^{-1}$	bar	$mmol \cdot g^{-1}$
0.00124	0.00418	9.72E-04	0.00438	0.00147	0.00405
0.00972	0.02083	0.01106	0.01977	0.00991	0.01219
0.0158	0.0304	0.01585	0.02548	0.01369	0.01496
0.0202	0.03684	0.02046	0.03049	0.02046	0.01936
0.03006	0.05026	0.0306	0.04085	0.03009	0.02512
0.04323	0.06673	0.04411	0.0536	0.04325	0.03243
0.06199	0.08804	0.06203	0.06905	0.06253	0.04251
0.08858	0.11585	0.08854	0.09046	0.09079	0.0562
0.12819	0.15309	0.12984	0.12065	0.12894	0.07325
0.18354	0.2	0.18346	0.15663	0.18463	0.09645
0.26435	0.26148	0.26502	0.20586	0.26502	0.12737
0.38086	0.33979	0.37892	0.26791	0.38013	0.16813
0.54448	0.43731	0.54675	0.34951	0.54677	0.22191
0.78636	0.56397	0.78602	0.45273	0.78495	0.29165
1.12954	0.72067	1.12878	0.58289	1.13146	0.38277
1.62573	0.91584	1.62501	0.74742	1.62596	0.49866
2.33705	1.15579	2.33821	0.95257	2.33946	0.6465
3.36654	1.45112	3.36772	1.20664	3.36571	0.83356
4.84883	1.80947	4.84758	1.51779	4.84836	1.06792
6.99058	2.2395	6.99029	1.89513	6.98795	1.35408
9.98496	2.74927	9.98449	2.3422	9.98513	1.69119

APPENDIX B

HIGH-PRESSURE EXPERIMENTAL DATA OF THE ADSORPTION ISOTHERMS FOR STUDIED ADSORBENTS

This appendix contains the adsorption isotherm data of seven studied zeolites in the high-pressure regime results generated from undertaking the analysis in Chapter 3.

Table B.1. Experimental absolute and excess adsorption isotherms of CH_4 on HSZ-320HOA

T = 304 K			T = 313 K			T = 334 K		
P	n_{abs}	n_{exc}	P	n_{abs}	n_{exc}	P	n_{abs}	n_{exc}
bar	$mmol \cdot g^{-1}$	$mmol \cdot g^{-1}$	bar	$mmol \cdot g^{-1}$	$mmol \cdot g^{-1}$	bar	$mmol \cdot g^{-1}$	$mmol \cdot g^{-1}$
0.5	0.1021	0.1020	0.5	0.0589	0.0589	0.5	0.0513	0.0512
1.0	0.2132	0.2128	1.0	0.1489	0.1485	1.0	0.1244	0.1243
2.0	0.4261	0.4247	2.0	0.3349	0.3335	2.0	0.2594	0.2587
5.0	0.9819	0.9737	5.0	0.8161	0.8086	5.0	0.6062	0.6019
10.0	1.6596	1.6314	10.0	1.4357	1.4100	10.0	1.0922	1.0760
15.0	2.1192	2.0645	15.0	1.8745	1.8244	15.0	1.4657	1.4325
20.0	2.4346	2.3499	20.0	2.1903	2.1122	20.0	1.7560	1.7021
25.0	2.6697	2.5524	25.0	2.4253	2.3169	25.0	1.9847	1.9078
30.0	2.8433	2.6920	30.0	2.6048	2.4643	30.0	2.1671	2.0655
35.0	2.9740	2.7877	35.0	2.7447	2.5710	35.0	2.3135	2.1859
40.2	3.0815	2.8588	40.2	2.8588	2.6506	40.2	2.4328	2.2786
45.3	3.1600	2.9008	45.3	2.9436	2.7009	45.3	2.5291	2.3473
50.2	3.2278	2.9318	50.2	3.0164	2.7387	50.2	2.6110	2.4019
60.1	3.3171	2.9467	60.1	3.1172	2.7692	60.1	2.7329	2.4677
70.1	3.3698	2.9236	70.1	3.1873	2.7663	70.2	2.8141	2.4918
80.1	3.3941	2.8736	80.1	3.2149	2.7241	80.1	2.8657	2.4878
90.1	3.3951	2.8023	90.1	3.2364	2.6745	90.0	2.8956	2.4627
100.2	3.3966	2.7122	100.2	3.2374	2.6012	100.2	2.9121	2.4240

Table B.2. **Experimental absolute and excess adsorption isotherms of CO_2 on HSZ-320HOA**

T = 304 K			T = 313 K			T = 333 K		
P bar	n_{abs} $mmol \cdot g^{-1}$	n_{exc} $mmol \cdot g^{-1}$	P bar	n_{abs} $mmol \cdot g^{-1}$	n_{exc} $mmol \cdot g^{-1}$	P bar	n_{abs} $mmol \cdot g^{-1}$	n_{exc} $mmol \cdot g^{-1}$
1.0	2.6348	2.6291	1.1	2.3194	2.3139	1.0	1.5171	1.5143
2.0	3.5597	3.5444	2.4	3.3998	3.3820	2.0	2.2615	2.2526
5.0	4.7723	4.7169	5.0	4.3907	4.3413	5.0	3.5090	3.4725
10.8	5.4816	5.3383	10.0	5.1175	4.9988	10.0	4.3868	4.2933
14.9	5.7421	5.5295	15.0	5.4793	5.2827	15.0	4.8233	4.6655
19.8	5.9638	5.6620	20.0	5.7217	5.4401	19.9	5.1016	4.8766
24.9	6.1485	5.7447	24.8	5.9026	5.5321	24.9	5.3117	5.0118
29.9	6.3068	5.7902	30.0	6.0649	5.5903	30.1	5.4865	5.1036
34.8	6.4542	5.8151	35.1	6.2099	5.6218	34.9	5.6232	5.1565
39.5	6.5894	5.8180	39.7	6.3313	5.6307	39.8	5.7508	5.1944
44.5	6.7420	5.8060	44.5	6.4559	5.6245	44.5	5.8565	5.2074
49.7	6.9146	5.7764	50.0	6.5978	5.5982	49.6	5.9765	5.2165

Table B.3. Experimental absolute and excess adsorption isotherms of CH_4 on HSZ-350HUA

T = 303 K			T = 313 K			T = 333 K		
P	n_{abs}	n_{exc}	P	n_{abs}	n_{exc}	P	n_{abs}	n_{exc}
bar	$mmol \cdot g^{-1}$	$mmol \cdot g^{-1}$	bar	$mmol \cdot g^{-1}$	$mmol \cdot g^{-1}$	bar	$mmol \cdot g^{-1}$	$mmol \cdot g^{-1}$
0.5	0.1127	0.1125	0.5	0.0680	0.0678	0.5	0.0634	0.0632
1.0	0.2158	0.2153	1.0	0.1608	0.1603	1.0	0.1277	0.1272
2.0	0.4178	0.4160	2.0	0.3285	0.3272	2.0	0.2555	0.2541
5.0	0.9652	0.9558	5.0	0.7902	0.7830	5.0	0.6000	0.5937
10.0	1.6824	1.6509	10.0	1.4300	1.4048	10.0	1.1058	1.0851
15.0	2.2096	2.1478	15.0	1.9130	1.8626	15.0	1.5091	1.4682
20.0	2.5995	2.5024	20.0	2.2846	2.2041	20.0	1.8464	1.7806
25.0	2.8899	2.7545	25.0	2.5759	2.4620	25.0	2.1164	2.0227
30.0	3.1210	2.9445	30.0	2.8065	2.6567	30.0	2.3376	2.2137
35.0	3.3035	3.0839	35.0	2.9977	2.8098	35.0	2.5273	2.3709
40.4	3.4556	3.1901	40.5	3.1517	2.9228	40.3	2.6909	2.5000
45.4	3.5712	3.2602	45.5	3.2831	3.0132	45.3	2.8170	2.5916
50.3	3.6799	3.3220	50.4	3.3922	3.0812	50.2	2.9371	2.6759
60.2	3.8313	3.3787	60.3	3.5535	3.1586	60.1	3.1042	2.7714
70.3	3.9462	3.3937	70.4	3.6746	3.1919	70.2	3.2596	2.8486
80.3	4.0358	3.3816	80.3	3.7662	3.1948	80.2	3.3626	2.8751
90.2	4.0913	3.3361	90.3	3.8354	3.1741	90.1	3.4395	2.8749
100.4	4.1383	3.2770	100.4	3.8801	3.1281	100.3	3.5096	2.8646

Table B.4. Experimental absolute and excess adsorption isotherms of CO_2 on HSZ-350HUA

T = 303 K			T = 313 K			T = 333 K		
P	n_{abs}	n_{exc}	P	n_{abs}	n_{exc}	P	n_{abs}	n_{exc}
bar	$mmol \cdot g^{-1}$	$mmol \cdot g^{-1}$	bar	$mmol \cdot g^{-1}$	$mmol \cdot g^{-1}$	bar	$mmol \cdot g^{-1}$	$mmol \cdot g^{-1}$
2.2	2.3846	2.3730	2.1	1.7923	1.7844	1.9	1.0946	1.0905
5.1	4.1358	4.0878	5.1	3.5110	3.4712	5.3	2.5064	2.4792
9.9	5.2654	5.1421	10.1	4.7623	4.6532	10.3	3.7852	3.7026
15.1	5.8309	5.6157	15.1	5.3602	5.1714	15.3	4.4718	4.3237
20.2	6.1805	5.8675	19.9	5.7600	5.4853	19.9	4.8989	4.6838
24.7	6.4351	6.0231	24.8	6.0415	5.6718	25.0	5.3177	5.0169
30.0	6.6836	6.1426	29.5	6.2597	5.7912	29.6	5.5583	5.1786
35.0	6.8976	6.2188	35.1	6.4832	5.8836	34.9	5.7795	5.3011
40.1	7.1037	6.2640	39.8	6.6547	5.9335	39.7	5.9541	5.3787
45.7	7.3247	6.2820	44.9	6.8289	5.9606	45.4	6.1213	5.4254
49.6	7.5008	6.2850	49.5	6.9798	5.9625	49.9	6.2619	5.4589

Table B.5. Experimental absolute and excess adsorption isotherms of CH_4 on HSZ-385HUA

T = 305 K			T = 313 K			T = 333 K		
P	n_{abs}	n_{exc}	P	n_{abs}	n_{exc}	P	n_{abs}	n_{exc}
bar	$mmol \cdot g^{-1}$	$mmol \cdot g^{-1}$	bar	$mmol \cdot g^{-1}$	$mmol \cdot g^{-1}$	bar	$mmol \cdot g^{-1}$	$mmol \cdot g^{-1}$
0.5	0.0739	0.0737	0.5	0.0595	0.0594	0.5	0.0547	0.0547
1.0	0.1431	0.1428	1.0	0.1165	0.1163	1.0	0.1051	0.1050
2.0	0.2915	0.2905	2.0	0.2501	0.2494	2.0	0.2029	0.2024
5.0	0.7227	0.7166	5.0	0.6235	0.6186	5.0	0.4819	0.4783
10.0	1.3282	1.3053	10.0	1.1573	1.1385	10.0	0.9010	0.8873
15.0	1.8138	1.7665	15.0	1.6018	1.5622	15.0	1.2679	1.2384
20.0	2.1949	2.1178	20.0	1.9621	1.8966	20.0	1.5765	1.5271
25.0	2.4956	2.3851	25.0	2.2546	2.1595	25.0	1.8407	1.7679
30.0	2.7412	2.5942	30.0	2.5020	2.3740	30.0	2.0645	1.9657
35.0	2.9488	2.7626	35.0	2.7086	2.5455	35.0	2.2554	2.1286
40.2	3.1232	2.8963	40.2	2.8928	2.6925	40.2	2.4338	2.2766
45.2	3.2700	3.0001	45.2	3.0348	2.7962	45.2	2.5814	2.3925
50.1	3.3990	3.0854	50.1	3.1668	2.8886	50.1	2.7060	2.4851
60.0	3.6127	3.2067	60.0	3.3889	3.0268	60.0	2.9273	2.6376
70.1	3.7882	3.2831	70.1	3.5603	3.1098	70.1	3.1070	2.7441
80.0	3.9227	3.3168	80.0	3.7046	3.1623	80.1	3.2604	2.8214
90.0	4.0484	3.3356	90.0	3.8301	3.1921	90.0	3.3914	2.8735
100.1	4.1539	3.3294	100.1	3.9254	3.1898	100.2	3.4946	2.8961

Table B.6. Experimental absolute and excess adsorption isotherms of CO_2 on HSZ-385HUA

T = 305 K			T = 313 K			T = 333 K		
P	n_{abs}	n_{exc}	P	n_{abs}	n_{exc}	P	n_{abs}	n_{exc}
bar	$mmol \cdot g^{-1}$	$mmol \cdot g^{-1}$	bar	$mmol \cdot g^{-1}$	$mmol \cdot g^{-1}$	bar	$mmol \cdot g^{-1}$	$mmol \cdot g^{-1}$
1.1	0.6108	0.6091	0.8	0.3160	0.3152	1.0	0.2734	0.2727
2.6	1.4783	1.4694	2.1	0.9348	0.9301	2.9	0.8602	0.8548
5.1	2.8981	2.8635	5.6	2.5239	2.4914	5.1	1.5091	1.4926
10.1	4.3115	4.2070	10.1	3.7729	3.6837	10.0	2.6960	2.6378
15.0	4.9416	4.7585	14.8	4.4223	4.2661	15.1	3.4864	3.3708
20.0	5.3378	5.0658	20.1	4.8756	4.6363	20.0	3.9630	3.7857
25.6	5.6653	5.2816	25.1	5.1709	4.8446	24.9	4.3063	4.0605
29.8	5.8659	5.3897	29.9	5.4034	4.9854	30.0	4.5598	4.2401
35.0	6.0830	5.4787	34.7	5.5844	5.0658	34.8	4.7604	4.3637
39.9	6.2706	5.5306	39.8	5.7625	5.1276	40.0	4.9287	4.4442
44.8	6.4574	5.5574	44.8	5.9073	5.1469	45.0	5.0593	4.4863
49.5	6.6543	5.5727	49.6	6.0599	5.1589	49.7	5.1864	4.5202

Table B.7. Experimental absolute and excess adsorption isotherms of CH_4 on HSZ-390HUA

T = 305 K			T = 313 K			T = 333 K		
P	n_{abs}	n_{exc}	P	n_{abs}	n_{exc}	P	n_{abs}	n_{exc}
bar	$mmol \cdot g^{-1}$	$mmol \cdot g^{-1}$	bar	$mmol \cdot g^{-1}$	$mmol \cdot g^{-1}$	bar	$mmol \cdot g^{-1}$	$mmol \cdot g^{-1}$
0.5	0.0751	0.0750	0.5	0.0372	0.0371	0.5	0.0218	0.0218
2.0	0.3080	0.3073	2.0	0.1711	0.1706	2.0	0.1245	0.1241
5.0	0.7326	0.7275	5.0	0.5391	0.5348	5.0	0.3998	0.3970
10.0	1.3298	1.3093	10.0	1.0705	1.0528	10.0	0.8111	0.7992
15.0	1.7984	1.7552	15.0	1.5007	1.4631	15.0	1.1553	1.1292
20.0	2.1637	2.0928	20.0	1.8445	1.7823	20.0	1.4539	1.4094
25.0	2.4547	2.3525	25.0	2.1250	2.0347	25.0	1.6936	1.6281
30.0	2.6699	2.5348	30.0	2.3394	2.2192	30.0	1.9130	1.8234
35.0	2.8596	2.6888	35.0	2.5258	2.3732	35.0	2.0995	1.9836
40.2	2.9938	2.7875	40.2	2.6827	2.4964	40.2	2.2306	2.0892
45.2	3.1154	2.8711	45.2	2.7983	2.5779	45.2	2.3557	2.1864
50.1	3.2217	2.9389	50.1	2.9102	2.6542	50.1	2.4546	2.2578
60.0	3.3660	3.0058	60.0	3.0628	2.7356	60.0	2.6299	2.3742
70.1	3.4764	3.0347	70.1	3.1742	2.7728	70.1	2.7550	2.4388
80.1	3.5360	3.0153	80.1	3.2536	2.7780	80.0	2.8531	2.4755
90.0	3.5765	2.9762	90.0	3.3086	2.7586	90.0	2.9132	2.4761
100.1	3.5911	2.9122	100.1	3.3275	2.7056	100.1	2.9549	2.4578

Table B.8. Experimental absolute and excess adsorption isotherms of CO_2 on HSZ-390HUA

T = 305 K			T = 313 K			T = 333 K		
P	n_{abs}	n_{exc}	P	n_{abs}	n_{exc}	P	n_{abs}	n_{exc}
bar	$mmol \cdot g^{-1}$	$mmol \cdot g^{-1}$	bar	$mmol \cdot g^{-1}$	$mmol \cdot g^{-1}$	bar	$mmol \cdot g^{-1}$	$mmol \cdot g^{-1}$
1.0	0.5603	0.5106	2.0	0.8737	0.7973	3.0	0.8745	0.7949
2.2	1.2385	1.1841	5.1	2.3362	2.2376	5.5	1.6016	1.5094
5.1	2.9401	2.8574	10.2	3.8676	3.7051	10.2	2.8023	2.6679
10.2	4.3756	4.2215	15.0	4.5208	4.2902	15.1	3.5703	3.3797
14.9	4.9618	4.7338	20.2	4.9525	4.6406	20.0	4.0598	3.8063
19.9	5.3506	5.0347	25.1	5.2327	4.8365	25.0	4.3754	4.0546
25.0	5.6207	5.2083	29.7	5.4346	4.9527	29.7	4.6139	4.2233
29.6	5.8169	5.3083	34.7	5.6102	5.0262	35.1	4.8137	4.3397
35.1	6.0173	5.3777	40.9	5.7839	5.0617	40.1	4.9674	4.4088
39.4	6.1477	5.3973	47.3	5.9404	5.0562	44.9	5.0753	4.4335
44.3	6.2620	5.3705	49.6	5.9881	5.0392	49.8	5.1853	4.4502
49.5	6.4364	5.3607	--	--	--	--	--	--

Table B.9. Experimental absolute and excess adsorption isotherms of CH_4 on CBV-760

T = 304 K			T = 313 K			T = 333 K		
P	n_{abs}	n_{exc}	P	n_{abs}	n_{exc}	P	n_{abs}	n_{exc}
bar	$mmol \cdot g^{-1}$	$mmol \cdot g^{-1}$	bar	$mmol \cdot g^{-1}$	$mmol \cdot g^{-1}$	bar	$mmol \cdot g^{-1}$	$mmol \cdot g^{-1}$
0.5	0.1035	0.1034	0.5	0.0477	0.0477	0.5	0.0121	0.0120
1.0	0.1827	0.1825	1.0	0.1117	0.1116	1.0	0.0855	0.0851
2.0	0.3538	0.3531	2.0	0.2199	0.2189	2.0	0.2151	0.2147
5.0	0.8144	0.8087	5.0	0.6157	0.6099	5.0	0.5135	0.5104
10.0	1.4322	1.4101	10.0	1.1779	1.1567	10.0	0.9423	0.9294
15.0	1.9140	1.8678	15.0	1.6119	1.5689	15.0	1.3090	1.2807
20.0	2.2837	2.2085	20.0	1.9655	1.8956	20.0	1.6066	1.5591
25.0	2.5795	2.4716	25.0	2.2482	2.1479	25.0	1.8636	1.7935
30.0	2.8054	2.6625	30.0	2.4671	2.3345	30.0	2.0849	1.9896
35.0	2.9992	2.8187	35.0	2.6750	2.5062	35.0	2.2610	2.1391
40.2	3.1777	2.9564	40.3	2.8429	2.6363	40.3	2.4220	2.2712
45.3	3.3003	3.0390	45.3	2.9757	2.7311	45.3	2.5685	2.3870
50.2	3.4263	3.1223	50.2	3.0965	2.8124	50.2	2.6806	2.4690
60.1	3.6098	3.2190	60.1	3.3000	2.9328	60.1	2.8761	2.6003
70.2	3.7638	3.2795	70.2	3.4600	3.0047	70.2	3.0360	2.6918
80.1	3.8845	3.3045	80.2	3.5746	3.0314	80.1	3.1519	2.7396
90.1	3.9634	3.2884	90.1	3.6708	3.0365	90.1	3.2614	2.7771
100.2	4.0311	3.2572	100.3	3.7354	3.0104	100.2	3.3480	2.7902

Table B.10. Experimental absolute and excess adsorption isotherms of CO_2 on CBV-760

T = 304 K			T = 313 K			T = 334 K		
P	n_{abs}	n_{exc}	P	n_{abs}	n_{exc}	P	n_{abs}	n_{exc}
bar	$mmol \cdot g^{-1}$	$mmol \cdot g^{-1}$	bar	$mmol \cdot g^{-1}$	$mmol \cdot g^{-1}$	bar	$mmol \cdot g^{-1}$	$mmol \cdot g^{-1}$
1.0	0.7605	0.7413	1.4	0.9108	0.8528	1.2	0.4914	0.4406
2.1	1.5447	1.5200	4.1	2.3523	2.2754	5.0	1.7899	1.7217
5.0	3.2573	3.2022	10.3	4.1731	4.0191	10.4	3.1109	2.9925
9.8	4.6009	4.4753	15.0	4.8362	4.6097	15.0	3.8036	3.6295
15.0	5.3068	5.0934	20.0	5.2866	4.9759	20.0	4.3018	4.0612
19.8	5.7388	5.4340	24.9	5.6365	5.2324	25.0	4.6629	4.3481
24.9	6.1017	5.6862	29.9	5.9294	5.4192	29.9	4.9498	4.5562
29.8	6.4005	5.8662	35.0	6.1766	5.5469	34.9	5.1753	4.6948
34.8	6.6723	5.9980	39.6	6.3832	5.6335	39.8	5.3849	4.8114
39.7	6.9099	6.0847	44.7	6.5790	5.6829	44.8	5.5441	4.8723
44.4	7.1242	6.1306	49.6	6.7700	5.7129	49.6	5.7076	4.9283

Table B.11. Experimental absolute and excess adsorption isotherms of CH_4 on CBV-780

T = 305 K			T = 314 K			T = 334 K		
P	n_{abs}	n_{exc}	P	n_{abs}	n_{exc}	P	n_{abs}	n_{exc}
bar	$mmol \cdot g^{-1}$	$mmol \cdot g^{-1}$	bar	$mmol \cdot g^{-1}$	$mmol \cdot g^{-1}$	bar	$mmol \cdot g^{-1}$	$mmol \cdot g^{-1}$
0.5	0.0394	0.0394	0.5	0.0318	0.0318	1.0	0.0568	0.0568
2.0	0.2913	0.2908	2.0	0.1659	0.1654	2.0	0.1566	0.1566
5.0	0.7173	0.7127	5.0	0.5494	0.5451	5.0	0.4536	0.4513
10.0	1.2976	1.2784	10.0	1.0645	1.0471	10.0	0.8674	0.8566
15.0	1.7385	1.6980	15.0	1.4733	1.4367	15.0	1.1970	1.1728
20.0	2.0778	2.0113	20.0	1.8038	1.7432	20.0	1.4924	1.4505
25.0	2.3593	2.2628	25.0	2.0745	1.9865	25.0	1.7323	1.6700
30.0	2.5886	2.4594	30.0	2.2873	2.1699	30.0	1.9421	1.8565
35.0	2.7845	2.6199	35.0	2.4874	2.3370	35.0	2.1161	2.0059
40.2	2.9503	2.7482	40.3	2.6462	2.4616	40.2	2.2757	2.1384
45.3	3.0913	2.8502	45.3	2.7894	2.5685	45.3	2.4209	2.2546
50.2	3.2122	2.9315	50.2	2.9128	2.6551	50.2	2.5455	2.3499
60.1	3.4175	3.0525	60.1	3.1265	2.7901	60.1	2.7500	2.4926
70.2	3.5856	3.1303	70.2	3.3011	2.8806	70.2	2.9235	2.5992
80.1	3.7445	3.1922	80.1	3.4442	2.9370	80.1	3.0756	2.6815
90.1	3.8704	3.2185	90.1	3.5789	2.9790	90.1	3.1986	2.7327
100.2	3.9747	3.2199	100.2	3.6917	2.9956	100.2	3.3155	2.7726

Table B.12. Experimental absolute and excess adsorption isotherms of CO_2 on CBV-780

T = 305 K			T = 314 K			T = 334 K		
P	n_{abs}	n_{exc}	P	n_{abs}	n_{exc}	P	n_{abs}	n_{exc}
bar	$mmol \cdot g^{-1}$	$mmol \cdot g^{-1}$	bar	$mmol \cdot g^{-1}$	$mmol \cdot g^{-1}$	bar	$mmol \cdot g^{-1}$	$mmol \cdot g^{-1}$
2.7	1.8649	1.7644	1.5	0.8969	0.8130	1.5	0.5646	0.4741
5.2	3.1180	2.9917	5.1	2.5381	2.4289	5.7	1.8740	1.7638
10.1	4.3054	4.1139	9.8	3.7696	3.6051	10.1	2.8636	2.7146
15.0	4.9375	4.6686	15.0	4.4836	4.2460	15.0	3.5816	3.3777
19.9	5.3673	5.0122	20.1	4.9356	4.6182	20.2	4.0735	3.8047
24.8	5.7252	5.2707	24.9	5.2856	4.8809	25.1	4.4310	4.0925
30.3	6.0608	5.4809	29.9	5.5444	5.0443	30.2	4.7203	4.3041
34.6	6.3795	5.6781	34.9	5.8473	5.2317	34.9	4.9652	4.4682
40.9	6.6663	5.7792	40.4	6.1152	5.3607	40.5	5.1967	4.5972
44.7	6.8789	5.8570	44.5	6.3150	5.4431	45.1	5.3945	4.7005
49.3	7.1450	5.9292	49.4	6.5346	5.5058	49.4	5.5547	4.7651

Table B.13. Experimental absolute and excess adsorption isotherms of CH_4 on Sorbead® WS

T = 303 K			T = 313 K			T = 334 K		
P	n_{abs}	n_{exc}	P	n_{abs}	n_{exc}	P	n_{abs}	n_{exc}
bar	$mmol \cdot g^{-1}$	$mmol \cdot g^{-1}$	bar	$mmol \cdot g^{-1}$	$mmol \cdot g^{-1}$	bar	$mmol \cdot g^{-1}$	$mmol \cdot g^{-1}$
0.49	0.0187	0.0186	0.49	0.0169	0.0169	0.28	0.0143	0.0142
0.98	0.0642	0.0639	0.97	0.0547	0.0545	0.49	0.0272	0.0271
1.98	0.1454	0.1445	1.98	0.1244	0.1237	0.98	0.0532	0.0530
4.98	0.3529	0.3481	4.98	0.3053	0.3015	1.98	0.1046	0.1040
9.98	0.6319	0.6159	9.98	0.5538	0.5405	4.98	0.2447	0.2416
14.97	0.8654	0.8331	14.97	0.7626	0.7357	9.98	0.4129	0.4041
19.97	1.0894	1.0353	19.97	0.9464	0.9021	14.97	0.6317	0.6096
24.97	1.2488	1.1718	24.98	1.1120	1.0469	19.97	0.7823	0.7465
29.97	1.4126	1.3079	30	1.2639	1.1749	24.97	0.9153	0.8641
34.97	1.5644	1.4293	35	1.4034	1.2876	29.97	1.0172	0.9504
40.2	1.7120	1.5410	40.2	1.5318	1.3867	34.97	1.1329	1.0454
45.2	1.8270	1.6211	45.3	1.6508	1.4739	40.2	1.2404	1.1309
50.1	1.9448	1.7003	50.2	1.7595	1.5493	45.2	1.3423	1.2086
60	2.1470	1.8210	60.1	1.9561	1.6732	50.1	1.4350	1.2761
70.1	2.3469	1.9237	70.1	2.1334	1.7690	60	1.6048	1.3905
80.1	2.5279	2.0003	80.1	2.2890	1.8377	70.1	1.7577	1.4818
--	--	--	--	--	--	80.1	1.8939	1.5523

Table B.14. Experimental absolute and excess adsorption isotherms of CO_2 on Sorbead® WS

T = 303 K			T = 313 K			T = 334 K		
$\boldsymbol{P}$	$\boldsymbol{n_{abs}}$	$\boldsymbol{n_{exc}}$	$\boldsymbol{P}$	$\boldsymbol{n_{abs}}$	$\boldsymbol{n_{exc}}$	$\boldsymbol{P}$	$\boldsymbol{n_{abs}}$	$\boldsymbol{n_{exc}}$
bar	$mmol \cdot g^{-1}$	$mmol \cdot g^{-1}$	bar	$mmol \cdot g^{-1}$	$mmol \cdot g^{-1}$	bar	$mmol \cdot g^{-1}$	$mmol \cdot g^{-1}$
1	0.6604	0.6588	1.2	0.6307	0.6288	1.2	0.3982	0.3972
2.1	1.0859	1.0806	5	1.5975	1.5791	5	1.1215	1.1096
5	1.8870	1.8647	9.9	2.4316	2.3754	9.9	1.7762	1.7379
9.8	2.8328	2.7658	15	3.1060	2.9949	14.9	2.2897	2.2148
14.9	3.5858	3.4535	19.8	3.6455	3.4692	20	2.7402	2.6178
20.3	4.2649	4.0443	25.5	4.2165	3.9462	24.9	3.1246	2.9473
24.8	4.7843	4.4736	29.9	4.6001	4.2461	30.1	3.4998	3.2541
29.7	5.3213	4.8933	34.6	5.0234	4.5618	35.1	3.8307	3.5101
34.4	5.8210	5.2585	39.7	5.4652	4.8689	43.3	4.3339	3.8688
41.2	6.5208	5.7211	45.4	5.9416	5.1675	--	--	--